The Pennsylvania State University

The Graduate School

MULTISCALE MODELING OF LITHIUM METAL ANODE FOR NEXT-GENERATION BATTERY DESIGN

A Dissertation in

Materials Science and Engineering

by

Zhe Liu

Submitted in Partial Fulfillment
of the Requirements
for the Degree of

Doctor of Philosophy

December 2019

The dissertation of Zhe Liu was reviewed and approved* by the following:

Long-Qing Chen
Donald W. Hamer Professor of Materials Science and Engineering
Professor of Engineering Science and Mechanics, and Mathematics
Dissertation Advisor
Chair of Committee

Chao-Yang Wang
Diefenderfer Chaired Professor of Mechanical and Nuclear Engineering
Professor of Chemical Engineering

Ismaila Dabo
Associate Professor of Materials Science and Engineering

Adri van Duin
Professor of Mechanical Engineering, Chemical Engineering, Engineering Science and Mechanics, Engineering Science and Mechanics, Chemistry, Materials Science and Engineering

John Mauro
Professor of Materials Science and Engineering
Chair, Intercollege Graduate Degree Program in Materials Science and Engineering

*Signatures are on file in the Graduate School

ABSTRACT

Achieving smooth Li-plating without dendrite growth remains to be a grand challenge for developing the next-generation batteries based on Li metal anode. One of the main reasons is our inability to directly model and predict the atomistic and mesoscale mechanisms underlying the complex electroplating process involving concurrent ionic transport, redox reaction, and development of morphological instability. This dissertation presents a phase-field-based multiscale modeling framework to fundamentally understand the dendrite growth mechanism, theoretically interpret the experimental phenomena, and guide the Li metal battery design.

The stability and functionality of the solid electrolyte interphase (SEI), i.e. the passivation layer between anode and electrolyte, play critical roles in maintaining a decent battery cycle life as well as calendar life. This becomes even more critical for Li metal anode, which is subjected to large volumetric and interfacial variations during Li plating and stripping. However, there is currently a lack of comprehensive understanding of Li metal/SEI interfaces and their electrochemical and mechanical properties, as well as the SEI growth mechanism at Li metal anode. In this thesis, we employed combined atomistic calculations and experimental techniques to study SEI. Using density function theory (DFT) calculations, we evaluated the interfacial energetics, density of states (DOS), and electrostatic potential profiles of two interfaces, LiF/Li and Li_2CO_3/Li, at Li metal anode. The calculation results suggest higher interface mechanical stability at the Li_2CO_3/Li interface but better electron tunneling leakage resistance at the LiF/Li interface. Experimentally, we employed an isotope-assisted time-of-flight secondary ion mass spectrometry (TOF SIMS) method to reveal a “bottom-up” formation mechanism of SEI growth. It is found that the topmost SEI near the electrolyte formed first and the SEI near the electrode formed later during the initial formation cycle. This growth mechanism was then correlated to the

electrolyte one-electron and two-electron reduction reaction dynamics, which in turn explains the formation of two-layered organic-inorganic SEI composite structure. These results provide physical interpretation for the mesoscale phenomena and thus valuable insights for advanced electrode protective coating design.

Continuum models have been widely used in attempts to understand and solve the Li dendrite growth problem at mesoscale. However, the limited availability and the accuracy of input physical parameters often limit the predictive power of existing continuum simulations. We hereby developed a multiscale model for a metal electrodeposition process based on the phase-field method and transition state theory by connecting the atomic level charge-transfer physics to the mesoscale morphological evolution. With this model, we discovered that the difference in cation de-solvation-induced exchange current is mainly responsible for the dramatic difference in dendritic Li-plating and smooth Mg-plating. This study not only reveals the physical origin of Li dendrite growth, but also provides a strategy to design dendrite-free Li-ion battery anodes guided by this multiscale model integrating the phase-field method and atomistic calculations.

All-solid-state battery is a promising solution to suppress Li dendrite growth. However, recent experimental observation of mechanically-hard ceramic solid electrolytes such as LLZO indicates intergranular dendrite penetration. To understand the Li plating behavior in solid electrolytes, we further extended the multiscale phase-field model of Li dendrite growth by incorporating multiphase solid mechanics and explicit dendrite nucleation. This model helps elucidate the mechanism of major failure modes in a wide range of existing solid electrolyte systems, such as dendrite penetration, intergranular growth and isolated nucleation.

TABLE OF CONTENTS

LIST OF FIGURES

LIST OF TABLES

LIST OF SYMBOLS

Symbols	Physical Quantities
A	Dimensionless area/number of reaction sites
a	Activity
B_0	Exchange current pre-factor
b_1, b_2, b_3, b_4	Phenomenological parameters
$\tilde{c}$	Dimensionless concentration
c	Concentration
C_{ijkl}	Elastic stiffness tensors
D	Diffusion coefficient
D_{DOS}	Density of states
E	Energy
F	Faraday Constant
f	Free energy density
F_{Fermi}	Fermi function
G	Free energy
I	Current
i	Current density
i_0	Exchange current density
J^*	Nucleation rate
k_0	Reaction rate constant
k_b	Boltzmann constant
l	System size
L_η	Electrochemical pre-factor
L_σ	Interface mobility
n	Valence
$\bar{n}$	Number of electrons per volume
N_A	Avogadro's Constant
N_{sol}	Solvation shell size parameter

P_N	Nucleation probability
R	Gas constant
r	Radius
$\bar{R}$	Reaction rate
S	Surface area
T	Temperature
t	Time
u	Short-range interaction coefficient
V	Volume
W	Energy barrier
$W_{Adhesion}$	Work of adhesion
Y	Young's modulus
α	symmetric factor
γ	Surface energy
γ_{TS}	activity coefficient at transition state
δ	Anisotropy strength
δ_N	Dirac delta function of nucleation
$\bar{\varepsilon}$	Energy of states
ε_{ij}	Strain
ε_{ij}^0	Eigen strain
ζ	Correction factor for inhomogeneous nucleation
η	Overpotential
Θ	Standard State
θ	Mean coverage fraction
κ	Gradient coefficient
λ_T	Temperature correction factor
μ	Chemical potential
$\bar{\mu}$	Electrochemical potential
ν	Poisson ratio
ξ	Phase fraction of Li metal

ρ	Thickness parameter for surface DOS
σ	Conductivity
τ	Interfacial energy
φ	Phase fraction of solid electrolyte grain i
ϕ	Electrostatic potential
χ	Step function for surface DOS
ψ	Angle between surface normal and reference
ω	Crystallographic symmetry mode
Ω	SEI effective coefficient

In the table above, subscripts i,j,k,l = 1,2,3,4 are indices for tensors.

ACKNOWLEDGEMENTS

I would like to thank my advisor, Prof. Long-Qing Chen, for continuously mentoring and encouraging me in my research and life at Penn State during the last six years. He is not only a knowledgeable educator, an excellent researcher, but also an enthusiastic leader, who has inspired me with his enlightening in teaching, his diligence in science, and his vitality in management. As a top scientist in computational modeling and materials science, he provided us with a vast platform to communicate and collaborate with world's leading groups and researchers. Without his help, none of my achievements would have been possible.

I would like to thank Prof. Chao-Yang Wang, Prof. Dabo Ismaila, and Prof. Adri van Duin, for serving on my Ph.D. committees and providing in-depth discussions and insightful suggestions on my research and career. I would like to thank Dr. Peng Lu (now at Apple Inc.), Dr. Xingcheng Xiao, Dr. Qinglin Zhang, Dr. Ingrid Rousseau and all the colleagues at General Motors for the great memory of my summer intern at Warren Tech Center in 2015 and 2016. I would like to thank Prof. Yue Qi at Michigan State University for co-advising me and leading the collaboration projects. I am also grateful to my collaborators, Prof. Yuan Yang at Colombia University, Prof. Donghai Wang at Penn State University, Prof. Yi Cui at Stanford University, Prof. Ce-Wen Nan and Prof. Yuan-Hua Lin at Tsinghua University, that provided great opportunities for me to apply my computation models to their latest cutting-edge experimental findings.

I would like to thank all my labmates and friends at Penn State for their kind help and encouragement. Particularly, I would like to thank Dr. Bi-Cheng Zhou (now professor at University of Virginia) for the patient teaching that opened the door for me to density functional theory, and Dr. Chao Yang (now in Beijing) for in-depth discussions that introduced to me the phase-field model and advanced electrochemistry. I would like to thank Dr. Yanzhou Ji and Dr.

Guoxing Li for insightful ideas, detailed suggestions and close help in my research; I would like to thank Dr. Lei Chen (now a professor at Mississippi State University) for the modeling framework left for me to take over; I would also like to thank Mr. Bo Wang, Mr. Xiaoxing Cheng, Mr. Yin Shi, Dr. Tiannan Yang, Dr. Yakun Yuan (now at University of California at Los Angeles) for experiencing together the ups and downs in the seemingly-endless Ph.D. life.

Last and importantly, I would like to thank my beloved parents, who have been so supportive and considerate in everything.

Financial support for this research was through National Science Foundation under contract CMMI-1235092 and Department of Energy under contract DE-EE0007803. Computational support was through the Penn State Institute for CyberScience and calculations were performed on the Lion-X, Cyberstar, and ACI servers. The findings and conclusions do not necessarily reflect the view of the funding agency.

Chapter 1

Introduction

1.1 Lithium metal batteries and dendrite suppression

1.1.1 Challenges in lithium ion batteries

Rechargeable or secondary Lithium ion batteries (LIBs) have been the most effective energy-storage solution for a wide range of applications [1-8], and regarded as one of the most promising power strategies for the on-going revolution in vehicle electrification [9-16]. The ever-growing demands in global energy market promoted the renovations in high-energy-density and functional materials for almost every battery component [17-29], as well as the advancements in battery management and control for more sophisticated and reliable systems [30-34]. As the existing commercialized LIBs approaching their inherent capacity limits [3, 35, 36], it yet becomes unprecendentedly urgent ever in history to explore new materials and chemistry to go beyond the convention of LIBs [37]. The past four decades saw remarkable progress in improving battery performance from various perspectives [6, 38-45], particularly in developing and designing next-generation electrodes [1, 46-51]. Among all these efforts, Li metal, the ultimate anode material with ultrahigh theoretical capacity (3860 mAh/g) and low redox potential (-3.04 V vs. standard hydrogen electrode), received increasing attention worldwide [52-55]. However, the practical application of Li metal anode has been hindered by technical challenges such as low Coulombic efficiency, limited cyclability and unsatisfied compatibility [56, 57] as well as serious safety concerns associated with the dendritic morphology of Li electrodeposition [58-60], as shown in Figure 1-1.

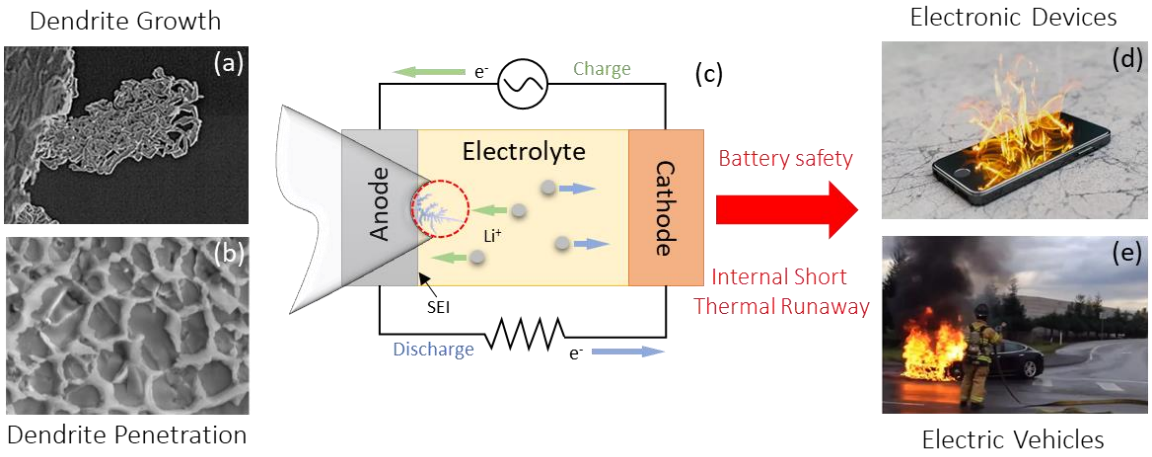

Figure 1-1. Challenges in Li metal anodes: (c) a schematic of dendrite growth during charge cycle in a Li metal battery; observation of (a) mossy dendrite morphology in liquid electrolyte and (b) dendrite penetration in solid electrolyte from SEM [61, 62], and (d-e) safety issues caused by Li dendrite growth.

These issues are strongly correlated to the intrinsic properties of Li metal and its electrodeposition process during each charge cycle. Firstly, Li metal is so chemically reactive that a complex of redox reactions take place instantly upon exposure to the electrolyte environment, forming a passivation layer at Li metal surface. This nano-thin layer is called the solid electrolyte interphase, named by Peled in 1970s as an important solid-state part of the electrolyte [63]. The formation of SEI consumes active Li and reduces the battery effective capacity [57, 64-66]. Secondly, unlike the Li intercalation processes in other anode materials such as graphite and silicon [47, 67-69], the electrodeposition at Li metal anode is a hostless process with higher spatial freedom and larger volume change [58, 70]. Therefore, the inhomogeneous electrodeposition at pristine Li metal anode can lead to Li dendrite growth even under moderate current densities [71, 72]. These formed dendrites may either peel off to become “dead Li” [73-75] and further decrease reversible capacity. Worse still, dendrites can even penetrate through separator to cause short-circuit at cell level, and a series of disastrous consequences at battery pack level, such as thermal runaway and fire [33, 76, 77] (Figure 1-1 (d-e)). Last but not least, the

synergistic effect of the two processes above may result in accelerated capacity fading and battery aging [78, 79]. Specifically, improperly plated Li above or within SEI layer can be partially or fully oxidized depending on the availability of electrons [80], which contributes to the formation of new SEI phase. And the huge volume change upon plating/stripping causes mechanical and chemical instability at the anode/electrolyte interface. Cracks can thus easily nucleate and propagate in the brittle SEI phase, exposing fresh Li metal surfaces to electrolyte environment and intensifying the new SEI formation at these uncovered sites. Meanwhile, these passive evolution of SEI layer accompanying Li plating may, in turn, produce more uneven current distribution, facilitating even dendritic growth of plated Li.

1.1.2 Dendrite formation mechanism and its suppression

To solve the dendrite issue in Li metal anode, it is critical to fundamentally understand the Li dendrite formation mechanism. Current consensus on the initial dendrite nucleation is mainly associated with the transport and charge-transfer kinetics at the anode surface and in the SEI layer [54, 81, 82]. Though accounting for the major cyclic capacity loss and Coulombic efficiency fading, a healthy and stable SEI is essential to the battery performance and life. As shown in Figure 1-2, during the charge cycle, two competing processes take place simultaneously at the anode/electrolyte interface: electron tunneling from anode to SEI (electrolyte) and Li-ion diffusion from electrolyte to anode. As mentioned previously, an ideal SEI layer serves as a Li-ion conductor and electron blocker, so that a Li^+ ion can (1) ionically diffuse/migrate though SEI and reach the Li metal surface, (2) meet with an electron and get reduced to Li^0 atom, and (3) rest and bond to a local energy minimum site. Smooth plating surface will be harvested if the Li diffusivity, electronic conductivity, SEI thickness, space charge distribution, etc. are uniform across the interface. However, SEI layer can hardly remain intact and uniform throughout the

whole calendar life, and the initial anode surface usually cannot be ideally smooth in a real battery cell. Most dendrite growth starts with these slight errors in homogeneity and the subsequent electrodeposition further amplifies the propagated inhomogeneity to form the observed dendritic morphologies of plating. For example, if an unhealthy region (e.g. a crack in SEI) appears at anode surface with either increased electronic tunneling or limited Li-ion transport, the local balance of electrochemical kinetics will break and the charge-transfer location will shift accordingly outwards into SEI layer and electrolyte. As such, isolated nuclei of Li metal are likely to form within SEI layer, which lose electric contact with Li metal anode and create unevenly-distributed space charge. These isolated Li metal nuclei can potentially lead to dendrite defoliation to become "dead Li". Therefore, to mitigate dendrite growth, the SEI should be electronically insulating enough to isolate anode and electrolyte from further reactions, yet Li-ion-conductive enough to sustain normal Li electrodeposition beneath it.

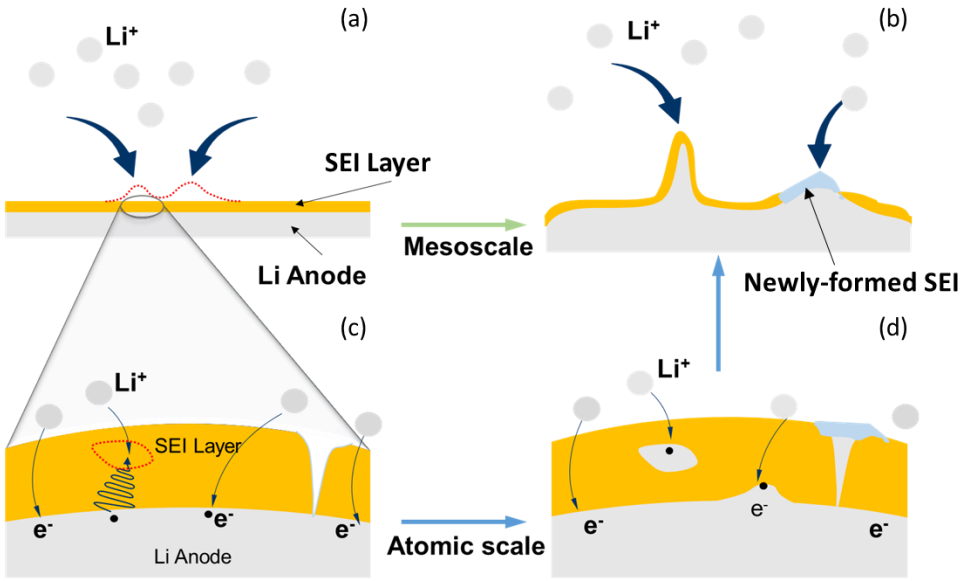

Figure 1-2. Schematics of dendrite formation mechanism: (a-b) Li dendrite and SEI growth at Li metal anode at macroscale, and (c-d) Li dendrite nucleation and crack-induced SEI formation at Li metal LIB anode at microscale. [82]

Based on the current understanding of dendrite growth mechanisms, extensive attempts have been deployed to the dendrite-free Li metal anode design in the past decades. Major efforts can be categorized from four perspectives: (1) optimized liquid electrolyte systems and new additives to alter the Li plating charge-transfer kinetics [2, 83-88], (2) artificial SEIs and anode coatings to improve the anode/electrolyte interface cyclic stability [89-93], (3) 3D electrode frameworks and matrices to spatially confine the electrodeposition morphology [94-98], and iv) solid-state electrolytes to mechanically suppress dendrite growth [99-103]. Despite the notable progress in enhancing the performance of Li metal anode accomplished by these works, there is still a long distance away from the practical application of Li metal batteries, since no optimal solution solves all the Li metal problems at once. For instance, in the majority of these attempts for liquid electrolyte systems, artificial coatings and 3D electrode matrices were widely employed to mechanically suppress or volumetrically accommodate the dendrite growth. Though effective as these approaches are in lowering the risk of separator penetration by metallic Li, their capability in maintaining high Coulombic efficiency and decent battery cyclability is limited, especially for those using micro-channeled or nano-porous structures with high surface ratio [94, 98] so that Li deposits can fill in densely without observably mossy or dendritic patterns. These methods failed to fundamentally solve the Li metal anode issues, since a great amount of new surface is still created during Li plating, where considerable amount of Li gets consumed irreversibly each cycle by forming new SEI. Solid electrolytes and all-solid-electrolyte batteries were once believed to be another promising solution for Li metal anode since the high-modulus solid electrolyte phase can easily stop dendrite growth and penetration [104]. However, new issues soon appeared when researchers observed the dendrite intergranular growth in polycrystalline ceramic electrolyte [62, 105] along with its intrinsically low ionic conductivity and interfacial challenges [106]. New liquid electrolyte systems and additives design can optimize the charge-transfer energy landscape and control the electrochemical kinetics, which is

one of the ultimate directions to fundamentally solve the dendrite issue. In spite of the limited number of excellent works such as the design of self-healing electrolyte [107], developing of a new electrolyte system generally takes more efforts and longer period.

1.2 Modeling of Li metal anode and dendrite growth

Computational modeling has been a powerful "green" tool to theoretically understand the electrodeposition kinetics and dendrite formation mechanism at different temporal and dimensional scales that might otherwise be experimentally costly, or even beyond detection limit. In a real battery cell, the length scale of Li dendrite morphology is usually around tens of microns; the actual electrodeposition reaction takes place within a nano-scale SEI layer; yet the ionic transport behavior and charge-transfer processes are at atomic and electronic scale. Therefore, a comprehensive understanding of Li dendrite growth requires the integration of multiscale techniques. In this part, we present a brief review on modeling works of Li electrodeposition and dendrite growth at different scales to demonstrate how multiscale modeling supports, compliments and guides the experimental works.

1.2.1 Atomic scale interpretation of dendrite nucleation at Li metal anode

Density functional theory (DFT) based atomic calculation and modeling have played an important role in understanding Li electrodeposition, SEI formation and dendrite nucleation at Li metal anode. Despite the calculation size limit of a few hundred atoms, DFT calculations are able to accurately capture the complex of redox reactions and charge-carriers transport behaviors at the anode/SEI/electrolyte interfaces. Chen et al. [108] calculated the electronic structures and Li

migration energy barriers along major diffusion pathways of the three main components (Li_2CO_3, Li_2O, LiF) of inner SEI layer from DFT bulk study. Pan et al.'s [109] work on defect physics in LiF demonstrated that the defect formation and Li ion conduction through SEI components is very sensitive to the external potential of the electrode. For SEI/electrode interfacial study, Leung et al. [110] combined constrained density functional theory (cDFT) and ab initio molecular dynamics (AIMD) to investigate the solvent decomposition at atomic layer deposition (ALD)-Al_2O_3 coated Li metal electrode, elaborating that the electron transfer rate at the electrode surface is lowered due to the coating layer, and further confirmed that the ALD coating reduces electrolyte decomposition effectively. Panahian et al. [111] developed a DFT method to study the interfacial properties of single layer crystalline LiF nanocluster grown on graphene surface, demonstrating the bilayer interfacial stability of different orientations and the electrostatic effects on the atomic structure of SEI layer in LIBs. Santosh et al. [112] provided a first-principle method to study the point defect diffusion and electronic properties at Li/γ-Li_3PO_4 electrode-electrolyte interface in solid state LIBs, revealing that the high formation energy of Li ion defects leads to the low conductivity across the interface, which is further affected by both mechanical strain and impurities. Lepley et al. [113] applied a DFT method to study the Li ion transport and interfacial properties of the two promising solid electrolyte materials, Li_3PS_4 and Li_3PO_4, reporting that the latter forms more stable idealized interface with Li metal. Most of the atomic works were focused on a nano-sized defect-free volume at a regularly-terminated surface or simply-oriented interface due to the limit of computational power. Although the real scenarios are far more complex, the simplified atomistic models [112, 113] still provide important insights on reaction kinetics and interface electrochemistry.

1.2.2 Continuum level modeling of electrodeposition and dendrite growth

Electrodeposition and dendrite growth are two of the most well-studied topics in traditional electrochemistry and solidification theories, respectively. And continuum modeling methods were most commonly used to deal with these problems at mesoscale. However, the dendrite growth associated with Li metal anode has been a tough problem due to the complicated surface electrochemistry. In the last half century, quite a few models were developed to address the Li dendritic growth problem at continuum level. The first attempt to model the growth of a needle-like dendrite tip was made by Monroe and Newman [114, 115] in a Li-polymer cell with invariant concentration and electric potential fields. Akolkar et al. [116, 117] extended this model by incorporating steady-state diffusion and temperature effects on Li-ion transport and electrochemical surface reaction. Furthermore, the 2-dimensional dendritic growth of electrodeposits were realized by Aryanfar et al. [81] and Nielsen et al. [81] via Monte Carlo simulation and finite element method, respectively. In these sharp-interface models, however, Li plating tendency is often determined by the local concentration or voltage, which would be crucially impacted by the temporal morphology change of Li metal phase they failed to consider or mathematically struggled to include. Advantageous in explicitly modeling the complex morphological evolution coupling ion/electron transport, electrode reaction, mechanical deformation and fracture, etc. [118], phase-field method was then drawn wide attention and extensively applied to model the electroplating processes. The major challenge confronted with phase-field modeling in electrodeposition is how to incorporated the nonequilibrium Butler-Volmer kinetics at the evolving reaction-surface to the conventional thermodynamics of Cahn-Hillard and Allen-Cahn frameworks. To overcome this difficulty, Liang et al. [119] developed a nonlinear phase-field model to describe the electrode reaction kinetics, which was further employed by Chen et al. [120] in metal electrodeposition to predict the dendrite growth patterns

under different electrochemical conditions. Meanwhile, Bazant et al. [121] summarized a general theory of chemical kinetics associating phase-field model with nonequilibrium thermodynamics. These efforts paved the way for the vast applications of phase-field method in electrochemical systems [122-126]. Due to the lack of database, however, a general dilemma facing mesoscale modeling is usually the choice of physical parameter inputs, which yet directly affects the feasibility as well as reliability of the simulation.

1.2.3 Phase-field model of metal electrodeposition

Phase-field method is a continuum modeling tool for microstructure evolution study during phase transformations, chemical reaction, transport, etc., which is thermodynamic-consistent to integrate multiple physical fields. Unlike other continuum model with sharp interfaces, the phase-field method uses a diffuse interface description [118]. In a general phase-field model, order parameters employed to distinguish different phases vary continuously across the phase boundaries with finite width. The temporal evolution of the microstructure can be realized by solving partial-differential formed governing equations describing the kinetics of the phase field. These governing equations are formulated based on Allen-Cahn or Cahn-Hilliard theories.

General phase-field models assume linear correlation between evolution rate and driving forces, which breaks down when systems goes highly out of equilibrium such as Li plating. Therefore, the phase-field model of electrodeposition was developed by incorporating the nonlinear Butler-Volmer kinetics to the conventional phase-field formulation based on Allen-Cahn theory. Current conservation and ionic diffusion are solved simultaneously with the evolving plating morphology. This model is capable to capture and investigate the electrodeposition behavior along with electrostatic field and concentration field evolution.

1.3 Research Objectives

The present research aims to solve the Li dendrite growth issue and facilitate Li metal battery design by combining phase-field-based multiscale modeling method and experimental techniques. The specific objectives of the dissertation are: (1) to fundamentally understand Li dendrite formation mechanism and the role of SEI layer from coupled atomic calculations and TOF SIMS techniques; (2) to develop a general modeling framework to predict Li dendrite morphology evolution in both liquid and solid electrolytes during electrodeposition and stripping; (3) to capture the electrochemical-mechanical driving forces and incorporate the impact of an nm-thin SEI in liquid-electrolytes as well as of the microstructures of nano-thick solid electrolytes for all-solid-state batteries; (4) to theoretically interpret experimental phenomena and accelerate the practical adoption of Li-metal electrodes in current and emerging battery technologies.

1.4 Dissertation structure

This dissertation contains six chapters: (1) Introduction, (2) Li metal anode/SEI interface study from density functional theory, (3) SEI formation dynamics investigated by TOF SIMS analyses, (4) Phase-field modeling of dendrite growth in liquid electrolyte, (5) Phase-field modeling for solid electrolyte design, and (6) Conclusions and future work.

In Chapter 1, the urgent demands for high-energy-density batteries and the challenges in developing practical Li metal anode were introduced. Then, Li dendrite growth, the toughest issue associated with Li metal anode was elaborated. The role of computational modeling tools in

understanding dendrite growth mechanism and promoting Li metal battery design was also discussed.

In Chapter 2, the interface of Li metal and solid electrolyte interphase (SEI) layer was investigated from density functional theory (DFT)-based atomic calculations on the two major SEI inorganic components, Li_2CO_3 and LiF. The mechanical properties of the most energetic-favored Li/Li_2CO_3 and Li/LiF interfaces were studied by calculating and comparing their interfacial energies, elastic energies and works of adhesion, etc. Their electrochemical properties were also checked from interface density of states (DOS) and electrostatic potential profiles. Based on these results, the tendency of dendrite nucleation and at each interface was discussed and basic rules for dendrite-suppression coating design were generalized.

In Chapter 3, the growth dynamics of solid electrolyte interphase layer during initial formation cycle at Li metal anode was revealed from experimental surface characterization techniques. An isotope-assisted time-of-flight secondary ion mass spectrometry (TOF SIMS) analyses method was developed to correlate time to isotope ratio and record the temporal information of SEI formation process. The unveiled SEI formation mechanism was then linked to the SEI two-layer structure and reaction kinetics to promote the in-depth understanding of SEI-formation-coupled Li electrodeposition/dissolution, and assist electrolyte additives and artificial electrode coatings design.

In Chapter 4, a general phase-field model of metal electrodeposition was developed coupling charge-transfer kinetics and mesoscale morphology evolution via transition state theory. Based on the multiscale model, the dendritic Li plating and non-dendritic Mg plating processes were simulated and compared to investigate the intrinsic mechanism of electrodeposition dendrite formation. Then, a parametric study on the major properties that differ between Li and Mg plating was carried out to generate a plating morphology transition map. This study pointed out the origin of Li dendrite growth and the most efficient way for dendrite-free Li metal anode design.

In Chapter 5, an extended phase-field model for Li electrodeposition in polycrystal solid electrolyte was developed by incorporating multiphase solid mechanics and explicit dendrite nucleation. Firstly, the model was validated by standard tests and comparing with existing models. Then, the Li plating morphologies in a simplified three-grain solid electrolyte system with a perpendicular crack and a perpendicular grain boundary were investigated. The impacts of major solid electrolyte properties (i.e. modulus, Li ion conductivity, grain boundary adhesion energy and surface electron density) on Li plating morphologies were quantitatively analyzed and summarized in terms of dendrite amount and penetration depth in the crack and grain boundary, respectively. The grain size influence on plating morphology was further examined by Li plating in polycrystal solid electrolyte structures with different controlled grain sizes generated from phase-field grain growth simulations. This model captures major existing failures in all-solid-state batteries including dendrite intergranular growth and isolated nucleation, and accelerates the optimization of solid electrolyte design.

In Chapter 6, the dissertation is summarized with some major conclusions listed. Some future directions related to the topic of the dissertation were further discussed. Major innovations are associated with the phase-field model of solid electrolyte, including incorporating Li metal plasticity and creep deformation, enabling crack initiation propagation and dendrite intragranular penetration, introducing the interlayer or second phases, etc.

Chapter 2
Li metal anode/SEI interface study from density functional theory

2.1 Introduction

The Li electrodeposition and dendrite growth are strongly correlated to the properties of SEI, the passivation thin layer between electrolyte and electrode. Electrolyte solvents, such as ethylene carbonate (EC) and dimethyl carbonate (DMC) will naturally reduce and decompose at the low potential Li metal surface and spontaneously form a SEI layer [80]. First proposed by Peled in 1970s [63], SEI remains "the most important but least understood" [127, 128] in rechargeable LIBs due to its complicated content that is highly dependent on numerous factors such as electrolytes and additives [129], electrode surface [130, 131] and operating conditions [132]. Many recent efforts have been focused on using different electrolytes to alter the property of SEI or developing artificial coatings on the Li surface to mitigate dendrite growth. Therefore, it is important to understand how the SEI and coating properties may impact Li dendrite formation.

The property of SEI is closely associated with its composition and structure. The generally accepted model of SEI consists of a porous organic (*e.g.* $(CH_2OCO_2Li)_2$ and ROLi) outer layer near the electrolyte/SEI interface and a dense inorganic (Li_2O, LiF, Li_2CO_3, *etc.*) inner layer near the electrode/SEI interface [133-138]. This double-layer structure of SEI was confirmed by Lu *et al.*'s [139] TOF SIMS isotope experiments on SEI depth profiles. In a later study combining computation and experimental observations, first-principle calculation on Li_2CO_3 bulk by Shi, *et al.* [140] further proposes a two-layer/two-mechanism SEI diffusion model: pore diffusion in the outer layer and interstitial knock-off diffusion in the inner layer.

They also demonstrate that the charge transfer “rate-determining step” [141] in the LIB system is the Li ion transport in the dense inner layer of SEI. Therefore, in order to elucidate the transport related dendrite formation, it is important to understand the interface between the electrode (Li metal in this case) and the dense inorganic inner layer of SEI.

In this section, we studied and compared the electrochemical and mechanical properties of two important interfaces, LiF/Li and Li_2CO_3/Li associated with SEI at a Li metal anode, by DFT method. The choice of these two systems is based on the fact that LiF and Li_2CO_3 are two major components in the inner inorganic SEI layer and closely related to the overall properties of SEI. Supercells with incoherent sharp interfaces are carefully constructed based on interfacial orientations and in-plane misfit minimization. Then energetics of each interface (*i.e.* interfacial energy, strain energy and work of adhesion) are calculated for mechanical stability evaluation. The density of states (DOS) and electrostatic potentials profiles of each interface are also plotted for electrochemical analysis. This will shed some light on the electron transport from Li through the SEI component, thus help us understand where Li metal will nucleate (near the interface or inside the SEI). This work also aims to provide a straightforward and effective way to predict and evaluate the overall properties of the two major SEI components, LiF and Li_2CO_3, from interfacial studies.

2.2 Description of the atomic model and calculation methodology

2.2.1 Interface orientations and supercell construction

We use several rules to build the periodic dense interfacial supercells. (1) Interfacial orientations: Based on the surface studies, orientations with the lower surface energy and similar in-plane lattice type were selected for Li, LiF and Li_2CO_3. (2) Sufficient number of atomic layers

of each phase (more than the minimum layer number for each surface energy to converge) is used along the selected directions, in order to minimize interactions between the two interfaces (total layer thickness larger than 10 Å for each phase). (3) Symmetry: At least an inversion (*P -1*) symmetry should be included in the constructed interface structure to guarantee the equivalency of the two interfaces in one supercell and preclude dipole moment (computation efficiency purpose). (4) Interfacial terminations: Only stoichiometric interfacial terminations are studied in this work. (5) Misfit: The artificially added in-plane strain to match the two parts in the interface structure should be less than 5%.

2.2.2 Surface energy calculation

The surface energy from slab method is the difference between the total energy of the relaxed slab structure and the bulk energy with the same number of atoms. The thickness of slab and vacuum layer is assumed to be large enough to neglect the interaction between the two surfaces of the slab (At least 10 Å vacuum layer is tested and added between slab surfaces in this calculation). The surface energy can be expressed as

$$\gamma = \lim_{N\to\infty} \frac{1}{2S}(E_{Slab}^{N} - N \times E_{Bulk}) \quad (2\text{-}1)$$

where E_{Slab}^{N} is the total energy of the relaxed slab containing N units, E_{Bulk} is the unit bulk total energy, S is the surface area, and the coefficient 2 indicates two equivalent surfaces in the supercell. To avoid error caused by E_{Bulk} calculation with different supercells and different $\boldsymbol{k}$-point mesh from E_{Slab}^{N}, Fiorentini and Methfessel method [142] was applied to obtain E_{Bulk} by linear fitting the slab supercell total energy data versus N and taking the slope of the straight line to reach the converged surface energy values efficiently with least atomic number of layers.

2.2.3 Definition of interfacial energetics and their calculations

The difference between the energy of the fully relaxed interface structure and the energy sum of the two stress-free pure phases with the same atomic unit numbers is defined as interface formation energy. For an interfacial supercell of constituents A and B, the interface formation energy, E_f, can be written as

$$E_f = E_{AB} - N_A E_A - N_B E_B \quad (2\text{-}2)$$

where E_{AB} is the total energy of the fully relaxed interfacial supercell, containing N_A units of A and N_B units of B. E_A and E_B are the energy per unit of the stress-free pure A and B bulk structure, respectively. To form a coherent interface without any lattice mismatch dislocations, the lattice mismatch of A and B needs to be small. The formation of the AB interface can be separated into two steps: first A and B slabs need to elastically deform to the common simulation cell length, then they join and form a coherent interface. Thus, the interface formation energy is separated into strain energy and interfacial energy corresponding to the two steps, and expressed as

$$E_f = 2S\tau + VE_{Elastic} \quad (2\text{-}3)$$

where τ is the interfacial energy, V is the fully relaxed cell volume, and $E_{elastic}$ is the elastic strain energy per unit volume. S is the interfacial area and the factor 2 in front of S is due to the two interfaces in one interfacial supercell. Equation 2-3 will allow us to evaluate the contribution of the strain energy and compare the chemical contribution of forming an interface when different strain needs to be applied form interfaces of varying orientation and materials.

The following method [143] was applied to separate the two energies. First, the constructed interface structures were fully relaxed (with respect to cell volume, shape and atomic coordinates) to their external stress-free states. Then, pure A and B bulk structures with the same interfacial geometry and similar atomic layer numbers, were relaxed along interface normal

direction (z) respectively, with fixed strained in-plane (x and y) lattice vectors obtained from the fully relaxed interfacial geometry. Same k-point mesh and cut-off energy were used for the two steps. The interfacial energy can be then calculated by

$$\tau_{AB} = \frac{E_{AB(xyz)} - N_A E_{A(z)} - N_B E_{B(z)}}{2S} \quad (2\text{-}4)$$

where $E_{AB(xyz)}$ is the fully-relaxed total energy of the interfacial structure. $E_{A(z)}$ and $E_{B(z)}$ are the energy per atomic layer of the pure A and B bulk structures after constrained relaxation along interface normal direction (z direction) with fixed x and y lattice vectors. N_A and N_B are the atomic layer numbers of A and B in the interfacial supercell, respectively. The elastic strain energy is then written as

$$E_{Elastic} = \frac{E_f}{V} - \frac{2S\tau}{V} \quad (2\text{-}5)$$

With all the calculation results, the work of adhesion of the interface can be expressed as

$$W_{Adhesion} = \gamma_A + \gamma_B - \tau_{AB} \quad (2\text{-}6)$$

where γ_A, γ_B and are the surface energies of A and B from unstrained slab method, respectively. τ_{AB} is the interfacial energy of A/B interface.

2.2.4 First-principles calculations

DFT calculations in this work were performed using Vienna Ab-initio Simulation Package (VASP) [144, 145] with plane wave basis sets and projector-augmented wave (PAW) pseudopotentials [146]. The exchange-correlation (X-C) functionals are treated within the generalized gradient approximation (GGA) of Perdew-Burke-Ernzerhof [147] revised for solids (PBEsol) [148]. Valence electron configurations for each element are as follows: $1s^2 2s^1$ for Li, $2s^2 2p^2$ for C, $2s^2 2p^4$ for O, and $2s^2 2p^5$ for F. The cutoff energy for the plane-wave basis is 500 eV, which was tested and applied for all supercells. Bulk and surface studies of each material were

conducted prior to interface investigations. For the bulk structure optimization, Monkhorst-Pack ***k***-points mesh was tested and set to $10 \times 10 \times 10$, $4 \times 8 \times 6$ and $12 \times 12 \times 12$ for the conventional cells of Li (body-center cubic (b.c.c.), space group: $Im\bar{3}m$, No. 229), Li_2CO_3 (monoclinic, space group: *C2/c*, No. 15) and LiF (rocksalt structure, space group: $Fm\bar{3}m$, No. 225) respectively. Using slab method, the ***k***-points samplings were reset for surface structure optimization, based on the geometry of each structure with one ***k***-point in the surface normal direction and the same ***k***-point number in-plane as in the bulk calculations. The total energy of each interface structure was converged to 10^{-4} eV/supercell, while 10^{-6} eV/supercell criterion was used for bulk and surface supercells. The Hellmann−Feynman force was converged to 0.02 eV/Å. Methfessel-Paxton smearing (order equals 1) was used for Li metal and Gaussian smearing was used for Li_2CO_3 and LiF, with a 0.2 eV energy broadening in all cases. For the interface structure with extended supercells in each phase, a $1 \times 1 \times 1$Monkhorst-Pack ***k***-points mesh was used in the self-consistent calculations, whereas $3 \times 3 \times 3$ Monkhorst-Pack ***k***-points mesh was applied to obtain the density of states (DOS).

2.3 Results and discussion

2.3.1 Bulk and surface

The ground-state lattice constants of Li, Li_2CO_3 and LiF were calculated and tabulated with experimental values in Table 2-1, as a check of the methodology. The equilibrium geometries of the three determined by energy optimization with respect to lattice parameters are in agreement with experimental measurement. The surface energy results and minimum atomic

layer numbers needed to converge were listed together with available results from other computational and experimental works in Table 2-2.

Table 2-1. DFT calculated lattice constants for Li_2CO_3, LiF and Li with experimental references [141, 149, 150].

Material	Symmetry	Lattice Constants					
		a (Å)	b (Å)	c (Å)	α(°)	β (°)	γ (°)
Li_2CO_3	C/2c	8.355	4.991	6.139	90	114.543	90
Li_2CO_3 (Exp.)		8.359	4.974	6.194	90	114.789	90
LiF	$Fm\bar{3}m$	4.010	-	-	90	-	-
LiF (Exp.)		4.027	-	-	90	-	-
Li	$Im\bar{3}m$	3.437	-	-	90	-	-
Li (Exp.)		3.48	-	-	90	-	-

The calculated surface energy values of the three materials, as listed in the table, are well matched with the available experimental measurements. The lowest surface energy is usually in the most close-packed directions with least number of daggling bonds. For b.c.c. Li metal, the three low-indices surfaces, (001), (110) and (111), show close values of surface energies, with the lowest of 0.49 J/m^2 along (001) direction.

For monoclinic Li_2CO_3, (001) orientation has the lowest surface energy of 0.18 J/m^2, prominently smaller than the other two low-indices surfaces, $(\bar{1}01)$ and (110). For rocksalt-structured LiF, the (001) orientation has the lowest surface energy of 0.36 J/m^2, almost two times smaller than (110) direction. The LiF (111) surface is not energetically favorable due to net dipole along surface normal direction produced by alternating stack of F-only and Li-only layers.

Table 2-2. DFT calculated low-indices surface energies for Li_2CO_3, LiF and Li with experimental references [111, 151-154].

Material	**Li_2CO_3**			**LiF**		**Li**		
Orientations	**(001)**	**($\bar{1}$01)**	**(110)**	**(001)**	**(110)**	**(001)**	**(110)**	**(111)**
Layer # to converge	2	3	3	5	7	5	5	7
Surface Energy (J/m^2)	0.18	0.30	0.59	0.36	0.84	0.48	0.51	0.56
Other computation (J/m^2)	0.18	0.28	0.57	0.32	0.78	0.46	0.49	0.56
Exp. (J/m^2)				0.353		0.472		

2.3.2 Interface

Based on the surface energy results and construction rules elaborated in the method section, two LiF/Li and two Li_2CO_3/Li interfaces were built. The interface projection view in the interface normal direction of each matching counterparts are shown in Figure 2-1. Since Li is rather isotropic, the two lowest energy surfaces, (001) and (110), are both considered in the interface model. On the other hand, LiF and Li_2CO_3 are rather anisotropic, only the orientations with the lowest surface energy were considered. The supper lattice size of Li metal were selected to match the lowest energy surfaces, (001) of LiF and (001) of Li_2CO_3, respectively. Each surface was cleaved and expanded to match the counterpart, reducing the interfacial mismatches to ~3% for all interface supercells, as listed in Table 2-3.

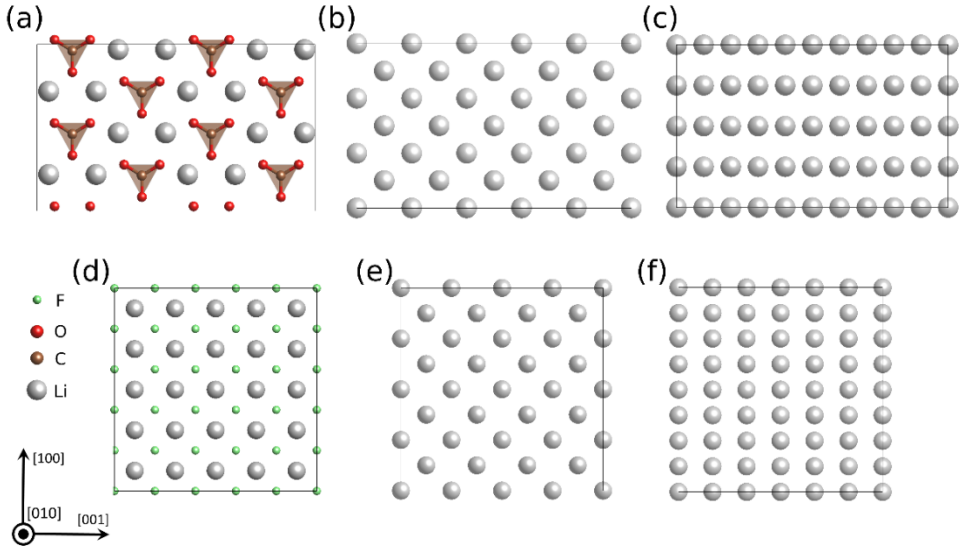

Figure 2-1. Top view of the atomic structures of each matching part in Li_2CO_3 (001)/Li interfaces: (a) 2×2 Li_2CO_3 (001), (b) 3×5 Li (001), (c) 2×5 Li (110), and each matching part in LiF (001)/Li interfaces: (d) 5×5 LiF (001), (e) 4×4 Li (001), (f) 3×4 Li (110), respectively.

Table 2-3. Misfit along the two in-plane directions upon interface matching for each supercell

Interface	Li(001)/Li_2CO_3(001)	Li(110)/Li_2CO_3(001)	Li(001)/LiF(001)	Li(110)/LiF(001)
Matching	3x5 / 2x2	2x5 /2x2	4x4 / 5x5	3x4 / 5x5
Misfit in [001]	2.76%	2.76%	2.78%	2.77%
Misfit in [010]	3.20%	2.67%	2.78%	2.78%

The initial as-constructed and the final fully-relaxed interfacial supercells of Li(001)/Li_2CO_3(001) and Li(001)/LiF(001) and interfaces are shown in Figure 2-2. Compared with LiF/Li interfaces, the relaxed Li_2CO_3/Li interfaces underwent drastic structural changes, indicated by the large distortion in the CO_3 groups near the interfacial region. By contrast, the relaxed LiF/Li interfaces experienced less lattice distortion, and instead, only slight atomic layer bending near interfacial region is observed. To further analyze the structural relaxation in

Li/Li_2CO_3 interface, the angle between CO_3 planar group and interface is defined as $A(CO_3\text{-}010)$ to characterize the structural relaxation. As shown in Figure 3, even $A(CO_3\text{-}010)$ in the same layer shows large variation due to the mismatch between Li lattice and Li_2CO_3 lattice. For example, in the interfacial supercell of $Li(001)/Li_2CO_3(001)$, the $A(CO_3\text{-}010)$ in Layer 1 (interface) varies from 16.8° to 22.7°. In Layer 2, it converges to 20°, which is close to the value in bulk Li_2CO_3 (18.6°). In the interfacial supercell of $Li(110)/Li_2CO_3(001)$, the divergence of $A(CO_3\text{-}010)$ is even larger. Even in the second layer, they still vary from 17.8° to 27.1°. This is quite different from what is observed in the model of Li_2CO_3 exposed to vacuum [155], where the $A(CO_3\text{-}010)$ is very close to its bulk value in the 2nd layer and the computed work function is converged when the Li_2CO_3 is more than 4 layers thick. The large distortion observed in the relaxed $Li(001)/Li_2CO_3(001)$ structure is primarily due to the prominent difference in the lattice type of Li metal (b.c.c.) and Li_2CO_3 (monoclinic). When interfaced with cubic Li metal, the tilted CO_3 tends to decrease the angle between the interface plane while still maintain the bulk-like structure, so that the total energy of the interface is minimized. The interface lattice mismatch in the model also causes more local structural variation in the interface model, and four layers of Li_2CO_3 may not be thick enough to recover the bulk structure in the middle of the slab yet.

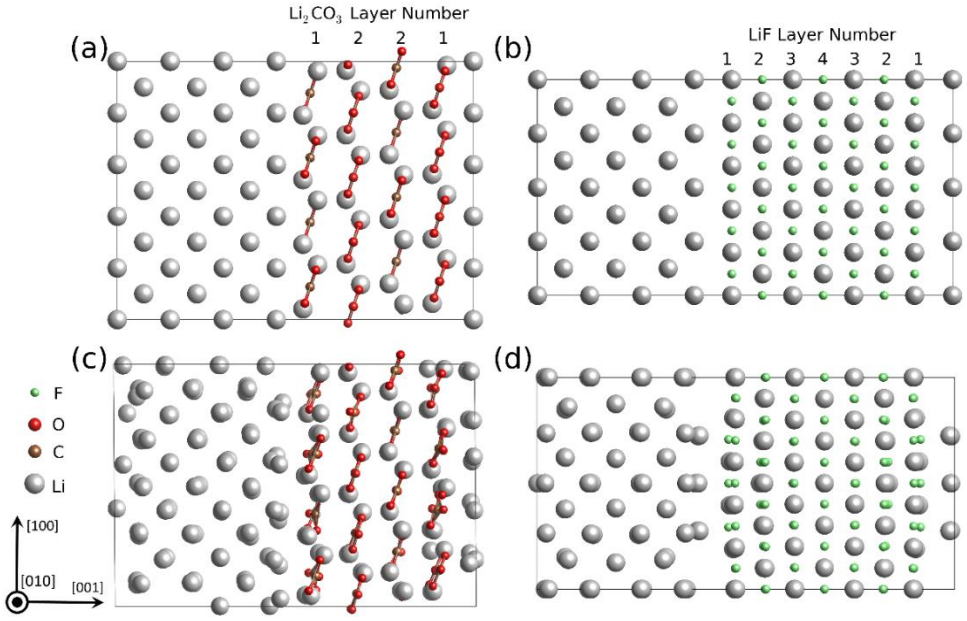

Figure 2-2. Atomic structures (with atomic layer labels) of the (a) as-constructed and (b) fully relaxed supercells of Li(001)/Li_2CO_3(001) interfaces, and the (c) as-constructed and (d) fully relaxed supercells of Li(001)/LiF(001) interface.

2.3.3 Energy calculations

The energetic calculation results of the four interfaces are tabulated in Table 4. Since the calculation results of elastic strain energies depend on how a supercell is constructed (interfacial misfit), the interfacial energy and work of adhesion results are used for the evaluation of interface mechanical stability. The work of adhesion is the energy cost to separate the two parts of the interface, and thus higher work of adhesion corresponds to better interfacial strength, and vice versa. The strain energy contributions to the total interface formation energy were also listed to further guarantee that each interface model was built reasonably with small elastic strain.

Table 2-4. DFT calculated energetics for different fully-relaxed interfacial supercells

	Li(001)/Li_2CO_3(001)	Li(110)/Li_2CO_3(001)	Li(001)/LiF(001)	Li(110)/LiF(001)
Formation Energy (10^{-18} J/simulation cell)	1.836	1.926	3.103	3.267
Interfacial Energy (J/m^2)	0.498	0.573	0.747	0.803
Work of Adhesion (J/m^2)	0.167	0.124	0.093	0.065
Strain Energy (MJ/m^3)	52.711	6.248	16.342	1.121
Strain Energy Contribution (%)	11.73	1.32	2.99	0.23

The work of separation of all four interfaces (0.065~0.167 J/m^2) are lower than the decohesion energy of the bulk materials, which is twice of the surface energy listed in Table 3. This means under tension, interface delamination is likely to occur. From the Li (001) and (110) orientations, the former shows higher work of adhesion and lower interfacial energy values in contact with either LiF or Li_2CO_3. Since Li (110) and (001) have similar surface energy, the interfaces with Li (001) are more stable when they both exist and are covered by LiF or Li_2CO_3, while (110) surface may become exposed again due to delamination. Meanwhile, Li_2CO_3 interfaces show only half of the interfacial energy and almost twice of the work of adhesion of LiF for either Li (001) or (110). This indicates that Li_2CO_3 as a SEI component on Li metal anode is more mechanically stable covering Li metal surface than LiF, and that Li_2CO_3/Li interface is less likely to delaminate than LiF/Li interface. The lower interfacial energy and the higher work of adhesion of Li_2CO_3/Li interface are closely related to the total energy decrease from larger lattice distortion after relaxation as mentioned above.

2.3.4 Density of states

In order to understand the influence of interfacial band structure variation on electrochemical property, the projected density of states (PDOS) was calculated for each fully-

relaxed interfacial supercell and split into the sums of different atomic layers in Li metal, Li_2CO_3 and LiF, respectively. The DOS curves of the two energetically-favored interfaces, Li(001)/LiF(001) and Li(001)/Li_2CO_3(001) are shown in Figure 2-3.

The DOS curves were found similar for each Li metal layer, so only the mid-layer Li DOS are presented here. However, the DOS curves for each LiF and Li_2CO_3 layer varies prominently from interfacial layer to bulk-like inner layer (Figure 2-3). Meanwhile substantial band offset can be observed in DOS curves from layer 1 (interface) to layer 4 (bulk-like) in LiF, and Layer 1 (interface) to layer 2 (more bulk-like) in Li_2CO_3.

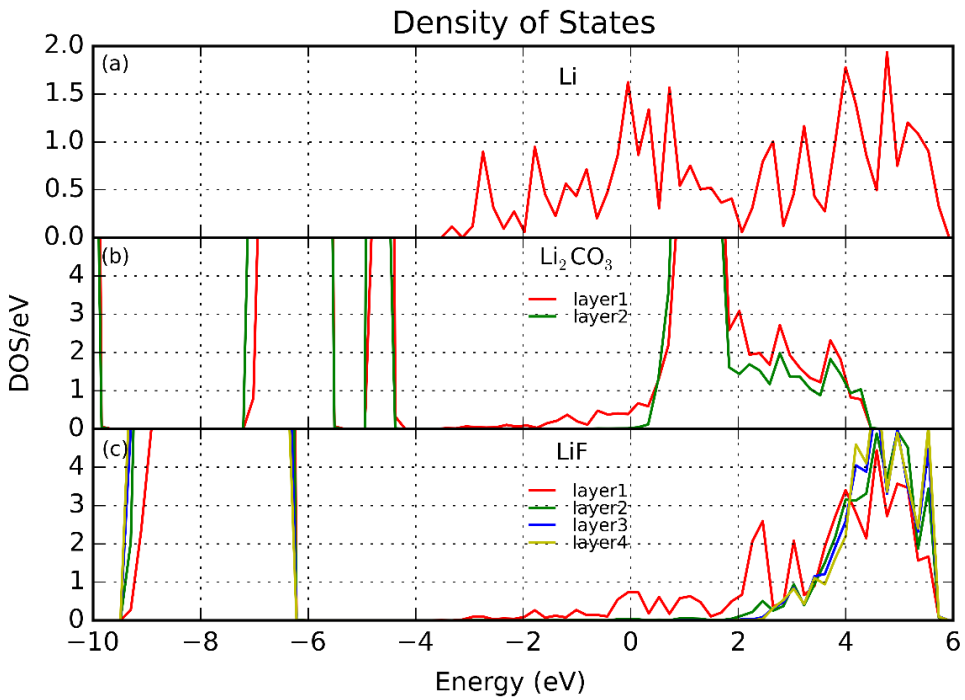

Figure 2-3. Density of states profiles by atomic layer with Fermi level at 0 eV: (a) mid-layer of Li metal in fully relaxed interfacial supercell, (b) layer 1 and layer 2 of Li_2CO_3 in fully-relaxed Li(001)/Li_2CO_3(001) interfacial supercell, and (c) layer 1 to layer 4 of LiF in fully-relaxed Li(001)/LiF(001) interfacial supercell.

This mainly results from the coupling effect with the band structure of Li metal and the influence of atomic structure reconstruction as already shown in Figure 2-2. As demonstrated in the relaxed interface, large distortion occurred inside Li_2CO_3 near the interface, where CO_3 layer tilted rather than staying planar. In comparison, the lattice distortion of LiF is much less. The electron tunneling barrier from Li to LiF or Li_2CO_3 can be read directly from DOS profiles by taking the difference of conduction band minimum (CBM) and Fermi level (0 eV). The electron tunneling barrier from Li to Li_2CO_3 (either layer 1 or layer 2) is close to 0 eV, which is much lower than the band gap value in bulk, indicating that two atomic layers of Li_2CO_3 is not insulating enough to block electron from migrating from Li metal to Li_2CO_3. In contrast, the electron tunneling barrier from Li to LiF increases from 0 (layer 1) to 1.8 eV at layer 2, and reaches 2.6 eV at layer 4, suggesting that LiF is more effective in blocking electrons from Li anode to SEI. Despite the limit in computational size, it still can be concluded that given the same thickness, LiF is more electronically insulating than Li_2CO_3 in terms of confining electrons within Li metal and thus to mitigate Li dendrite nucleation inside SEI. However, it is also possible that a thickness of 4 layers of Li_2CO_3 is not enough to reach the bulk band gap of Li_2CO_3. As analyzed in Figure 3, the planar CO3 groups are still tilted and have not converged to its bulk value in layer 2. Yet including more layers of Li_2CO_3 for the interface model is currently out of our computation limitation.

2.3.4 Electrostatic potential

In DFT calculations, the local potential, or local effective potential (U_{eff}) is a sum of local electrostatic potential (U_{elst}) and exchange correlation potential (U_{xc}), where the former includes ionic potential (U_{ion}) and Hartree potential (U_H). Therefore, the choice of exchange correlation potential has influence on the total local potential, but little impact on the electrostatic

potential. The difference between planar averaged U_{elst} and the U_{eff} exists near the core positions, and the detailed comparison of the two are in the supplementary material. Thus, in this section, the planar averaged electrostatic potential [6] along the interface normal direction is studied for each fully-relaxed interfacial supercell.

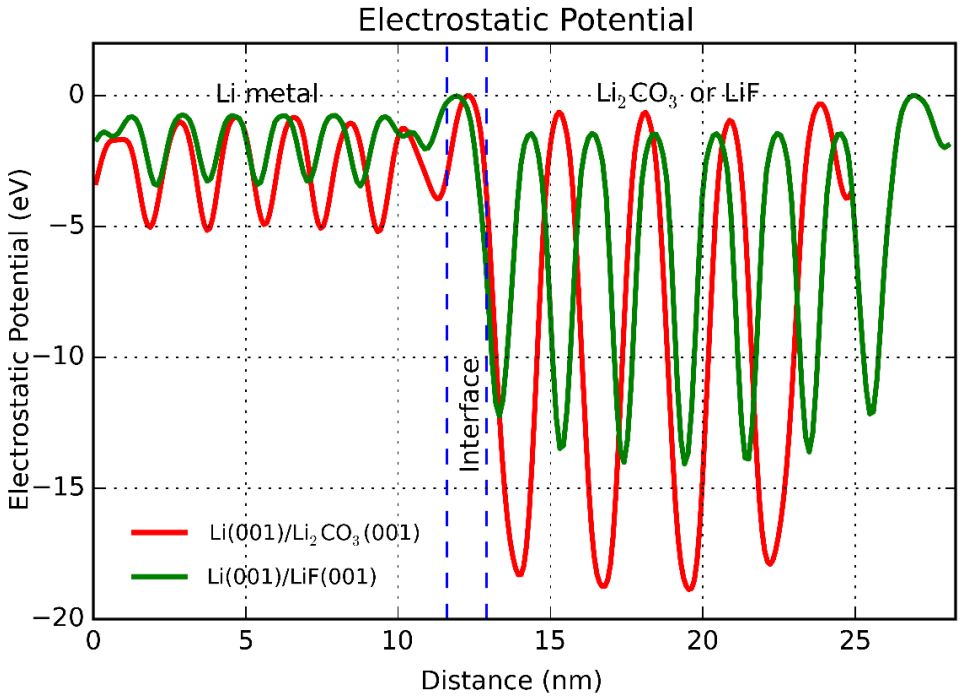

Figure 2-4. Electrostatic potential profiles of fully-relaxed Li(001)/LiF(001) and Li(001)/Li_2CO_3(001) interfaces with offset.

The ESP curves of the two energetically-favored interfaces, Li(001)/LiF(001) and Li(001)/Li_2CO_3(001), are shown in Figure 2-4. Similar trends are observed in ESP curves for other interfaces, which are shown in supplementary material. The potential curves oscillate within each phase while drop substantially at the interfacial region. Each valley of the curves can be treated as the approximated position of an atomic layer. The highest occupied electron level in each phase can be roughly estimated by taking the average of peak values. Therefore, the Fermi level difference between Li metal and 4-layer LiF is found much larger than 2-layer Li_2CO_3,

indicating higher work function in LiF phase over Li_2CO_3 phase with respect to Li metal. This conclusion is in agreement with and supplementary to our DOS calculation results.

According to Figure 1-2, if the electrons are well blocked beneath the SEI layer, Li should continue to electrodeposit at the Li/SEI interface; otherwise it might form new Li metal nuclei inside the SEI, which is then undesirably isolated from the rest of electrode. Thus, LiF may favor Li growth at the Li/SEI interface, while Li_2CO_3, if not sufficiently thick, may form isolated Li metal inside SEI layer. Further experiments to compare these two coating materials would provide more insights to elaborate the role of SEI coating on Li plating.

2.4 Conclusion

In this chapter, to understand the mechanical and electrochemical properties of the SEI/Li interface, interfacial supercells were constructed by matching the two important inorganic SEI components, LiF and Li_2CO_3, to Li metal, and studied by using the DFT method. The calculated interfacial energy and work of adhesion of each interface show that Li (001) is the most energetically stable interfacial orientation and that Li_2CO_3 shows better interfacial mechanical stability than LiF in SEI. Further calculation on DOS and ESP of each interface provides the migration barriers of electrons from anode to SEI at each interface. Given either same atomic layer number or thickness, larger electron tunneling barrier was obtained for LiF/Li interface, denoting LiF having less electron tunneling probability than Li_2CO_3. Particularly, in charging cycles with limited Li ion transport from electrolyte to anode surface, undesirable Li dendrites are more likely to nucleate and grow within SEI at Li_2CO_3/Li than LiF/Li interfaces. Based on this DFT interfacial study, a map can be established by this method, linking SEI components to their mechanical and electrochemical properties, which can hardly be measured by state-of-art experimental techniques. Meanwhile, the energetic results obtained can be used as important

inputs to other meso-scale simulations, *e.g.* Li dendrite and SEI phase evolution during LIB working cycles. More importantly, this study on SEI/Li metal interfaces provides valuable insights to the design of LIB electrode protective coating material, or artificial SEI layer.

Chapter 3

SEI formation dynamics investigated by TOF SIMS analyses

3.1 Introduction

The stability and functionality of SEI layer is crucial to improving the calendar life and non-degrading cycling capacity of lithium-ion batteries (LIBs). However, the SEI formation dynamics is not yet well understood due to the limitations from both experimental and computational methods. Experimentally, some SEI analysis tools, especially the thin-film measurement techniques, need to be conducted in high vacuum instead of in the electrolyte systems [156-159]. Several *in situ* experiments unveiled valuable information on the compositional [159, 160], morphological [161, 162] and electrochemical [163] evolution during SEI growth. However, there is still very limited understanding on how the double-layer SEI structure build up or what reactions dominate at each step. Complimentary to experimental characterizations, various modeling methods on different scales were performed. Atomistic simulations, such as density functional theory (DFT) [82, 164], density functional tight binding (DFTB) [165], Monte Carlo (MC) and molecular dynamics [166] reactive force field (ReaxFF) [167] methods, can potentially capture the electrochemical reaction details of the SEI formation process. Nonetheless, both the temporal and spatial limits only allow these simulations to focus on the very short span of a local SEI formation process, *i.e.* specific redox reactions involving a limited number of molecules [80, 168]. In addition, most atomic scale dynamic simulations are based upon simplified models to reduce computation costs, such as crystalline structure systems, elevated temperatures, approximated description of bonding, *etc*. Continuum models, on the other hand, are able to simulate the complete SEI morphological evolution while lacking chemistry

details [120, 169], but key physical parameter inputs are usually difficult to obtain. Ushirogata *et al*. [170] proposed a "solution-mediated" mechanism for the initial stage of SEI formation via two-step *ab initio* molecular dynamics (AIMD) simulations, claiming that the electrolyte decomposition products will first desorb and form aggregates, then merge and absorb onto the anode surface to form the initial layer of SEI. Takenaka *et al.* [171] demonstrated a complete nanometer-thick SEI formation process with a two-layer structure, by a hybrid MD/MC reaction method to overcome the time and length scales. However, a constant reaction rate was assumed throughout the formation process in this model, where the surface voltage, chemistry, and the availability of electrons and solvents should gradually change as SEI layer grows thicker. Under such assumptions, a "top-down" SEI growth sequence was observed that new SEI layer forms on the top of the existing layer. This work is one of few that elaborates the electrochemical details of SEI formation from initial electrolyte decomposition to nanometer-thick layer buildup, but the simplified reaction rate presumption limits its predictive strength.

In this chapter, to understand the SEI growth dynamics, especially the dimensional buildup mechanism after the initial step of electrolyte decomposition, we hereby present an isotope-assisted time-of-flight secondary ion mass spectrometry (TOF SIMS) study to unveil the SEI growth sequence during a later stage of SEI formation in the first cycle. Moreover, it is widely accepted that SEI generally has a two-layer structure consisting of an outer organic layer and an inner inorganic layer. However, the kinetics of each layer formation, *i.e.* which layer forms first, what reduction reaction (*e.g.* one-electron or two-electron reactions) dominates during each layer formation stage, and if there exists any phase transition between the two layers, *etc.*, remain unanswered. In this study, by combining isotope tracer and TOF SIMS profiling, we will address in-depth, for the first time, all these relevant questions and interpret the revealed dynamics of SEI formation during the first cycle at a pristine anode.

3.2 Description of the isotope-assisted TOF SIMS method

3.2.1 Sample preparation

Li|Cu coin half-cells were prepared with Cu foil (25 μm thickness, 12 mm in diameter) as working electrode, pure ^{7}Li metal of the same size as counter/reference electrode, and isotope labeled 1M $^{6}LiBF_4$ in 1:2 ethylene carbonate (EC): dimethyl carbonate (DMC) as electrolyte (Figure 3-1 (a)). The choice of non-Li insertion Cu as electrode eliminated the complication of Li insertion and thus all Li signal observed can be attributed to the SEI. [138] The coin cell was cycled for a half SEI formation cycle under constant current constant voltage (CCCV) condition: first discharged galvanostatically at 0.005 mA from open circuit voltage (OCV) to 0.025 V, and then held at 0.025V for 10 h until the current dropped to less than 0.001 mA for SEI layer formation on the Cu electrode (Figure 3-1 (b)). After SEI formation, the Cu electrode was harvested by dissembling the cell in an Ar-filled glovebox. The SEI layer formed on Cu foils were soaked in DMC for 15s and then rinsed thoroughly with DMC to remove the electrolyte residuals. The harvested electrodes were dried in Ar prior to subsequent characterizations and analyses. For TOF SIMS analyses, a sealed apparatus was used for SEI sample transfer to avoid air exposure.

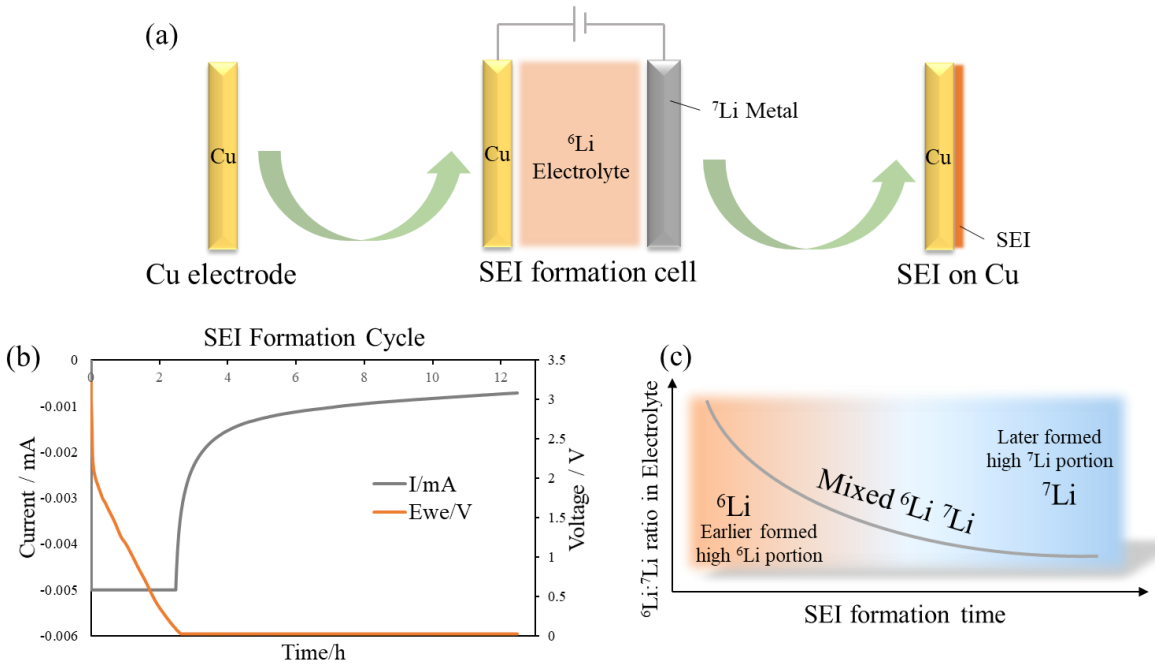

Figure 3-1. (a) Schematic of sample preparation from a coin cell, (b) the I-t and V-t curve under CCCV for SEI formation cycle and (c) Li isotopes ratio variation trend over time in the cell electrolyte during formation cycle.

3.2.2 Instrumentation

The TOF SIMS analyses were conducted on a PHI TRIFT V nano TOF spectrometer (Physical Electronics, Chanhassen, MN) with a 30 kV Au^+ ion source for both sputtering (~0.1 nm/s calibrated by 100 nm SiO_2) and analysis. The analysis chamber of the instrument was maintained at a pressure of less than 5×10^{-7} Pa during operation. A 50 $\mu m \times 50\ \mu m$ analysis area was used within a sputter area of 200 $\mu m \times 200\ \mu m$. A PHI Quantera XPS Scanning Microprobe (Physical Electronics, Chanhassen, MN) with a monochromated Al Kα source (1486.6 eV) was employed for the XPS analyses. The base pressure of the system was maintained less than 2.5×10^{-7} Pa. A 1 kV Ar ion source was used for sputtering, and the sputter rate was ~2 nm/min calibrated on a 100 nm SiO_2 thin film. SEM images were taken by Hitachi S4800 field

emission SEM. The SEI formation and electrochemical measurements were performed by Biologic VMP3 potentiostat.

3.2.3 Experiment design

To investigate SEI growth kinetics, isotope-assisted TOF SIMS was developed as an approximation of *in situ* diagnostic method. By combining isotope tracer and TOF SIMS profiling, this method is able to "record" the time-dependent information during SEI growth. Briefly, while the ^{6}Li enriched electrolyte is continuously reduced to form SEI at the Cu electrode surface, ^{7}Li from the pure ^{7}Li metal electrode dissolves into the electrolyte to compensate the Li^{+} consumption. Therefore, considering a case of ideal mixing under the applied CCCV condition, the overall ^{6}Li:^{7}Li ratio in electrolyte would decrease over time. The timescale of SEI growth can thus be represented by the ^{6}Li:^{7}Li ratio in the SEI, and each ^{6}Li:^{7}Li ratio corresponds to a snapshot point on SEI growth timeline: the initially formed SEI layer should have higher ^{6}Li:^{7}Li ratio than the subsequently formed SEI portion (Figure 3-1 (c)). With this method, the encoded SEI growth dynamics can be extracted out even after the growth process has completed.

3.3 Results and discussion

3.3.1 The bottom-up formation dynamics of SEI layer

The normalized intensities of selected ion fragments from the harvested SEI on Cu after formation cycle was measured with TOF SIMS as a function of sputtering depth into SEI (Figure 3-2). In all depth profiles, depth 0 refers to the SEI topmost surface at the electrolyte/SEI interface. Higher depth number indicates the location in the SEI closer the Cu electrode.

Combining the intensity variation trends of Cu^+ and of the other composition representative species of SEI, i.e. $C_2H_2^-$ and Li_2F^-, the SEI/Cu interface position (taking the midpoint of a 60 nm diffuse interfaces) can be defined at around 30 nm (*i.e.* SEI thickness ~ 30 nm). In Figure 3-2 (a), higher ^6Li:^7Li ratio was observed near the electrolyte/SEI interface, while lower ^6Li:^7Li ratio was found near the SEI/Cu interface, indicating that the SEI portion near the electrolyte formed first (higher ^6Li:^7Li ratio), and the SEI portion near the electrode formed last (lower ^6Li:^7Li ratio). This decreasing trend of ^6Li:^7Li ratio indicates that SEI formation spatially follows a "bottom-up" sequence, where new SEI forms at the SEI/electrode interface and pushes up the existing SEI layer as SEI grows thicker (Figure 3-3). This observation contradicts with Takenaka's "top-down" SEI formation sequence [171], suggesting that some assumptions in that model may not be valid, such as the constant transport properties of electrons and solvent molecules in the SEI during the SEI buildup process.

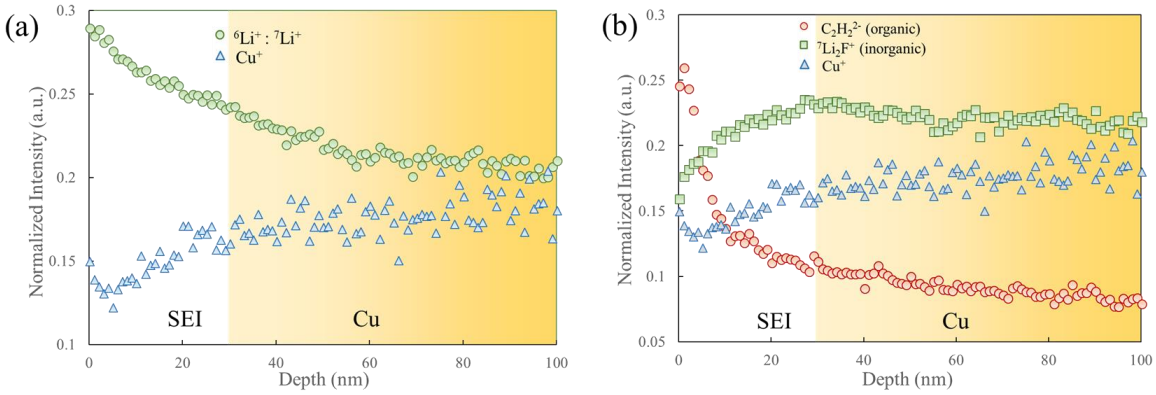

Figure 3-2. TOF SIMS depth profiles of the SEI on Cu electrode surface: (a) ^6Li:^7Li ratio and Cu^+ (b) $C_2H_2^-$ (organic), Li_2F^- (inorganic) and Cu^+. Intensities were normalized to total ion counts.

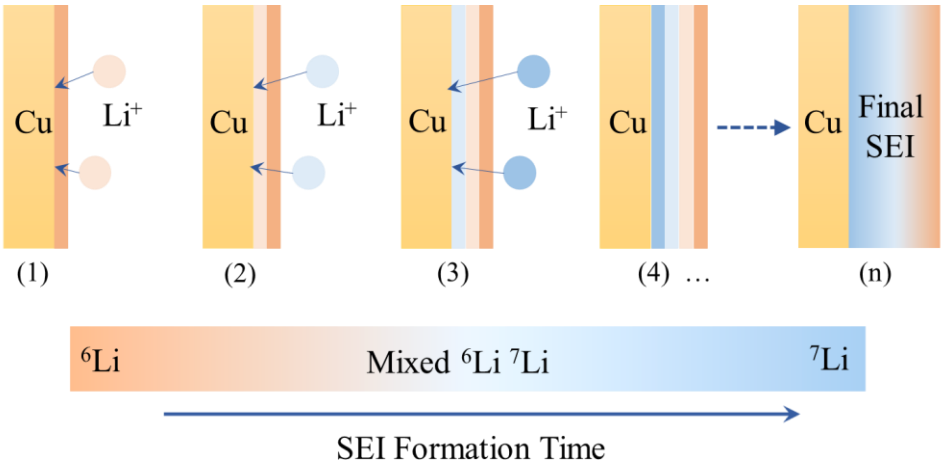

Figure 3-3. Schematic of SEI formation on Cu electrode in the initial cycle and the "bottom-up" growth mechanism interpreted by Li isotope ratio variation over time.

3.3.2 SEI chemistry analyses

To further reveal SEI growth kinetics regarding different SEI components, the composition of SEI at various depth was studied with TOF SIMS and XPS. In the TOF SIMS depth profiles (Figure 3-2 (b)), $C_2H_2^-$ fragment ion is taken as an indicator for organic species, while Li_2F^- fragment ion is indicative of LiF (an example of major inorganic species) in SEI. From SEI topmost surface near electrolyte to bottom surface near Cu electrode, the normalized intensities of $C_2H_2^-$ decreases while Li_2F^- increases. This opposite variation trends of organic ($C_2H_2^-$) and inorganic (Li_2F^-) depth profiles further confirm the double-layer structure of SEI: an organic outer layer interfaced with electrolyte and an inorganic inner layer interfaced with Cu electrode. It is consistent with the XPS observations of the SEI at various depths. The O1s spectra (Figure 3-4 (a)) shows the topmost SEI layer near electrolyte (0 nm) contains mostly organic components, such as polyethylene glycol or organic lithium salt (532.8 eV). While the SEI near Cu (30 nm) is rich in inorganic species, such as Li_2CO_3, LiOH, and Li_2O, indicated by the peaks of metal carbonates at 530.6 eV and metal oxides at 528.2 eV, respectively. The C1s XPS spectra

also demonstrate that most organic carbon species are found in the topmost SEI layer (285.0 eV, 286.5 eV), while little carbonaceous species were present near the Cu substrate. The composition and morphology map from the same SEI sample region are also obtained by TOF SIMS and SEM (Figure 3-5). From the $^{12}C^-$ and $^{16}O^-$ map, C and O containing species mostly uniformly presents in the as-formed SEI. LiF, indicated by $^{19}F^-$, tends to aggregate locally and form small islands. This is in agreement with previously reported observations, that LiF with strong Li-F bonding are mostly found in the form of crystalline particles intercalated in SEI [172].

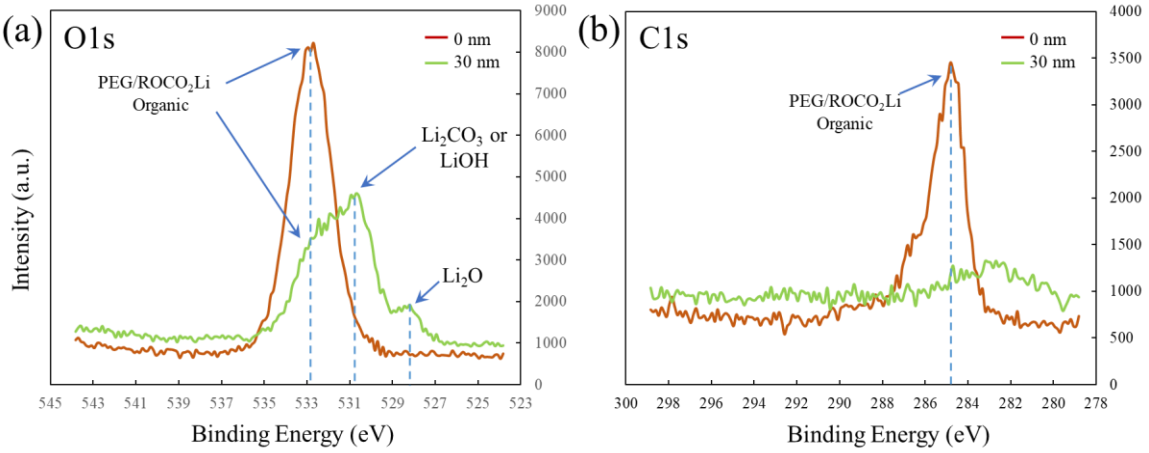

Figure 3-4. XPS spectra of SEI on Cu electrode surface: (a) O1s at the surface (0 nm) and 30 nm below the surface (b) C1s at the surface (0 nm) and 30 nm below the surface. The absolute intensities at different depths were scaled up for comparison purpose.

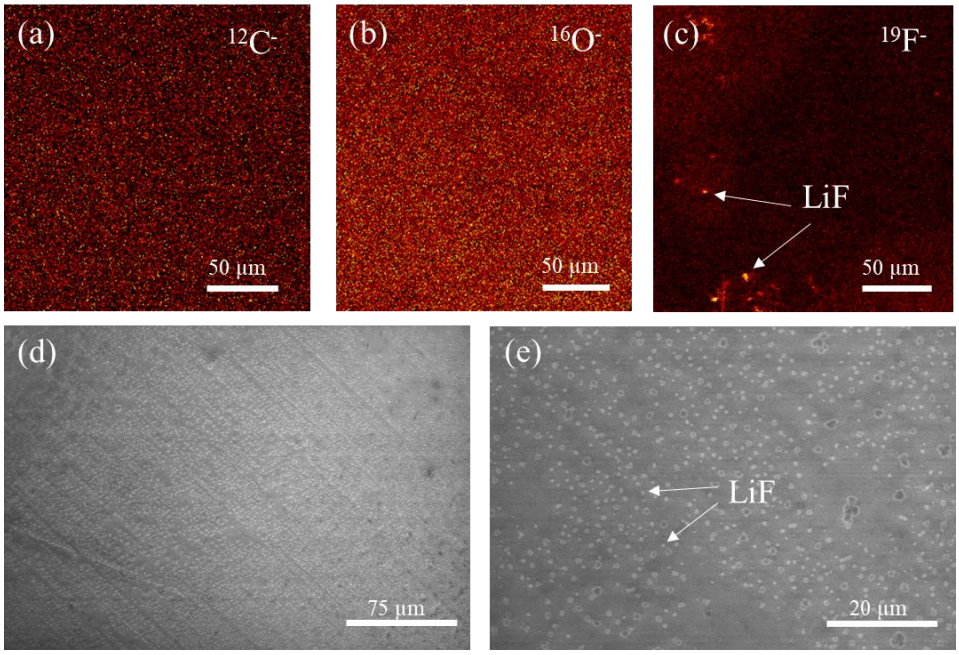

Figure 3-5. TOF SIMS composition maps of SEI on Cu electrode: (a) $^{12}C^-$, (b) $^{16}O^-$ and (c) $^{19}F^-$; (d, e) SEM images of SEI on Cu electrode at different magnification.

3.3.3 Interpretation of SEI formation mechanism

Combining the SEI growth sequence and its two-layer chemistry, several conclusions can be further drawn based on these analyses results. The TOF SIMS and XPS results together validate the double-layer structure of SEI: an organic layer near electrolyte and an inorganic layer near the electrode. Furthermore, the SEI growth follows a "bottom-up" mechanism: the organic components (*e.g.* poly-ethylene-glycol and organic lithium salt) form first on the electrode, then the inorganic components (*e.g.* LiF, Li_2CO_3, and Li_2O) form underneath the organic layer and push the as-formed layer up as SEI grows. It also can be inferred that the formation of inorganic components (*e.g.* Li_2CO_3 and LiF) is from the direct decomposition of the electrolyte, instead of multi-step conversion from formerly formed organic components. We propose the reason for this

bottom-up SEI growth mechanism is due to the competition between the availability of electrolyte and electrons. Initially, on the pristine Cu surface (similar mechanism should occur on graphite electrode surface), the electrolyte is abundant. Therefore, most solvent molecules will be reduced *via* one electron reduction mechanism, which favors organic species formation. And the electrode surface will be covered by the organic film, which has been demonstrated to be porous and allow both anions and solvents to transport. [173]. As the organic layer grows thicker, few BF_4^- anions and solvents (such as EC) will transport through the porous organic layer to the electron-rich electrode surface. Thus two-electron reduction reactions will then take place, which favors the direct formation of inorganic species, such as LiF and Li_2CO_3 . [80, 174] This mechanism is illustrated in Figure 3-6.

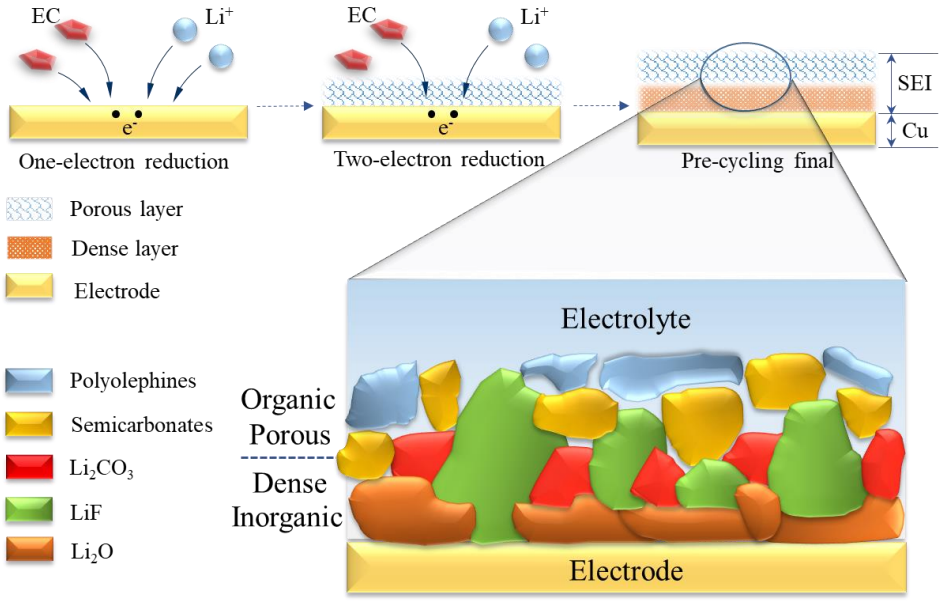

Figure 3-6. Schematic of complete SEI formation mechanism combining the two-layer structure chemistry and "bottom-up" growth dynamics.

3.4 Conclusion

In this chapter, the SEI structural and compositional evolution during formation is investigated. It is found that the SEI formation takes place at the SEI/electrode interface, and new SEI, especially the inorganic components, forms beneath the existing organic phase SEI, through a “bottom-up” process, as illustrated in the schematic (Figure 3-3 and Figure 3-6). This growth mechanism leads to the observed two-layered structure of SEI, where the organic layer is permeable for the electrolyte. This growth mechanism is related to the unbalanced electrolyte and electron concentrations that lead to first one-electron reduction reaction to form the organic layer and then the two-electron reduction reactions to form the inorganic layer at the SEI/electrode interface. It should be emphasized that the proposed growth mechanism may dominate only in the initial stage of SEI formation during the battery pre-cycling or the SEI “formation cycle”. This work provides insights for the SEI formation mechanism from a dynamical perspective, and the in-depth understanding of SEI formation assists electrolyte additives and artificial electrode coatings design. Future investigation on the SEI formation and evolution during calendar and cycle tests is needed. As an SEI grows thicker and more stable, other coupled growth mechanism may be responsible for the continuous SEI growth. Nevertheless, this novel isotope-assisted TOF SIMS approach can also be extended to address these questions.

Chapter 4

Phase-field modeling of dendrite growth in liquid electrolyte

4.1 Introduction

The dendrite growth issue severely hinders the application of Li metal as a high-energy-density anode for next-generation batteries. Experimentally, an overwhelmingly huge amount of effort has been dedicated to promoting the performance of Li metal batteries, yet the achievement has been limited. Theoretically, continuum models have attracted wide attention to fundamentally understand and solve the Li plating problem at mesoscale. However, the current awareness of dendrite growth remains empirical and phenomenological, and a comprehensive model has been missing to truly guide the dendrite-free Li metal anode design.

While Li metal is notorious for its dendritic growth during plating, Mg metal, another promising anode candidate for next generation batteries, drew wide attention for its non-dendritic polyhedral electrodeposition morphology [175-177]. Although designing electrolytes with applicable electrochemical windows [178, 179] and exploring high voltage cathodes of good charge-transfer kinetics [180] still remain challenging for Mg batteries, understanding the uniform deposition feature at the Mg metal anode might potentially provide useful hints to realize dendrite-free Li metal anodes.

Despite the extensive modeling works on the dendrite growth of metallic Li, Zn, *etc*. [120, 122-126], there have been limited number of studies to examine the differences in the properties of the dendrite-free Mg with other dendritic metals. Ling et al. [181] calculated the absorption energies and surface migration barriers in Mg and Li metals from density functional theory (DFT), claiming that the stronger Mg-Mg bond strength causes its non-dendritic deposit morphology.

Similarly, Jäckle et al. [182, 183] compared the self-diffusion barriers on Li, Mg, Na, Zn and Al metal surfaces calculated from DFT, and concluded that the smaller Ehrlich-Schwoebel barrier for adatom moving from an island to a lower terrace at Mg metal (0001) surface is strongly correlated to its tendency towards harvesting smooth deposition morphology. However, these works fail to incorporate the impact of electrochemical kinetics in an electrolyte environment, which extremely limits their interpreting power. Beyond these atomic scale calculations, there have been no major efforts to elucidate the intriguing plating behavior in Mg metal.

To explore the physical origin of such plating morphological discrepancy between Mg and other dendritic metal, a well-defined model for metal electrodeposition is need to embrace the complete electrodeposition kinetics at the anode/electrolyte interface. The metal electrodeposition process can be generally divided into four stages: (a) metal cation desolvation from electrolyte molecules, (b) cation ionic transport through passivation layer (if the anode surface is covered by SEI.), (c) charge-transfer at anode surface, and (d) adatom self-diffusion at anode surface. So far, only the last stage has been thoroughly investigated and compared between the pristine surfaces of Mg and other metals [181-183], which could be relevant yet is far from enough to conclude this topic. In this study, we hereby developed a multiscale model linking atomic level charge-transfer physics towards the mesoscale phase-field method incorporating transition state theory to capture the entire process of metal electrodeposition in a half-cell system. This model is capable of reproducing the Li and Mg deposit morphological difference while integrating their key physical parameters inputs from atomistic calculations. By parametric studies, the model reveals it is the lower exchange current density of Mg electrodeposition due to the larger desolvation energy in (a) stage, that is responsible for its non-dendritic plating morphology. Then we further apply the model to discuss the dendrite-free metal anode design for next generation batteries.

4.2 Phase-field model of metal electrodeposition in liquid electrolyte

4.2.1 Equilibrium thermodynamics

We consider a general metal electrodeposition, $M^{n+} + ne^- \rightarrow M(s)$, in a model regular solution liquid electrolyte half-cell system, illustrated in Figure 4-1. The electrochemical potential of species is defined in the reference of standard state (Θ) with unit activity

$$\bar{\mu}_i = RTlna_i + \mu_i^{\Theta} + nF\varphi = RTln\tilde{c_i} + \bar{\mu}_i^{ex} \tag{4-1}$$

where R, T and F are gas constant, temperature and Faraday constant, respectively. n is the valence of metal cation, and φ is the local electrostatic potential. a_i is the activity of species and $\tilde{c_i} = c_i/c_0$ is the dimensionless concentration, where c_0 is the standard bulk concentration of electrolyte solution. $\bar{\mu}_i^{ex}$ is the excess electrochemical potential. The electrochemical potential of each component involved in the electrodeposition reaction can be then written as

$$\bar{\mu}_{M^{n+}} = RTlna_{M^{n+}} + \mu_{M^{n+}}^{\Theta} + nF\varphi_s = RTlnc_{M^{n+}} + \bar{\mu}_{M^{n+}}^{ex} \tag{4-2}$$

$$\bar{\mu}_e = RTlna_e + \mu_e^{\Theta} - F\varphi_e = RTlnc_e + \bar{\mu}_e^{ex} \tag{4-3}$$

$$\bar{\mu}_M = RTlna_M + \mu_M^{\Theta} = RTlnc_M + \bar{\mu}_M^{ex} \tag{4-4}$$

where φ_s and φ_e are the local electrostatic potential in the electrolyte solution and at the metal electrode. The interfacial potential difference at electrode/electrolyte interface is thus $\Delta\varphi = \varphi_e - \varphi_s$. Then the total electrochemical potential of reactants and products are expressed as $\bar{\mu}_1 = \bar{\mu}_{M^{n+}} + n\bar{\mu}_e$, and $\bar{\mu}_2 = \bar{\mu}_M$, respectively. At electrochemical equilibrium, the reaction electrochemical potential is 0 ($\Delta\mu = \bar{\mu}_1 - \bar{\mu}_2 = 0$), which gives the Nernst equation, or the equilibrium voltage

$$\Delta\varphi^{eq} = E^{\Theta} + \frac{RT}{nF} ln \frac{a_{M^{n+}} {a_{a_e}}^n}{a_M} \tag{4-5}$$

where $E^{\Theta} = \frac{\mu^{\Theta}_{M^{n+}} + n\mu^{\Theta}_{e} - \mu^{\Theta}_{M}}{nF}$ is the standard half-cell potential, which is taken as the voltage reference.

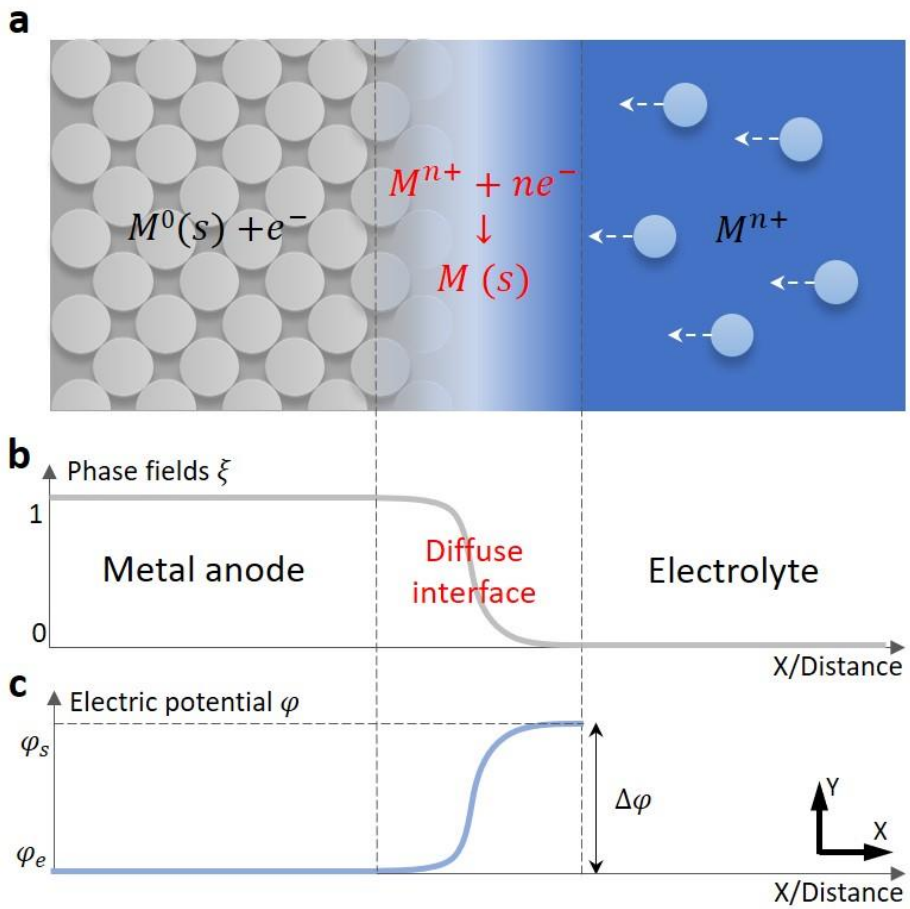

Figure 4-1. The schematic of phase-field model for metal electrodeposition: (a) the half-cell simulation system of metal anode and liquid electrolyte; (b) phase-field order parameter variation at the anode/electrolyte interface; (c) the electric potential variation at the anode/electrolyte interface.

4.2.2 Reaction kinetics

We apply the general transition state theory to the Faradaic charge-transfer process to study the reaction kinetics during metal electrodeposition. From the excess electrochemical potential landscape in reaction coordinates, equilibrium reactants at each energy minima ($\bar{\mu}_1^{ex}$ and

$\bar{\mu}_2^{ex}$) are separated by an energy barrier ($\bar{\mu}_{TS}^{ex}$) of the transition state. Upon excitation, the reaction complex occasionally overcomes the energy barrier and crosses the short-lived transition state (Figure 4-2). For a simple faradaic reaction (e.g. $M^{n+} + ne^- \rightarrow M(s)$), the reaction rate is defined as the difference between the forward ($R_{1\rightarrow2}$) and backward ($R_{2\rightarrow1}$) reaction rates

$$\bar{R} = R_{1\rightarrow2} - R_{2\rightarrow1} = k_{1\rightarrow2}^0 \exp\left(-\frac{\bar{\mu}_{TS}^{ex} - \bar{\mu}_1}{RT}\right) - k_{2\rightarrow1}^0 \exp\left(-\frac{\bar{\mu}_{TS}^{ex} - \bar{\mu}_2}{RT}\right) \qquad (4\text{-}6)$$

where $k_{1\rightarrow2}^0$ and $k_{2\rightarrow1}^0$ are the forward and backward reaction rate constants, respectively, which depend on temperature only. The transition is considered "rare event" since the energy barrier height is usually much larger than thermal energy ($(\bar{\mu}_{TS}^{ex} - \bar{\mu}_i^{ex})/N_A \gg k_B T$, where N_A is Avogadro's Constant and k_B is Boltzmann constant.). It is also assumed that reaction particles reaching the transition state proceed with unit probability, and that any concentration effects at this short-lived state, i.e. $k_B T ln c_{TS}$, can be factored out into the pre-factor rate constant k_0. Therefore, it is convenient to define the reaction rate in terms of the excess electrochemical potential at transition state, $\bar{\mu}_{TS}^{ex}$, instead of $\bar{\mu}_{TS}$ in equation (4-6).

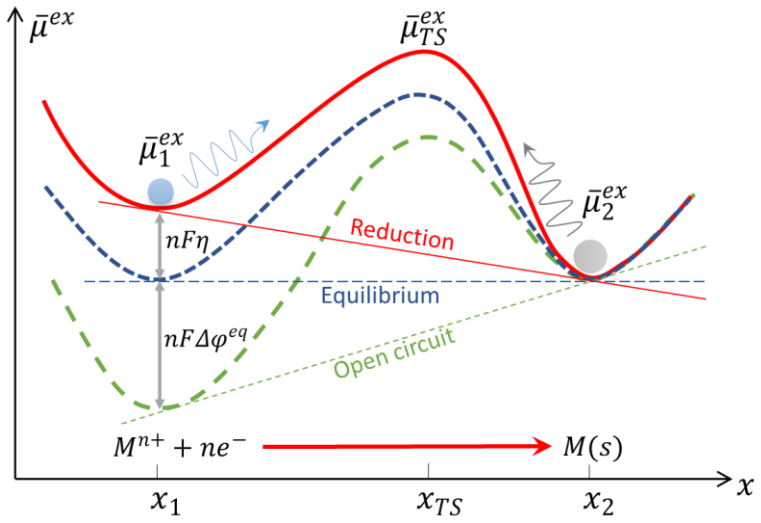

Figure 4-2. Schematic of excess chemical potential landscape in reaction coordinate, demonstrating the transition state (x_{TS}) and the equilibria (x_1 and x_2) for a metal electrodeposition reaction ($M^{n+} + ne^- \rightarrow M(s)$) at open circuit (green), Nernst equilibrium (blue) and during reduction [178] under a negative overpotential ($\eta < 0$), respectively.

At electrochemical equilibrium ($\Delta\mu = \bar{\mu}_1 - \bar{\mu}_2 = 0$, or $\Delta\varphi = \Delta\varphi^{eq}$), the reaction rate $\bar{R} = R_{1\to2} - R_{2\to1} = 0$. So, we have $k^0_{1\to2} = k^0_{2\to1} = k_0$, with a properly defined electrochemical potential. The reaction rate can be rewritten as

$$\bar{R} = k_0\left[{c_{M^{n+}}c_e}^n \exp\left(-\frac{\bar{\mu}^{ex}_{TS}-\bar{\mu}^{ex}_1}{RT}\right) - c_M \exp\left(-\frac{\bar{\mu}^{ex}_{TS}-\bar{\mu}^{ex}_2}{RT}\right)\right] \quad (4\text{-}7)$$

Now the reaction kinetics can be correlated to equilibrium thermodynamics by the De Donder relation

$$\frac{R_{1\to2}}{R_{2\to1}} = \exp\left(-\frac{\bar{\mu}_2-\bar{\mu}_1}{RT}\right) = \exp\left(-\frac{\Delta\mu}{RT}\right) \quad (4\text{-}8)$$

Out of equilibrium, the reaction rate is controlled by overpotential (η), which is more commonly used in electrochemistry.

$$\eta = \Delta\varphi - \Delta\varphi^{eq} \quad (4\text{-}9)$$

The Butler-Volmer hypothesis asserts that the electrostatic energy of the transition state is a weight average of the electrostatic energy of the oxidized state and the reduced state. The excess electrochemical potential of transition state is defined as

$$\bar{\mu}^{ex}_{TS} = \bar{\mu}^{A}_{TS} + (1-\alpha)\left(\mu^{\ominus}_{M^{n+}} + n\mu^{\ominus}_e + nF\varphi_s - nF\varphi_e\right) + \alpha\mu^{\ominus}_M \quad (4\text{-}10)$$

where $\bar{\mu}^{A}_{TS} = RTln\gamma_{TS}$ is the activation chemical potential, denoting the contribution from excess chemical activity at transition state (e.g. energy penalty due to adsorption, solvation, etc.). γ_{TS} is the activity coefficient at transition state. α is the symmetric factor that is normally considered to be 1/2 at moderate overpotential and nondepleted concentration [121]. By substituting into equation (4-7), we have the reaction rate in terms of overpotential

$$\bar{R} = \frac{k_0}{\gamma_{TS}}\left({a_{M^{n+}}a_e}^n\right)^{(1-\alpha)}{a_M}^{\alpha}\left[\exp\left(\frac{-\alpha nF\eta}{RT}\right) - \exp\left(\frac{(1-\alpha)nF\eta}{RT}\right)\right] \quad (4\text{-}11)$$

The reaction current can also be formulated based on reaction rate by correlation, $I = nFA\bar{R}$.

$$I = I_0\left[\exp\left(\frac{-\alpha nF\eta}{RT}\right) - \exp\left(\frac{(1-\alpha)nF\eta}{RT}\right)\right] \quad (4\text{-}12)$$

$$I_0 = \frac{nFAk_0}{\gamma_{TS}} (a_{M^{n+}} a_e{}^n)^{(1-\alpha)} a_M{}^{\alpha} \quad (4\text{-}13)$$

where A denotes the dimensionless area or number of reaction sites. I_0 is the exchange current of electrodeposition reaction. Therefore, even there is no net current at the electrochemical equilibrium ($I = 0$), the exchange current is nonzero ($I_0 \neq 0$).

4.2.3 The transition state of charge-transfer

Compared to the well-defined equilibrium states where the reaction complex resides most of the time, the transition state is such a short-lived state that further elaboration is often circumvented. Formulation-wise, the transition state influences the reaction kinetics in terms of activity coefficient (γ_{TS}) in the reaction rate pre-factor (for general chemical reactions) or exchange current (for Faradaic reactions). Most works on Faradaic reactions treated γ_{TS} as a constant for simplicity and due to the lack of exchange current databases in various non-standard scenarios, which is considered reasonable for studies on a specific material or when the solvent reorganization effects are negligible. For a general model of Faradaic reactions in concentrated solutions, however, a more concrete description of the transition state is desired so that γ_{TS} can be properly defined. We hereby propose a method to correlate the reaction exchange current to a more well-defined transition state. During a charge-transfer in an electrodeposition reaction, the solvated metal cations adsorb onto the electrode surface, de-solvate and then react with the active electrode material and electrons. As a first approximation, the adsorption step can be described by a lattice gas model [121], as shown in Figure 4-3 using metal M deposition as an example. The activation chemical potential ($\bar{\mu}_{TS}^{A}$) at transition state can be written as

$$\bar{\mu}_{TS}^{A} = RTln\gamma_{TS} = -N_{sol}RTln(1-\theta) + u(1-2\theta) + \Delta E_{ads} + \Delta E_{sol} \quad (4\text{-}14)$$

where $N_{sol}(\geq 1)$ is the number of available reaction sites that the solvation shell excludes on the electrode surface, which is related to the shell size and electrode surface structure. θ is the mean coverage fraction of adsorbed solvated-cations onto the electrode surface. The term $u(1-2\theta)$ denotes the short-range interaction between adsorbed species ("Frumkin isotherm" for $h_{iso} \neq 0$ and "Langmuir isotherm" for $u = 0$.). ΔE_{ads} and ΔE_{sol} are adsorption energy and solvation energy, respectively. Here we consider a Langmuir isotherm with $u = 0$. Therefore, the activity coefficient at transition state is

$$\gamma_{TS} = \frac{1}{(1-\theta)^{N_{sol}}} \exp\left(\frac{\Delta E_{ads}+\Delta E_{sol}}{RT}\right) \tag{4-15}$$

It is convenient to combine ΔE_{ads} and ΔE_{sol} into one de-solvation energy term, i.e. $\Delta E_{de-sol} = \Delta E_{ads} + \Delta E_{sol}$. Then the exchange current density can be reformulated as

$$i_0 = \frac{I_0}{A} = \left[(1-\theta)^{N_{sol}} \exp\left(-\frac{\Delta E_{de-sol}}{RT}\right)\right] nFk_0 (a_{M^{n+}} a_e{}^n)^{(1-\alpha)} a_M{}^{\alpha} \tag{4-16}$$

Therefore, with the mean coverage $0 < \theta < 1$, a larger N_{sol} value (larger solvation shell size) leads to a lower exchange current. Meanwhile, an increased de-solvation energy barrier results in a decreased exchange current. By now, we managed to specify the charge-transfer kinetics through a properly-defined transition state, and make further connection to the mesoscale phase-field model.

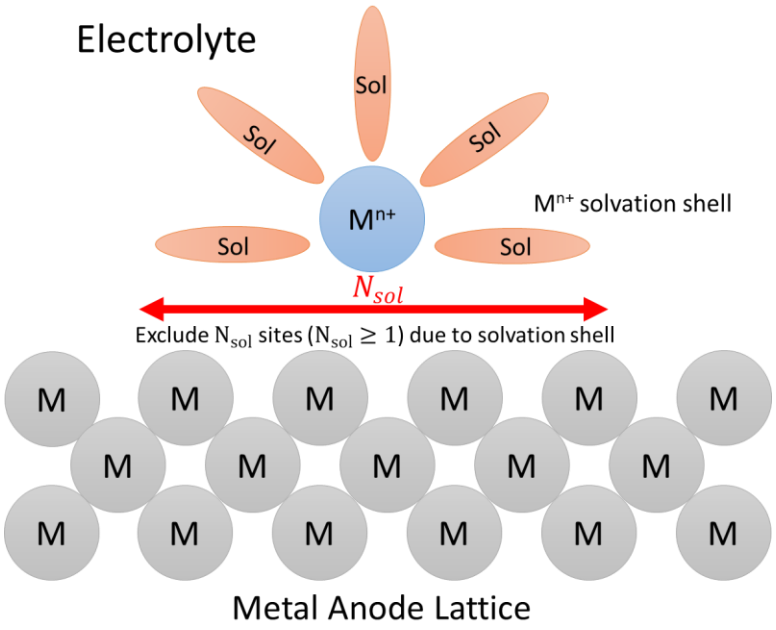

Figure 4-3. The schematic of solvated M^{n+} cation adsorbed onto the M metal surface in liquid electrolyte solution during a general metal electrodeposition process, and the definition of the solvation shell size parameter N_{sol}.

4.2.4 The phase-field model and simulation setup

Assuming negligible mechanical impact on the electrodeposition process in a liquid electrolyte, the total Gibbs free energy of the system can thus be written as

$$G = \int_V [f_{local}(\xi, \tilde{c}_i) + f_{grad}(\nabla\xi) + f_{elec}(c_i, \varphi)]\, dV \tag{4-17}$$

where ξ is a dimensionless phase-field order parameter representing phase fraction, varying continuously from 1 to 0 to distinguish the solid phase (i.e. the metal electrode at $\xi = 1$) and the liquid phase (i.e. the electrolyte at $\xi = 0$) with a diffuse interface of finite width, as shown in Figure 4-1 (b). The local free energy density for the bulk is given by

$$f_{local} = g(\xi) + c_0 RT \sum_i \tilde{c}_i \, ln\tilde{c}_i + \sum_i c_i \mu_i^{\theta} \tag{4-18}$$

where i indicates all the involving species, i.e. $i = M^{n+}$, e and M. $\tilde{c}_i = c_i/c_0$ is the dimensionless concentration. c_0 is the standard bulk concentration of electrolyte solution. μ_i^{θ} is the standard

chemical potential of species i. A double-well form function, $g(\xi) = W\xi^2(1-\xi)^2$, is used to mathematically describe the non-electrochemical energetic landscape of the two equilibrium states with a transition energy barrier of $W/16$. $f_{elec} = F\sum_i n_i c_i \varphi$ is the electrostatic energy density, where the local electrostatic potential φ in the electrolyte solution and the metal electrode are φ_s and φ_e (Figure. 4-1 (c)), respectively. $f_{grad} = 1/2\kappa(\nabla\xi)^2$ is the gradient energy density, accounting for the half of the surface energy contribution for an interface at equilibrium, where $\kappa(\psi) = \kappa_0[1+\delta cos(\omega\psi)]^2$ is the gradient coefficient.

Assuming electrons always supply (unit electron activity) at the metal anode, the phase temporal evolution is governed by

$$\frac{\partial\xi}{\partial t} = -L_\sigma[g'(\xi) - \kappa\nabla^2\xi] - L_\eta h'(\xi)\left\{exp\left[\frac{(1-\alpha)nF\eta}{RT}\right] - \tilde{c}_+ exp\left[\frac{-\alpha nF\eta}{RT}\right]\right\} \quad (4\text{-}19)$$

where L_σ is the interface mobility and L_η is a pre-factor related to reaction exchange current, i.e. $L_\eta = \frac{I_0}{nFA}$. An interpolating function, $h(\xi) = \xi^3(6\xi^2 - 15\xi + 10)$, is applied to confine the electrochemical driving force within the electrode/electrolyte interface region, where the charge-transfer takes place.

The mass transport in the electrodeposition system is described by the Nernst-Planck equation. We assume the metal atoms are motionless since the self-diffusion in the solid metal electrode is orders of magnitude slower than the species diffusion in a liquid electrolyte. It is also reasonable to consider that the effects of anions and solvent molecules on the diffusion of metal ions are effectively included in the diffusion coefficients of the metal ions. Therefore, the mass transport during electrodeposition is solely determined by metal cation diffusion

$$\frac{\partial\tilde{c}_+}{\partial t} = \nabla\cdot\left[D\nabla\tilde{c}_+ + \frac{D\tilde{c}_+}{RT}nF\nabla\varphi\right] - \frac{c_s}{c_0}\frac{\partial\xi}{\partial t} \quad (4\text{-}20)$$

where the effective diffusion coefficient D is material dependent, interpolated as $D = D_e h(\xi) + D_s[1-h(\xi)]$. D_e and D_s are the metal cation diffusion coefficients in solid metal electrode and electrolyte, respectively, where $D_e \cong 0$. The last term is the metal cation consumption/production

at the electrode/electrolyte interface due to the charge-transfer reaction, where c_s is the site density of Li metal.

The electrostatic potential field of the system is described by Poisson-type equation including a source term accounting for the charge annihilated (or created) due to the electrodeposition reaction.

$$\nabla \cdot \left[\sigma \cdot \nabla\left(\varphi(\boldsymbol{r}, t)\right)\right] = I_R \tag{4-21}$$

where σ is the effective conductivity expressed by interpolating function as $\sigma = \sigma_e h(\xi) + \sigma_s[1 - h(\xi)]$, in which σ_e and σ_s are the conductivities of solid metal electrode and electrolyte, respectively. The source term I_R is also related to reaction rate at the electrode/electrolyte interface, taking the form of $I_R = nFc_s \frac{\partial \xi}{\partial t}$. Since only the cation diffusion is considered in the system, a modified description of the electrostatic potential distribution is used by assuming charge neutrality in the system, which is detailed in our previous work [120].

All the equations in this work were solved using COMSOL Multiphysics 5.2 based on the finite element method. The $500 \times 500 \mu m$ system is adaptively meshed by a 140×140 grid with a minimum spacing of $1 \mu m$. An implicit time integration was used with a timestep of $0.2\ s$. A Dirichlet boundary condition of the electrolyte bulk concentration ($c_0 = 1 mol/L$) was applied on the boundary opposite to the anode side. The constant voltage condition of $0.1\ V$ was used for all electrodeposition processes. The normalization details and a complete parameter table can be found in Table 4-1. Three half-spherical nuclei with a radius of 5 μm were included as the initial morphology in each simulation. No random noise was included for all simulations.

Table 4-1. Phase-field simulation in liquid electrolyte: parameters and their normalizations.

	Symbol	Unit	Real Value		Normalization	Normalized Value	
			Li	Mg		Li	Mg
System Size	l	m	5.0×10^{-4}		$\tilde{l} = l/l_0$	5.0	
Time Step	Δt	s	0.2		$\Delta\tilde{t} = \Delta t/\Delta t_0$	5.0×10^{-5}	
Cation Diffusion Coeff. in Electrolyte	D_s	m^2/s	7.5×10^{-10}		$\widetilde{D}_s = D_s/({l_0}^2/\Delta t_0)$	300	
Cation Diffusion Coeff. in Anode	D_e	m^2/s	7.5×10^{-14}		$\widetilde{D}_e = D_e/({l_0}^2/\Delta t_0)$	0.03	
Cation Bulk Concentration in Electrolyte	c_0	mol/m^3	1.0×10^3		$\tilde{c}_0 = c_0/c_0$	1.0	
Conductivity in Electrolyte	σ_s	S/m	1.0		$\tilde{\sigma}_s = \sigma_s \cdot (\Delta t_0 RT)/(c_0 F^2 {l_0}^2)$	1.0×10^2	
Conductivity in Anode	σ_e	S/m	1.0×10^7		$\tilde{\sigma}_e = \sigma_e \cdot (\Delta t_0 RT)/(c_0 F^2 {l_0}^2)$	1.0×10^9	
Interface Mobility	L_σ	$m^3/(J \cdot s)$	2.5×10^{-6}		$\tilde{L}_\sigma = L_\sigma \cdot (E_0 \cdot \Delta t_0)$	1.5×10^5	
Standard Rate Constant	k_0	m/s	0.1		$\tilde{k}_0 = k_0 \cdot (\Delta t_0/l_0)$	4.0×10^7	
Electrodeposition Rate Normalizer	λ_η	$/m$	1.0×10^8		$\tilde{\lambda}_\eta = \lambda_\eta \cdot l_0$	1.0×10^4	
Symmetric factor	α	–	0.5		–	–	
Site Density of Metal	c_s	mol/m^3	7.64×10^4	7.15×10^4	$\tilde{c}_s = c_s/c_0$	76.4	71.5
Exchange Current Density	i_0	A/m^2	0.376	0.031	$i_0/{i_0}^{Li}$	1.0	0.083
Electrochemical Pre-factor	L_η	$/s$	5.1×10^{-3}	2.3×10^{-4}	$\tilde{L}_\eta = L_\eta \cdot \Delta t_0$	20	1.0
Barrier Height	W	J/m^3	1.18×10^6	1.58×10^6	$\widetilde{W} = W/E_0$	0.08	0.11
Gradient Energy Coeff.	κ_0	J/m	3.68×10^{-6}	4.95×10^{-6}	$\widetilde{\kappa}_0 = \kappa_0/(E_0 \cdot {l_0}^2)$	2.45×10^{-5}	3.30×10^{-5}
Anisotropy	δ	–	0.04	0.09	–	–	–
Crystallographic Symmetry Mode	ϖ	–	4	6	–	–	–
Cation Valence	n	–	1	2	–	–	–

4.3 Results and discussion

As an application and validation of model, we apply the as-formulated electrodeposition phase-field model to Li and Mg metal electrodeposition morphological analyses. With the input parameters from the DFT-based atomic calculations on Li and Mg half-cell systems [165], we demonstrate that our phase-field model reproduced the dendritic growth of Li and faceted morphology evolution of Mg, as observed in scanning electron microscope (SEM) images [184]. Then we performed a systematic parametric study on the plating morphological evolution with respect to the key properties related to the electrodeposition kinetics.

4.3.1 Incorporate atomic calculation on charge-transfer

A key advance of this work is the development of a computational framework for directly linking the phase-field model of the electrodeposition process and the atomistic simulations discussed above. It allows us to directly incorporate the charge-transfer kinetic parameters as well as the surface energy anisotropy from DFT calculations into the phase-field modeling of electrodeposition process.

In this work, we fit the surface energies from DFT calculations [82, 185] into the gradient coefficient $\kappa(\psi) = \kappa_0[1 + \delta cos(\omega\psi)]^2$ with the parameter values listed in Table 4-1, where κ_0 is associated with the average surface energy and interface width, δ and ω are the anisotropy strength and crystallographic symmetry mode, respectively. ψ is the angle between the reference axis and the migration normal vector of interface. The hexagonal close-packed (hcp) Mg metal has a 6-fold symmetry ($\omega_{Mg} = 6$) while the body-centered cubic (bcc) Li metal has a 4-fold symmetry ($\omega_{Li} = 4$) in their corresponding basal planes, i.e. (0001) plane for Mg and (001) plane for Li, respectively. The present phase-field model integrates the effects of surface SEI layer implicitly by introducing an effective parameter for the charge-transfer kinetics into the exchange current terms. Given unit electron activity and the same electrolyte bulk concentration, the electrodeposition exchange currents density of Li and Mg are further written as

$$i_0^{Li} = B_0^{Li}(1-\theta)^{N_{sol}^{Li}} \exp\left(-\frac{\Delta E_{de-sol}^{Li}}{RT}\right) \tag{4-22}$$

$$i_0^{Mg} = 2B_0^{Mg}(1-\theta)^{N_{sol}^{Mg}} \exp\left(-\frac{\Delta E_{de-sol}^{Mg}}{RT}\right) \tag{4-23}$$

where the pre-factor $B_0 = Fk_0c_0$ is considered as a constant for both cases. The standard rate constant k_0 with units of $cm \cdot s^{-1}$ is assumed comparable for Li and Mg plating reaction. Therefore, the exchange current is basically determined by the de-solvation energy barrier (ΔE_{de-sol}) during charge-transfer, the solvation shell size parameter (N_{sol}), and the mean

coverage (θ). The de-solvation energies were estimated to be $\Delta E_{de-sol}^{Li} \cong 0.41$ eV and $\Delta E_{de-sol}^{Mg} \cong 0.49$ eV from the calculated charge-transfer energy landscapes for Li and Mg electrodeposition reaction, respectively. The solvation shell size parameters were approximated to be $N_{sol}^{Li} \cong 4.29$, $N_{sol}^{Mg} \cong 3.2$, based on their relaxed atomic cells of charge-transfer, respectively. The mean coverage parameter can be calculated by $\theta(Mg) = 1/N_{sol}^{Mg} = 0.31$ and $\theta(Li) = 1/N_{sol}^{Mg} = 0.23$, respectively. Substituting ΔE_{de-sol} and N_{sol} into equation (4-22) and (4-23), the electrodeposition exchange current, i_0, of Li (0.376 A m^{-2}) was calculated to be about ten times larger than Mg (0.031 A m^{-2}), as shown in Table 4-1. At atomic scale, the Li metal anode is SEI-covered, while a functional Mg anode surface is normally assumed free of passivation layer [176]. However, to be consistent in the phase-field formulation as well as to avoid further complication due to the surface voltage variation incorporating the SEI layer [165], the phase-field model will not explicitly model the SEI. For future work, the impact of surface passivation layer [1] or artificial coating on charge-transfer rate parameter can be incorporated with an additional effective kinetics parameter, Ω, such that $B_0 = \Omega F k_0 c_0$.

4.3.2 Phase-field simulation of Li and Mg electrodeposition

The electrodepositions of Li and Mg in $500 \times 500 \mu m$ half cells were reproduced by phase-field simulations with identical electrochemical boundary conditions (constant applied electric voltage of $0.1\,V$). In the simulation of Mg plating, we placed its basal plane (0001) parallel to the XY plane to expose the $(10\bar{1}0)$ and $(11\bar{2}0)$ planes that have higher surface energies and less anisotropy to the electrolyte environment. This guarantees the two planes where dendrite growth is more energetically favorable are examined. Likewise, we placed the Li basal plane (001) parallel to XY plane for Li plating simulation. We assumed the cation diffusion coefficients

of Mg and Li in the electrolyte are the same. The slowdown of cation diffusion at Li metal surface due to the presence of a SEI layer was not explicitly included in the present work but can be incorporated in an effective diffusion coefficient. The spatial and temporal evolution of the morphology, ion concentration, ion flux, local electric potential, and electric field were obtained by solving the phase-field equations numerically. The anode surface initial roughness was mimicked by adding three $5\,\mu m$ half-spheres of single crystalline metal nuclei, as shown in Figure 3 (o).

The simulated Li and Mg plating morphological evolutions are illustrated at selected timesteps in Figure 3 (a) to 3 (d), and 3 (f) to 3 (i), respectively. In contrast to the mossy and dendritic pattern of Li (Figure 3 (d)), half-hexagonal morphology (Figure 3 (i)) was harvested for Mg, corresponding to its hcp crystallography. Although the initial nuclei shapes were half-spherical (Figure 3 (o)), they started to become faceted for Mg (Figure 3 (g)) and branchy for Li (Figure 3 (b)) within 200s. These simulated morphologies of deposited Li and Mg by the phase-field method were consistent with the experimental images captured by SEM [184] in Figure 3 (e) and 3 (j), respectively. To be comparable with the constant current electrodeposition condition of 2 mA cm^{-2} applied in experiment [184], we also determined that the simulated average current density under the constant voltage condition is in the range of $2 \sim 4$ mA cm^{-2}, with an average of 2.77 mA cm^{-2} for Li and 2.58 mA cm^{-2} for Mg, respectively. It is noted that the amount of deposited Mg metal was less than Li metal under similar current densities, indicating the higher volumetric capacity of Mg metal anode (3833 mAh cm^{-3} for Mg vs. 2046 mAh cm^{-3} for Li) [175].

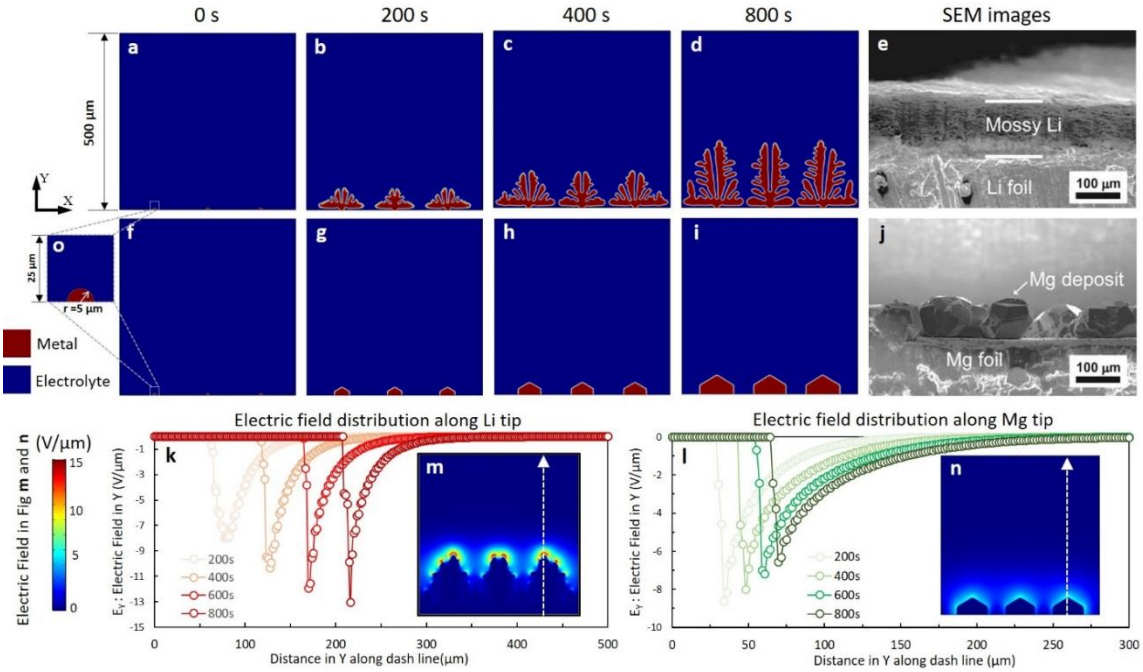

Figure 4-4. Reproducing Li and Mg electrodeposition by phase-field model: The 2D phase-field simulation morphologies at 0s, 200s, 400s, and 800s from (a-d) Li and (f-i) Mg electrodeposition, respectively, compared with the SEM captured (e) Li and (j) Mg electrodeposit morphologies from a hybrid Mg-Li-ion battery. The 2D electric field strength distribution at 800s during (m) Li and (n) Mg electrodeposition, and the 1D variation of the electric field in Y along with tip directions (white dash lines) at selected time steps during (k) Li and (l) Mg electrodeposition. The SEM images were adapted with permission from Reference [184]. Copyright (2015) American Chemical Society.

The ionic transport and charge-transfer behaviors in liquid electrolyte during Li and Mg plating can be visualized and compared from their cation concentration and concentration gradient profiles generated by phase-field simulations as shown in Figure 4-5. The morphologies of deposited metals are indicated within the 0 M-concentration blue regions in Figure 4-5 (a) and (b). The elevated cation flux region at Li metal surfaces in red in Figure 4-5 (c) corresponds to locally faster cation consumption or higher electrodeposition rate, where the dendritic growth originates. By contrast, the concentration flux inhomogeneity is not observed at Mg metal surfaces in Figure 4-5 (d), which is closely associated with its non-dendritic plating morphology. The 1-dimensional cation concentration and flux variations along tips in Figure 4-5 (e) further

reveal that the tip region cation flux increases over time during Li plating. Oppositely, a decreased trend of tip region cation flux during Mg plating is observed in Figure 4-5 (h), indicating the tip concentration flux localization can be automatically mitigated at Mg metal surface.

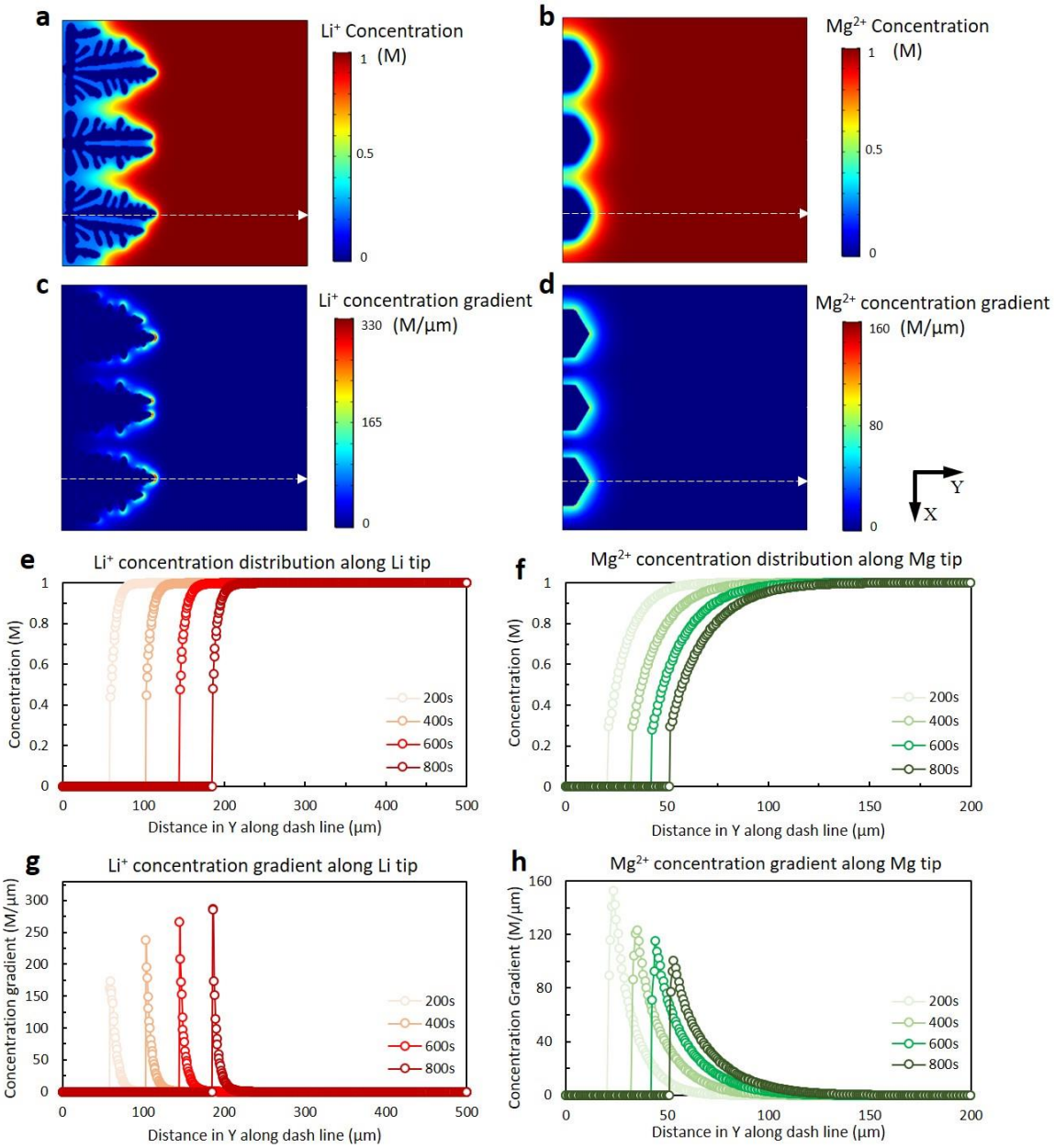

Figure 4-5. The cation concentration distributions of (a) Li and (b) Mg plating, and the corresponding cation concentration gradient magnitude distributions of (c) Li and (d) Mg plating at 800s. The 1-dimensional variation of cation concentration along tip directions indicated by dash lines during (e) Li and (f) Mg electrodeposition, and the corresponding concentration gradient magnitude variation along tip directions during Li (g) and Mg (h) electrodeposition at 200s, 400s, 600s and 800s.

From the electric potential profiles of Li and Mg plating at 800s shown in Figure 4-6 (a) and (b), the potential drops at anode surface region due to charge-transfer reaction, creating an elevated electric field at anode/electrolyte interfacial region in red (Figure 4-6 (c) and (d)). Similarly, opposite trends of tip region electric field variation are observed in 1-dimensional along tip direction during Li and Mg plating, which increases over time for Li (Figure 4-6 (g)) but decreases over time for Mg (Figure 4-6 (h)).

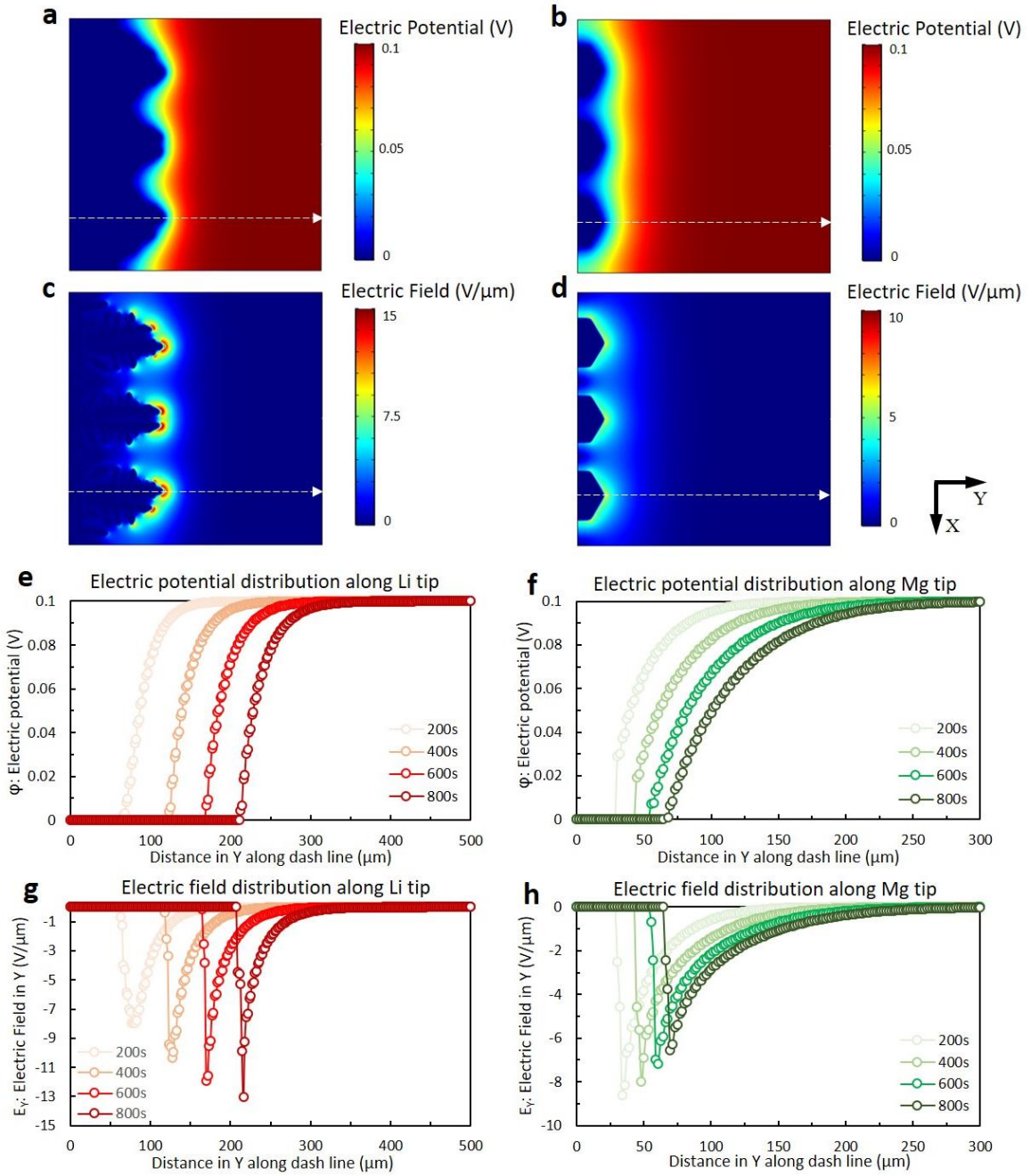

Figure 4-6. The electric potential profiles of (**a**) Li and (**b**) Mg plating, and the corresponding electric field strength distributions of (**c**) Li and (**d**) Mg plating at 800s. The 1-dimensional variation of electric potential along tip directions indicated by dash lines during (**e**) Li and (**f**) Mg electrodeposition, and the corresponding variation of electric field in Y along tip directions during Li (**g**) and Mg (**h**) electrodeposition at 200s, 400s, 600s and 800s.

The morphological difference between Li and Mg is directly associated with their temporal electrochemical driving forces (equation (4-21) in 4.2.4 section), which are further related to their local ion concentration and electrostatic distributions. As mentioned above, the ion concentration gradient and the electric field near the growing tip regions exhibited opposite temporal evolution trends between Li and Mg electrodeposition. The metal cation concentration gradient variation along the tip directions (Figure 4-5 (g) and (h)) near the tip region increased over time for Li while decreased over time for Mg. Likewise, the electric field variation along tip directions (Fig 4-4 (k) and (l)) showed the electric field strength in the tip region increased over time for Li but decreased over time for Mg. These two pieces of evidence together proved the formation of mossy Li structure was a self-accelerating process [186], while Mg deposition tends to self-mitigate. More importantly, our simulations naturally revealed the classical model of "Sand's time": when an excess of charge accumulates at the anode and creates a large electric field, the dendritic growth initiates [187, 188].

It has been suggested that the smooth morphology of Mg deposition is attributed to its lower metal surface migration energy barrier in a vacuum than metallic Li [181, 182, 189]. In the liquid electrolyte environment, however, this non-electrochemical process becomes less significant or even irrelevant due to the fast diffusion in the liquid phase and continuous stripping/redeposition at the surface. In this model, we thus focused on the electrochemical reaction kinetics and had assumed that the atomic migration on the metal surface was much slower than the diffusion of the ions in the liquid electrolyte. (Surface migration on an SEI/coating covered anode could be even slower due to the resistance from the interface layer.) Therefore, surface in-plane diffusion can be achieved through cation being stripped into the electrolyte and cation being redeposited at other places. The surface migration in the solid phase will be explicitly incorporated into the phase-field model in the future study.

4.3.3 Implications for Creating Smooth and Dendrite Free Li

Inspired by the smooth morphology of Mg electrodeposition, we attempt to understand the key parameters that lead to the morphological differences between Mg and Li plating. In particular, a morphological evolution map (Fig 4) was generated by controlling the most relevant parameters in the phase-field simulations, namely, the surface energy, anisotropy, and the exchange current. To demonstrate a transition between dendritic pattern and the as-observed dendrite-free morphology in Mg plating, we kept the 6-fold symmetry of Mg and the rest parameters from Li plating, and tuned each investigated property in a physical range covering most metal electrodeposition scenarios [190, 191]. By increasing the surface energy from 0.375 to 1 J m^{-2}, the secondary dendrite arms gradually vanish and the plating morphology becomes less mossy as shown in Fig 4a to 4e. This is because the energy penalty for creating new surfaces increases and thus the secondary arms are eliminated to reduce the total energy. However, the remaining primary arms are still detrimental to battery safety due to the probability of separator penetration. By varying the anisotropy from 0 to 0.15, the splitting in dendrite primary arms disappears while the tip growth rate increases slightly (Fig 4k to 4o). More significantly, by decreasing the exchange current density from 2 times to 0.2 times of Li plating, the deposit morphology transforms notably from mossy dendrite ($2i_0^{Li}$) (Fig 4j) to hexagonal faceted ($0.2i_0^{Li}$) (Fig 4g). Moreover, when the exchange current is further decreased to $0.02i_0^{Li}$, the plating morphology start to become spherical (Fig 4f). This morphological variation demonstrates that the exchange current difference in Mg and Li is the main reason for the faceted morphology of Mg deposit. Although the higher Mg metal surface energy, originated from the stronger Mg-Mg bond strength at the atomic level, also contributes to the minimization of the total surface area, the lower exchange current of Mg plating is majorly responsible for the non-dendritic Mg deposit morphology. However, this does not mean Mg will never form dendrite during electrodeposition.

Under specific experimental conditions (e.g. higher current density, larger over potential, different electrolyte, poor initial surface condition, etc.), dendrite growth with Mg anodes is possible [192]. Our model suggests that, under similar plating current and over potential, the most effective approach to achieve dendrite free electrodeposition is lowering the intrinsic exchange current of electrodeposition reaction, I_0.

4.4 Conclusion

In this chapter, we present a newly developed multiscale model integrating atomic calculations of the charge-transfer reaction parameters and phase field model of electrodepositing morphology evolution to understand and predict the dendrite growth in liquid electrolytes. The scale bridging between the phase-field method and atomistic calculations can be generalized into other chemical and electrochemical processes and achieve a parameter-free predictive modeling approach. The model reproduced dendrite growth of Li plating and the polyhedral morphology of Mg plating. The Li and Mg electrodeposition processes were compared and analyzed from cation diffusion and electrostatic potential distribution evolution. It was discovered that the cation desolvation induced low intrinsic exchange current is mainly responsible for the smooth Mg plating morphology although the surface energy and its anisotropy can also modulate the plating morphology. More importantly, this study suggests electrolyte engineering to increase the desolvation barrier or increase the cation-solvation surface coverage can effectively promote dendrite free electrodeposition at Li metal anodes.

Chapter 5

Phase-field modeling for solid electrolyte design

5.1 Introduction

Solid electrolytes (SEs) and all-solid-state batteries have been regarded as a promising solution to the application of Li metal anode for future high-energy-density batteries. Because most of the solid electrolyte materials are non-flammable, and the parasitic dendrites grown from Li metal anode are believed to be mechanically suppressed by the high-modulus electrolyte phase. However, dendrite penetration, intergranular growth and even isolated nucleation were soon observed in a wide range of solid electrolyte systems, particular inorganic ceramic electrolytes, leading to battery degradation and the risk of short-circuit. With even lower Li conductivities than liquid electrolyte systems, all-solid-state batteries are now confronted with more serious challenges than ever. Many experimental efforts have been attempted to prevent the Li dendrite growth and penetration in SEs, such as increasing the effective shear modulus of SE materials [115, 193], increasing the SE relative density [194], strengthening the SE grain boundaries with secondary phases [195], decreasing the SE grain size, [196] reducing the interfacial resistance by introducing additional phases at extended defects [197, 198], tailoring the electrolyte/electrode interface by depositing buffer interlayers [199]. Nevertheless, with all the efforts so far, Li dendrite and short-circuit still appeared at current densities higher than 1 mA cm^{-2}. Worse still, it remains puzzling and controversial on the underlying mechanisms of these failures in all-solid-state batteries.

The initial belief that solid electrolyte would suppress dendrite growth can be traced back to the first attempt to model the temporal evolution of a needle-like single dendrite tip in polymer

electrolyte by Monroe and Newman. Their model predicts that Li dendrite growth may be mechanically suppressed when the shear modulus of the electrolyte is over two times higher than that of Li metal (~1.6 GPa) [200]. However, the later observation of dendrite in both rubbery polymer SEs [201-204] and stiff ceramic SEs (e.g. LPS, garnet LLZO and LLZTO) [61, 205, 206] collectively suggest that a criterion using modulus alone is not sufficient to determine whether dendrite can be prevented or not, considering the shear moduli of the existing ceramic SE materials (~60 GPa for garnet) [207] are much higher than Li metal.

Mechanisms proposed to understand the dendrite issue in SEs can be summarized into two categories: (1) Mechanically driven extended defects filling mechanism: Small pores, micro-cracks and loose grain boundaries (GBs) generally exist in solid electrolytes. And the deposited Li metal grows more easily into these mechanically-weak sites. As Li metal continuously fills in the defect regions, it generates a stress concentration, leading to propagation of these surface defects and eventually the formation of main cracks that enables Li dendrite penetration. The recently observed elastoplastic, viscoplastic and creep deformation of Li metal at room temperature may further accelerate the Li deposits filling process, particularly given the external pressure (~80 Psi) upon battery cell assembly to maintain a good contact between electrodes and the electrolyte. (2) Electronically driven Li nucleation and growth mechanism: Higher SE electronic conductivity leads to faster Li dendrite growth. DFT calculations found some SE materials, such as LLZO, has prominently elevated electronic conductivity at surfaces and GBs, providing additional driving force for dendrite penetration, intergranular growth, as well as isolated nucleation. These two mechanisms are highly coupled and synergistic.

With detailed mechanism of dendrite growth and penetration under debate, a fully-developed physics-based model to understand Li plating behavior in SEs has been missing. We hereby developed this multiscale phase-field model of Li dendrite growth in SEs to address the existing capability gap. The multiscale approach bridges mesoscale phase-field model and atomic

scale DFT-based calculations. This comprehensive model is able to capture and understand major failure modes of dendrite penetration, intergranular growth and isolated nucleation in SEs and guide the practical design of all-solid-state batteries.

5.2 Phase-field model of Li plating in solid electrolyte

The phase-field model of Li electrodeposition in solid electrolyte was developed based on the liquid electrolyte model. The major differences for the solid electrolyte model are: (i) The electrolyte is no longer treated as a homogeneous phase as did for the liquid systems, since defects, such as pores, cracks and GBs, present extensively in solid phases. (ii) The mechanical interaction between electrode and electrolyte is included, which has great impact on Li plating behaviors. To incorporate these two features, we developed this general phase-field model of Li electrodeposition in a multi-phase polycrystalline solid electrolyte system as shown in Figure 5-1.

5.2.1 General description of the phase-field model and simulation setup

An all-solid-state half-cell system consists of a Li metal anode and a polycrystalline solid electrolyte, as shown in Figure 5-1. The solid electrolyte always contains internal extended defects voids, pores, cracks, and GBs. To describe the microstructure of an N-grain solid electrolyte cell, we employ N+1 independent non-conserved phase-field variables to define each grain or phase with: $\{\xi, (\phi_1, \phi_2, \dots, \phi_g \dots \phi_N)\} = \{1, (0,0, \dots, 0, \dots 0)\}$ for Li metal, $\{\xi, (\phi_1, \phi_2, \dots, \phi_g \dots \phi_N)\} = \{0, (0,0, \dots, 1, \dots 0)\}$ for the ith grain of the solid electrolyte, and $\{\xi, (\phi_1, \phi_2, \dots, \phi_g \dots \phi_N)\} = \{0, (0,0, \dots, 0, \dots 0)\}$ for unspecified internal extended defects. Each field is continuous across the phase boundary with a finite thickness. Therefore, the total energy of the inhomogeneous system is given by

$$G = \int \left[f_{local}(\xi, \phi_g, \tilde{c}_i) + f_{grad}(\nabla\xi, \nabla\phi_g) + f_{elec}(c_i, \varphi) + f_{mech}(\xi, \phi_g) \right] dV \quad (5\text{-}1)$$

where $\tilde{c}_i = c_i/c_0$ is a set of dimensionless concentrations of species, (i.e. $i = Li^+, e^-$) where c_0 is the bulk concentration of the solid phase. φ is the electrostatic potential. The complete formulation of each energy contribution term in total energy can be found in the section 5.2.2. The evolution equations of Li metal phase and each solid electrolyte grain can be obtained by solving the nonlinear Allen-Cahn equations incorporating Butler-Volmer kinetics [120] and the conventional Allen-Cahn equations [118], respectively, as

$$\frac{\partial\xi}{\partial t} = -L_\sigma^\xi \left(\frac{\partial f_0}{\partial\xi} + \frac{\partial f_{mech}}{\partial\xi} - \kappa_\xi \nabla^2\xi \right) - L_\eta h'(\xi) \left[-\tilde{c}_{Li+}\tilde{c}_e exp\frac{-\alpha F\eta}{RT} + exp\frac{(1-\alpha)F\eta}{RT} \right] + \delta_N \quad (5\text{-}2)$$

$$\frac{\partial\phi_g}{\partial t} = -L_\sigma^\phi \frac{\delta G}{\delta\phi_g} \quad (5\text{-}3)$$

where L_σ^ξ and L_σ^ϕ are the interface mobility of Li metal phase and solid electrolyte phase, respectively, and L_η is associated with the exchange current of electrodeposition. α and η are the charge transfer coefficient and electric overpotential, respectively. Details of the nonlinear phase-field model for electrodeposition can be found in references [119, 120]. The driving force of dendrite nucleation, δ_N, is a Dirac delta function, which is further given by,

$$\delta_N = \begin{cases} 1, & P_N = 1 - \exp(-J^* \cdot \Delta t) > random[0,1] \\ 0, & otherwise \end{cases} \quad (5\text{-}4)$$

where P_N is an approximation of the nucleation probability in the form of a Poisson distribution. J^* is the dendrite nucleation rate derived from classical nucleation theory, taking the form of $J^* = J_0^* exp\left(-\frac{\zeta\Delta G^*}{RT}\right)$, where J_0^* is a nucleation rate pre-factor, ζ is the correction factor for inhomogeneous nucleation. $\Delta G^*$is the classical nucleation activation energy depending on local electric potential, Li ion concentration and electron concentration (The detailed derivation can be found in section 5.2.5). This formulation of explicit nucleation is based on the assumptions that (1) the nucleation time is much less than simulation timestep Δt, (2) the smallest simulation grid volume is taken as the initial nuclei of Li metal, and (3) the expectation number of the formed

nuclei within the time of Δt is $J^* \cdot \Delta t$. The detailed phase-field model of explicit nucleation can be found in reference [208]. The phase evolution equations (5-2) and (5-3) were solved simultaneously with mass transport and electrostatic distribution as detailed in section 5.2.3.

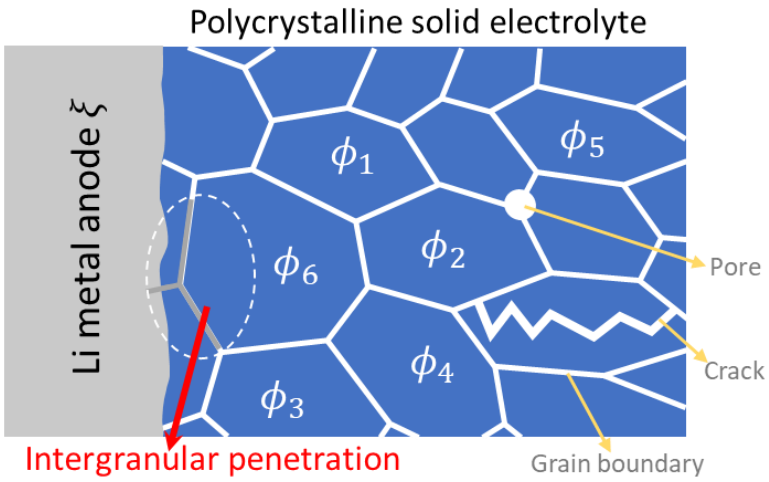

Figure 5-1. The schematic of a multi-phase polycrystalline solid electrolyte Li metal anode half-cell system, and Li dendrite growth along extended defects such as pores, cracks, grain boundaries.

All phase-field simulations were performed by COMSOL Multiphysics 5.2 using finite element solver with implicit time integration (timestep $\Delta t = 0.2s$). The $500\mu m \times 500\mu m$ solid electrolyte cell was adaptively meshed by a 200×200 grid with a minimum grid size of $1\ \mu m$. Dirichlet boundary condition of electrolyte bulk Li ion concentration ($c_0 \approx 42.2\ mol/L$ for LLZO calculated from ideal LLZO supercell.) was employed on the side opposite to anode. A constant electric overpotential of - 0.1 V was applied for all systems to mimic the constant voltage plating condition. The normalization details and a complete parameter table can be found in **Table 5-1**. The initial polycrystalline solid electrolyte structures of different grain sizes were generated from phase-field grain growth code [209, 210].

Table 5-1. Phase-field simulation in solid electrolyte: parameters and their normalizations.

	Symbol	Unit	Real Value		Normalization	Normalized Value	
			Li	LLZO		Li	LLZO
System Size	l	m	5.0×10^{-4}		$\tilde{l} = l/l_0$	5	
Time step	Δt	s	0.2		$\Delta\tilde{t} = \Delta t/t_0$	5.0×10^{-5}	
Interface mobility	L_σ	$m^3\,(J \cdot s)^{-1}$	2.5×10^{-6}	1.5×10^{-8}	$\tilde{L}_\sigma = L_\sigma \cdot (E_0 \cdot t_0)$	1.5×10^{5}	9.0×10^{2}
Barrier Height	W	$J \cdot m^{-3}$	1.18×10^{6}	2.05×10^{6}	$\widetilde{W} = W/E_0$	0.08	0.14
Gradient Coefficient	κ_0	$J \cdot m^{-1}$	3.68×10^{-6}	6.38×10^{-6}	$\tilde{\kappa}_0 = \kappa_0 \cdot (E_0/l_0^2)$	2.45×10^{-5}	4.25×10^{-5}
Anisotropy	δ	–	0.03	0	–	0.03	0
Li^+ Diffusion Coefficient	D	$m^2 \cdot s^{-1}$	1.0×10^{-15}	1.0×10^{-12}	$\widetilde{D} = D/({l_0}^2/\Delta t_0)$	4.0×10^{-4}	0.4
Conductivity	σ	$S \cdot m^{-1}$	1.0×10^{7}	1.0×10^{-5}	$\tilde{\sigma} = \sigma \cdot (\Delta t_0 RT)/(c_0 F^2 {l_0}^2)$	2.51×10^{7}	2.51×10^{-5}
Young's Modulus	Y	$J \cdot m^{-3}$	4.9×10^{9}	1.5×10^{11}	$\tilde{Y} = Y/E_0$	3.27×10^{2}	1.00×10^{4}
Poisson Ratio	ν	–	0.362	0.257	–	0.362	0.257
Electrochemical pre-factor	L_η	s^{-1}	0.005	–	$\tilde{L}_\eta = L_\eta \cdot t_0$	20	–
Symmetric factor	α	–	0.5	–	–	0.5	–
Nucleation rate pre-factor	J_0^*	–	200	–	–	200	–
Inhomo correction factor	ζ	–	1	–	–	1	–

Phase-field simulation input parameters were normalized by a characteristic length $l_0 = 1 \times 10^{-4} m$, a characteristic energy density $E_0 = 1.5 \times 10^{7} J \cdot m^{-3}$, the Li ion bulk concentration of LLZO $c_0 = 42.2 \times 10^{3}\ mol \cdot m^{-3}$, and a characteristic time step $\Delta t_0 = 4 \times 10^{3} s$ at room temperature $T = 298K$.

5.2.2 Formulate the total energy

In this section, we will formulate the total energy of the inhomogeneous system in detail. The total energy as written in equation (5-1), consists of four contributions, local free energy, gradient energy, electrostatic energy and mechanical energy. The variable $\tilde{c}_i = c_i/c_0$ is a set of dimensionless concentrations of species, (i.e. $i = Li^+, e^-$) where c_0 is the bulk concentration of the solid phase. φ is the electrostatic potential. The local energy density, f_{local}, is further written as $f_{local} = f_0(\xi, \phi_g) + c_0 RT \sum_i \tilde{c}_i \, ln\tilde{c}_i + \sum_i c_i \mu_i^{\ominus}$, where R, T and $\mu_i^{\ominus}$ are gas constant, temperature and the standard chemical potential of species i, respectively. f_0 is formulated as

$$f_0 = b_1\xi^2(1-\xi)^2 + \sum_{g=1}^{N} b_2{\phi_g}^2(1-\phi_g)^2 + \sum_{p=1}^{N}\sum_{q\neq p}^{N}\frac{b_3}{2}{\phi_p}^2{\phi_q}^2 + \sum_{g=1}^{N}\frac{b_4}{2}\xi^2{\phi_g}^2 \quad (5\text{-}5)$$

where the phenomenological parameters are set to be $b_1 = b_2 = 1$ and $b_3 = b_4 = 3$, so that the equilibrium states are represented by the degenerate minima with equal depth on the landscape of f_0 at values of 0 or 1 for the phase-field variables. The gradient energy density is in the form of $f_{grad} = \frac{1}{2}\kappa_\xi (\nabla\xi)^2 + \sum_{g=1}^{N}\frac{1}{2}\kappa_\phi (\nabla\phi_g)^2 - \kappa_{GB}\sum_{p=1}^{N}\sum_{q\neq i}^{N}\nabla\phi_p\nabla\phi_q$, where κ_ξ, κ_ϕ and κ_{GB} are the gradient coefficients associated with Li metal surface energy, solid electrolyte surface energy, and solid electrolyte GB adhesion energy, respectively. The surface energy anisotropy of Li metal is incorporated by $\kappa_\xi = \kappa_0[1 + \delta cos(\omega\psi)]^2$, where κ_0 is related to the average Li metal surface energy and interface width, δ, ω and ψ are the anisotropy strength, crystallographic symmetry mode ($\omega = 4$ for body-centered cubic Li metal), and the angle between the reference axis and the normal direction of surface migration, respectively. The current model assumes isotropic solid electrolyte properties, and thus constant values are used for κ_ϕ and κ_{GB}. $f_{elec} = F\sum_i nc_i\varphi$ is the electrostatic energy density, where n is the valence of species and F is the Faraday constant. The elastic energy density is expressed as $f_{mech} = \frac{1}{2}C_{ijkl}(\xi, \phi_g)(\varepsilon_{ij} - \varepsilon_{ij}^0)\cdot(\varepsilon_{kl} - \varepsilon_{kl}^0)$, where the effective stiffness of the system is given by $C_{ijkl}(\xi, \phi_g) = \left[h(\xi)C_{ijkl}^{\xi} + \sum_{n=1}^{N} h(\phi_n)C_{ijkl}^{\phi}\right]$,

interpolated by function $h(\xi) = \xi^3(10 - 15\xi + 6\xi^2)$. C_{ijkl}^{ξ} and C_{ijkl}^{ϕ} are the corresponding elastic stiffness tensors of Li metal and solid electrolyte, respectively. Under the isotropic assumption, the eigen strain is written as $\varepsilon_{xx}^0 = \varepsilon_{yy}^0 = \varepsilon_{zz}^0 = \sum_{g=1}^{N} \xi \phi_g^0 \left(\Delta V_{\phi_g}\right)^{-3}$, where ϕ_g^0 and ΔV_{ϕ_g} are the initial field value and the volumetric change compared to the initial volume of the g-th grain, respectively.

5.2.3 Mass transport and electrostatic potential

The phase-field evolution equations (5-2) and (5-3) were solved together with mass transport and electrostatic potential evolution equations. The transport of Li ion in the system is governed by Nernst-Planck equation,

$$\frac{\partial \tilde{c}_{Li+}}{\partial t} = \nabla \cdot \left[D \nabla \tilde{c}_{Li+} + \frac{D \tilde{c}_{Li+}}{RT} F \nabla \varphi \right] - \frac{c_s}{c_0} \frac{\partial \xi}{\partial t} \tag{5-6}$$

where the effective Li ion diffusion coefficient D of the system is interpolated as $D = D_{anode} h(\xi) + \sum_{g=1}^{N} D_{SE} h(\phi_g)$. D_{anode} and D_{SE} are the Li ion diffusion coefficients in Li metal anode and solid electrolyte bulk, respectively (assume $D_{anode} \ll D_{SE}$). The last term is the electrodeposition reaction induced Li ion consumption/production at the electrode/electrolyte interface, where $c_s = 7.64 \times 10^4\ mol \cdot m^{-3}$ is the site density of Li metal. The electrostatic potential distribution is described by a Poisson-type equation with a reaction rate-related term accounting for the temporal charge annihilation/generation at anode surface:

$$\nabla \cdot \left[\sigma \cdot \nabla \left(\varphi(\boldsymbol{r}, t) \right) \right] = I_R \tag{5-7}$$

where the effective conductivity of the system, σ, is interpolated as $\sigma = \sigma_{anode} h(\xi) + \sum_{g=1}^{N} \sigma_{SE} h(\phi_g)$, in which σ_{anode} and σ_{SE} are the conductivities of Li metal anode and solid electrolyte bulk, respectively. The source term, $I_R = nF c_s \frac{\partial \xi}{\partial t}$, is correlated with the

electrodeposition reaction rate. A detailed description of the Li ion transport and electrostatic part of the model can be found in reference [120].

5.2.4 Incorporating the impact of solid electrolyte surface electrons

According to the previous study [211], the surface LLZO could be either stoichiometric or non-stoichiometric since both have similar surface energies. Not only the lower bandgap (2.3 eV) from the stoichiometric surface would get more electrons in conduction bands than bulk, but also the non-stoichiometric surface (Li segregated) would have metal-like behavior because the Fermi level has been lifted to conduction bands. This implies there are some electrons would transfer from anode to LLZO surfaces. Even though, the surfaces could still maintain neutral since the measured electrical conductivity (~10^{-8} S cm^{-1}) [212] is much lower than the measured Li-ion conductivity (~10^{-4} S cm^{-1}) [213], it is expected that the Li-ion could sufficiently compensate the charges of additional electrons on the LLZO surfaces. This amplifies the effect of trapped electrons on the extended internal defects, or a "worst" scenario for Li-dendrite nucleation. Therefore, to estimate the intrinsic surface electron concentration in LLZO, we could use the density of states of non-stoichiometric LLZO surface as input for the phase-field model and assume constant equilibrium electronic surface states during electrodeposition. The electron distribution of a given system is described as:

$$\bar{n} = \int_{-\infty}^{+\infty} F_{Fermi}(\bar{\varepsilon}) D_{DOS}(\bar{\varepsilon}) d\bar{\varepsilon} = \int_{-\infty}^{+\infty} \frac{D_{DOS}(\bar{\varepsilon})}{1+e^{(\bar{\varepsilon}-\bar{\varepsilon}_F)/k_b T}} d\bar{\varepsilon} \quad (5\text{-}8)$$

where $\bar{\varepsilon}$ is the energy of states, F_{Fermi} is the Fermi function, D_{DOS} is the density of states per volume in the unit of $[(eV \cdot \text{Å}^3)^{-1}]$, $\bar{\varepsilon}_F$ is the Fermi level, k_b is the Boltzmann constant and T is the temperature. The surface trapped electron concentration at room temperature, c_{surf}, can thus

be estimated with the 0 K DFT data and a temperature correction factor (λ_T), by integrating at the Fermi level,

$$c_{surf} \approx \bar{n}_{Fermi} = \int_{\bar{\varepsilon}_F - k_bT}^{\bar{\varepsilon}_F + k_bT} \frac{\lambda_T D_{DOS}(\bar{\varepsilon}_F)}{1+e^{(\bar{\varepsilon}_F - \bar{\varepsilon}_F)/k_bT}} d\bar{\varepsilon} \approx 2k_bT \frac{\lambda_T D_{DOS}(\bar{\varepsilon}_F)}{2} = \lambda_T D_{DOS}(\bar{\varepsilon}_F) k_bT \quad (5\text{-}9)$$

Taking unit value for λ_T and DFT data of $D_{DOS}(\bar{\varepsilon}_F)$, the concentration of the trapped electrons on the surface of nonstoichiometric c-LLZO was calculated to be around $0.337\ mol/L$. [211] . Since the focus is on the intrinsic and static material properties on the internal defects in SE, we did not consider how the Fermi level changes with the applied voltage.

The electron concentration decays sharply from solid electrolyte surface into bulk, which can be described using the calculated concentrations of surface trapped electrons, c_{surf}, and the phase-field order parameters in the form of

$$c_e = \xi + \sum_i c_{surf}(1-\xi)^2(1-\phi_i)\,\chi_i \quad (5\text{-}10)$$

where ξ and ϕ_i are the phase-field order parameters identifying the Li metal phase and ith solid electrolyte grain, respectively. χ_i is a step function confining the electrons within the i-th solid electrolyte grain surface region,

$$\chi_i = \begin{cases} 1, & |\phi_i - 0.5| < \rho \\ 0, & otherwise \end{cases} \quad (5\text{-}11)$$

where ρ is a surface thickness parameter that equals 0.05 in this work.

5.2.5 Dendrite nucleation rate

Based on classical nucleation theory, the nucleation rate of the precipitated phase can be generally written as,

$$J^* = J_0^* \exp\left(-\frac{\zeta \Delta G^*}{k_bT}\right) \quad (5\text{-}12)$$

where J_0^* is an empirical kinetic pre-factor. Given the complexity and randomness of the polycrystalline solid electrolyte structure, we introduced a correction factor, ζ, to describe the local inhomogeneity deviated from classical nucleation, such that both homogeneous and heterogeneous scenarios were considered in the model. $\Delta G^*$is the nucleation activation energy to form a stable nucleus. The total energy variation during a classical nucleation process is written as

$$\Delta G = -\left(\frac{\Delta\mu}{V_m}\right)\cdot\frac{4}{3}\pi r^3 + 4\pi r^2\cdot\gamma \tag{5-13}$$

where $\Delta\mu$ and γ are the chemical potential difference and interfacial energy between matrix and precipitate phase, respectively. V_m is the molar volume of the precipitate phase and r is the nuclei radius, ΔG^*, is determined by the saddle point of ΔG at critical radius $r^* = \frac{2\gamma V_m}{\Delta\mu}$, where the interfacial energy increase just gets compensated by the free energy decrease of phase transition,

$$\Delta G^* = \Delta G|_{r=r^*} = \frac{16\pi\gamma^3 {V_m}^2}{3\Delta\mu^2} \tag{5-14}$$

During Li electrodeposition process, the electrochemical potential difference between precipitated Li nuclei and solid electrolyte matrix is given by $\Delta\bar{\mu} = -RTln\frac{\tilde{c}_{Li+}\tilde{c}_e}{a_{Li}} - F(E^\Theta - \Delta\varphi) = F\eta$, where a_{Li} is the activity of Li metal atom (treated as 1 in this work), $E^\Theta$is the standard half-cell potential, and $\Delta\varphi$ is the interfacial potential difference between precipitated Li metal and solid electrolyte phase. Therefore, the nucleation rate can be rewritten as

$$J^* = J_0^* \exp\left(-\frac{16\zeta\pi\gamma^3 {V_m}^2}{3F^2\eta^2 k_b T}\right) \tag{5-15}$$

The detailed derivation of Li electrodeposition thermodynamics can be found in reference [120].

5.3 Results and discussion

5.3.1 Single crystal and bi-crystal SE systems

As a validation of the model, we did a series of standard simulation tests on simple SE systems. Firstly, we carried out interface stability analyses for a Li metal/single crystalline SE system by adding a sinusoidal electrochemical driving force at Li metal surface to mimic the Li electrodeposition, as shown in Figure 5-2 (a) to (d). This test is similar to the interface stability analyses in the solid electrolyte model of a Li metal/polymer electrolyte system proposed by Newman. Instead of analyzing the trend of instability at interface with fixed geometry in Newman model, phase-field model captured the interface morphology evolution. We check the Li metal/single crystal SE interface morphology evolution during electrodeposition with different SE shear moduli, ranging from one time to thirty times of the Li metal modulus. This moduli range covers the mechanical properties of most existing polymer and ceramic SEs. All simulations started with flat Li metal/SE interfaces, as shown in Figure 5-2 (a). The final morphologies demonstrated that the SE deformation increases as SE shear modulus decreases from thirty to one times of Li metal modulus, as shown in Figure 5-2 (b) to (d). And it can be concluded that the Li metal/single crystalline SE interface loses its stability when SE modulus is decreased to around the same order of Li metal modulus, which is in agreement with the conclusion in Newman model.

To go beyond classical models, we further investigated the Li plating morphology evolution in polycrystal solid electrolyte by introducing a straight grain boundary perpendicular to the Li metal surface in a bi-crystal system. Solid electrolyte of same initial geometry but with different moduli ranging from thirty times to one time of Li metal modulus were simulated as shown in Figure 5-2 (f-h). All simulations began with flat Li metal surfaces as show in Figure 5-2

(e). Uniform electrochemical driving forces were applied on Li metal surfaces to mimic Li electrodeposition. From the final morphologies of these bi-crystal systems as shown in Figure 5-2 (f-h), we observed faster Li electrodeposition as the grain boundary regions, which is because the mechanically-weak grain boundary regions are less resistant to dendrite growth than the bulk. Additionally, it is found that the Li dendrite protrusion morphologies at grain boundary regions vary with solid electrolyte moduli. The splitting angle of the protrusion increases as solid electrolyte modulus decreases, which can be explained by the elastic deformation in the solid electrolyte phase. By now, we have validated the phase-field model from single crystal systems, and overcome the fixed geometry limit in classical models, extracting more important information on polycrystalline systems.

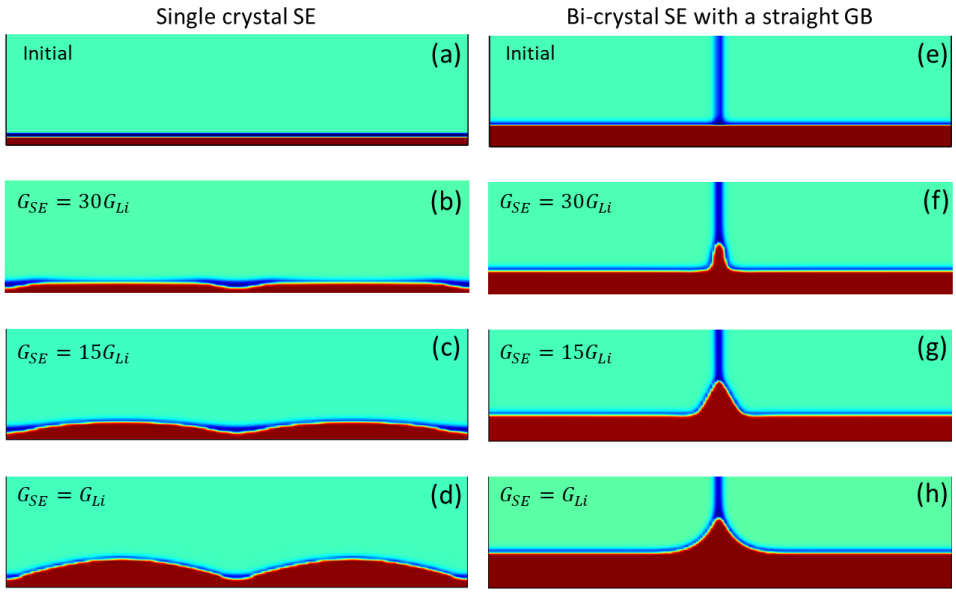

Figure 5-2. Phase-field simulation results of morphology evolution in (a-d) Li metal/single crystal solid electrolyte system under sinusoidal Li electrodeposition driving force and (e-h) Li metal/bi-crystal solid electrolyte with a straight grain boundary under uniform Li electrodeposition driving force, with different solid electrolyte shear moduli ranging from one time to thirty times of Li metal modulus.

5.3.2 Solid electrolyte parametric optimization

In this section, we use the as-developed phase-field model of Li plating in solid electrolyte to investigate electrodeposition morphologies evolution and their risks of dendrite penetration in polycrystalline SE systems. As discussed in the section 5.1, the dendrite issues in solid electrolyte batteries are either mechanical-driven or electronical-driven. We hereby parameterized all related properties of solid electrolyte and examined their impacts on Li plating behavior. To quantify the simulation results, we designed a standard $500 \times 500\ \mu m^2$ Li metal/SE system with three grains separated by a straight crack and a straight grain boundary, as shown in Figure 5-3. All simulations started with flat Li metal surfaces. Constant voltage conditions of –0.1 V were applied for all systems. We adjusted the parameters related to solid electrolyte properties in a physical range that covers most existing solid electrolyte systems and checked the dendrite penetration depths and total dendrite amount in the crack and grain boundary of each system. The investigated solid electrolyte properties and their corresponding ranges are: grain boundary adhesion energy ($0 - 1\ J/m^2$), grain boundary surface electron density ($0 - 0.4\ mol/L$); solid electrolyte elastic modulus ($0.735 - 1568\ GPa$, or 0.25 to 320 times of the Li metal modulus) and Li ion conductivity at grain boundary ($0 - 2.4\ mS/cm$). For the invariant properties in each study, we set as grain boundary adhesion energy $0\ J/m^2$, grain boundary electron density $0\ mol/L$, elastic modulus $147\ GPa$ (bulk LLZO data), and grain boundary Li ion conductivity $0\ mS/cm$. Their final morphologies after 800 s are presented in Figure 5-3.

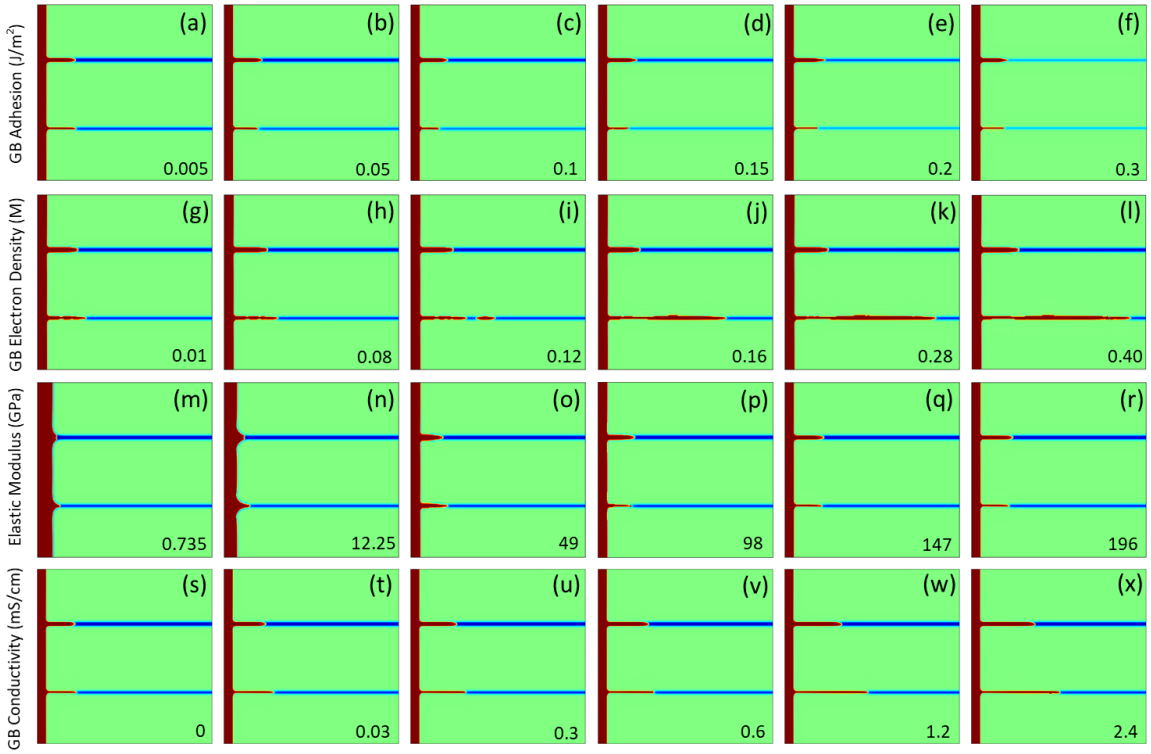

Figure 5-3. The final morphologies of Li electrodeposition in designed three-grain solid electrolyte systems of different (a-f) grain boundary adhesion energies; (g-l) grain boundary surface electron densities; (m-r) solid electrolyte elastic moduli; and (s-x) grain boundary Li ion conductivities.

The phase-field simulation morphologies results were quantified and plot into a solid electrolyte map as shown in Figure 5-4. To evaluate each solid electrolyte property in terms of dendrite suppression, two criteria, i.e. total dendrite amount and dendrite penetration depth, were used to assess their capabilities and efficiencies to impede metallic Li nucleation and growth in the grain boundaries and cracks of solid electrolytes. In order to directly evaluate and compare all solid electrolyte properties, we normalized the value of each parameterized properties into unitless intensities in the range of 0 to 1. Several trends and conclusions on dendrite intergranular penetration and suppression at grain boundaries can be drawn from the design map in Figure 5-4 (a) and (b): (1) Non-zero solid electrolyte surface free electrolyte density causes tremendously increase in the amount of dendrite and dendrite penetration depth at grain boundaries (red curves)

due to the additional electrochemical driving force and the isolated dendrite nucleation as shown in Figure 5-3; (2) Higher Li ion conductivity at grain boundaries leads to larger dendrite amount and deeper dendrite penetration (green curves), which holds yet only for the scenario of perpendicular grain boundaries in this study. (3) Increased grain boundary adhesion energy results in slightly mitigated intergranular growth in terms of both total dendrite amount and penetration depth (blue curves); (4) Modulus has complicated impact on dendrite penetration, which will be further discussed later. Similar trends but less efficiencies were observed for the impact of each properties but modulus on dendrite penetration in the cracks of solid electrolyte, as shown in Figure 5-4 (c) and (d).

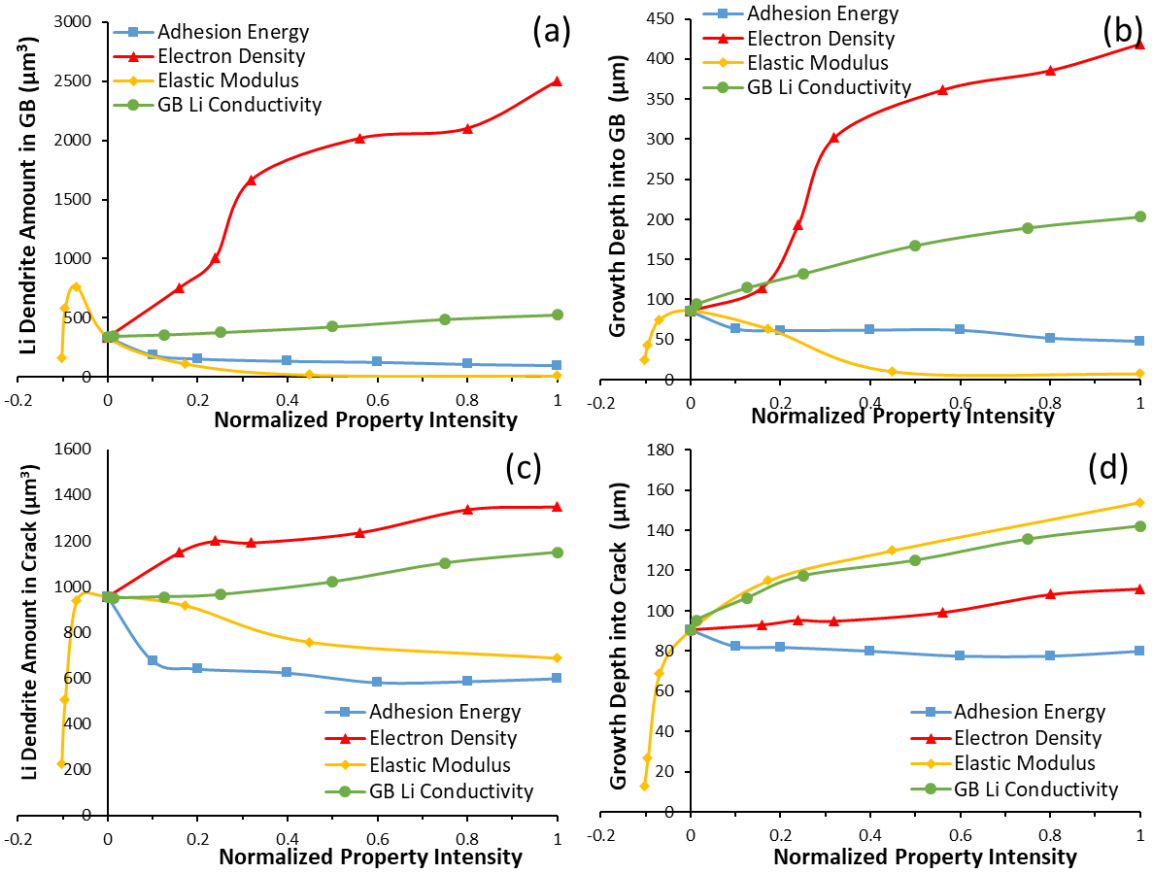

Figure 5-4. A design map generated from phase-field simulations of polycrystalline solid electrolytes with perpendicular straight grain boundaries and cracks: (a) The Li dendrite total amount and (b) penetration depth in grain boundaries (GBs); and (c) Li dendrite total amount and (d) penetration depth in cracks during electrodeposition in solid electrolytes with different GB adhesion energies, GB surface electron densities, solid electrolyte moduli, and GB Li-ion conductivities, respectively.

Due to the complicated variation trend of solid electrolyte modulus and the moderate impact of grain boundary adhesion energy, we did a systematic study on the coupled impacts of these two properties for both grain boundary and crack, as shown in Figure 5-5. Based on these additional analyses, we further concluded: (1) At grain boundaries, small modulus (comparable or less than Li metal) or extremely large modulus (i.e. $> 800\,GPa$) can effectively suppress intergranular growth, in terms of both dendrite amount and penetration depth, as shown in Figure 5-5 (a) and (b); (2) At cracks, decreased modulus leads to less dendrite growth due to the larger volume space from solid electrolyte deformation, as shown in Figure 5-5 (c) and (d); (3) Increased grain boundary adhesion energy suppresses dendrite intergranular growth at grain boundaries, but has no prominent impact on cracks. This is interesting and ironic since it is once believed that solid electrolyte can suppress dendrite growth because of its hardness, and the harder the better. But it was neglected that solid electrolyte can hardly be perfect and homogeneous, which contains defects and grain boundaries, and the increased mechanical strength also magnifies the mechanical weakness at these defects. On the contrary, soft solid electrolyte can compensate these mechanical weaknesses by larger elastic deformation, which explains the variation trends in Figure 5-5.

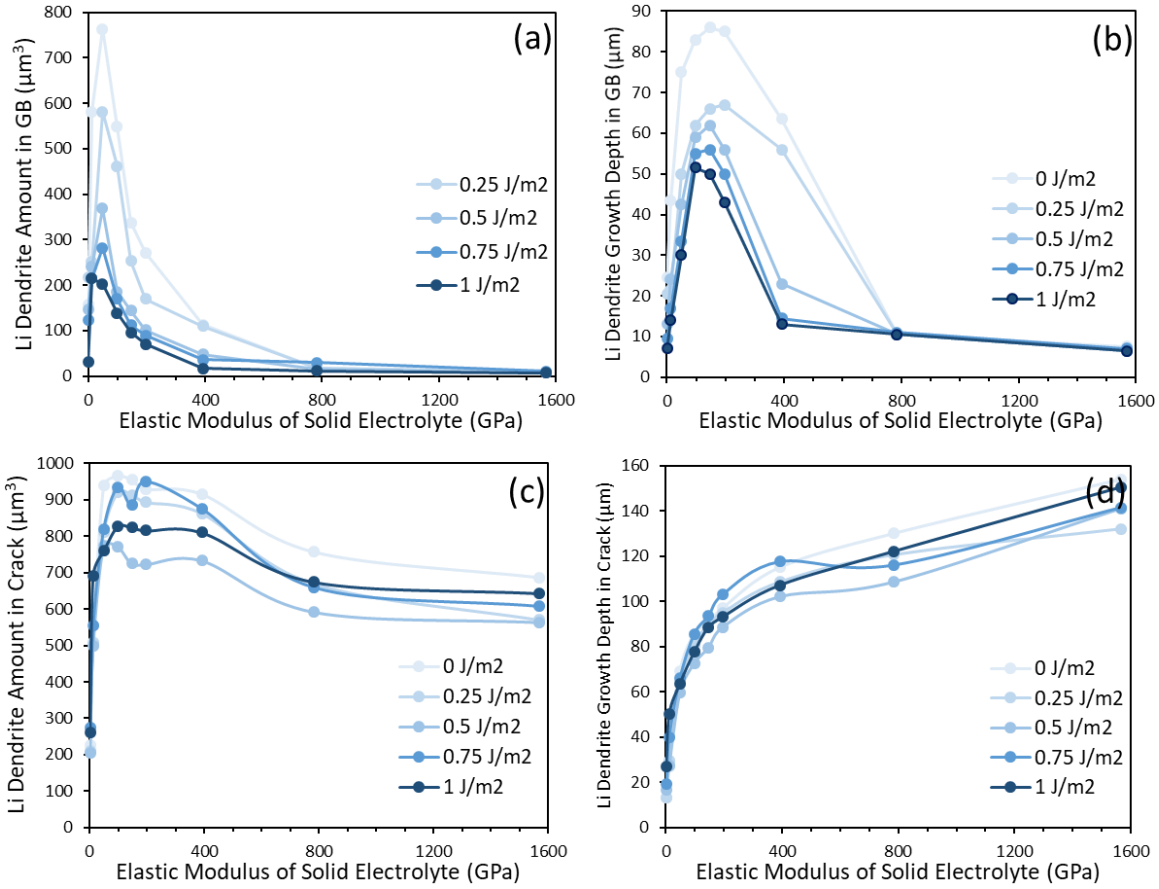

Figure 5-5. Coupled impacts of solid electrolyte modulus and grain boundary adhesion energy on dendrite amount at (a) grain boundaries and (c) cracks, and dendrite penetration depth at (b) grain boundaries and (d) cracks, respectively.

To conclude this section, a parametric study of the major solid electrolyte properties impacts on dendrite growth and penetration in polycrystalline solid electrolyte systems were conducted. A design map was generated based on systematic phase-field simulation results. Several general criteria and safety range of each properties were summarized to guide the design of healthy solid electrolyte systems.

5.3.3 Grain size impacts in polycrystalline solid electrolyte systems

In this section, we will further investigate the grain size impact on dendrite growth and penetration by moving from standard testing systems to the polycrystalline solid electrolyte in real life. The polycrystal solid electrolyte structures of different grain sizes in this study were generated from phase-field grain growth code. The atomic calculation results of LLZO surface electronic analyses were incorporated in the multiscale phase-field model. Here we treated the internal pore surfaces and grain boundaries with the same electronic properties. More detailed band structure calculations of grain boundaries need to be performed in the future. Since electrons respond almost instantly to the electrostatic potential compared with Li ion transport kinetics in solid electrolytes, we calculated the static surface electron concentration in each material based the DFT DOS results [211, 214].

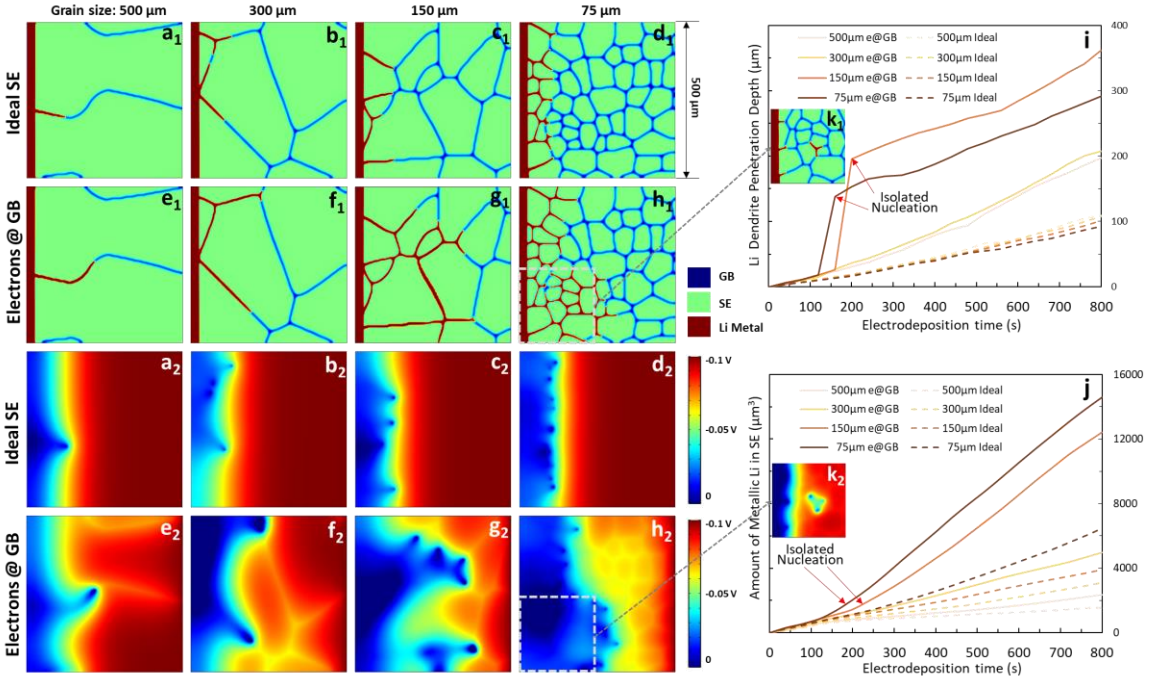

Figure 5-6. Phase-field simulation results on the impacts of surface trapped electrons and grain size on the morphologies and electric potential distributions after 800s Li electrodeposition in a $500 \times 500\ \mu m^2$ half-cell. A comparison of the final phase morphologies in (a1-d1) the ideal SEs with excess electron-free surfaces and (e1-h1) the real SEs with the calculated surface electron

concentrations from DFT, in a series of grain sizes. And a comparison of their corresponding final electric overpotential distributions for the SEs in (a1-h1). The dynamic evolution of (i) the Li dendrite penetration depths and (j) the total amount of metallic Li in SEs of different grain sizes. The initiation of isolated dendrite nucleation is demonstrated by (k1) the phase morphology and (k2) the corresponding electric potential distribution in the SE of the 75 μm grain size at 200s.

The Li electrodeposition processes in SEs of grain sizes ranging from 75 to 500μm were simulated in identical 500 $\mu m \times 500$ μm 2D half-cells with a constant electric overpotential of -0.1V. The properties of bulk c-LLZO (i.e. elastic moduli, Li ion conductivity, surface energy, etc.) were used for all SEs in this study (detailed in Table 5-1). To directly demonstrate the influence of excess surface electrons on electrodeposition, we compared two idealized scenarios of surface electronic states: "real" LLZO polycrystalline SEs referring to the extended internal defects with excess surface electron concentration ($c_e = 0.337\ mol/L$) and "ideal" LLZO SEs referring to the extended internal defects with no surface electrons, while both have identical structures. The spatial and temporal evolution of the multiphase morphology, Li ion concentration and electric potential during electrodeposition were tracked over the simulation time of 800s.

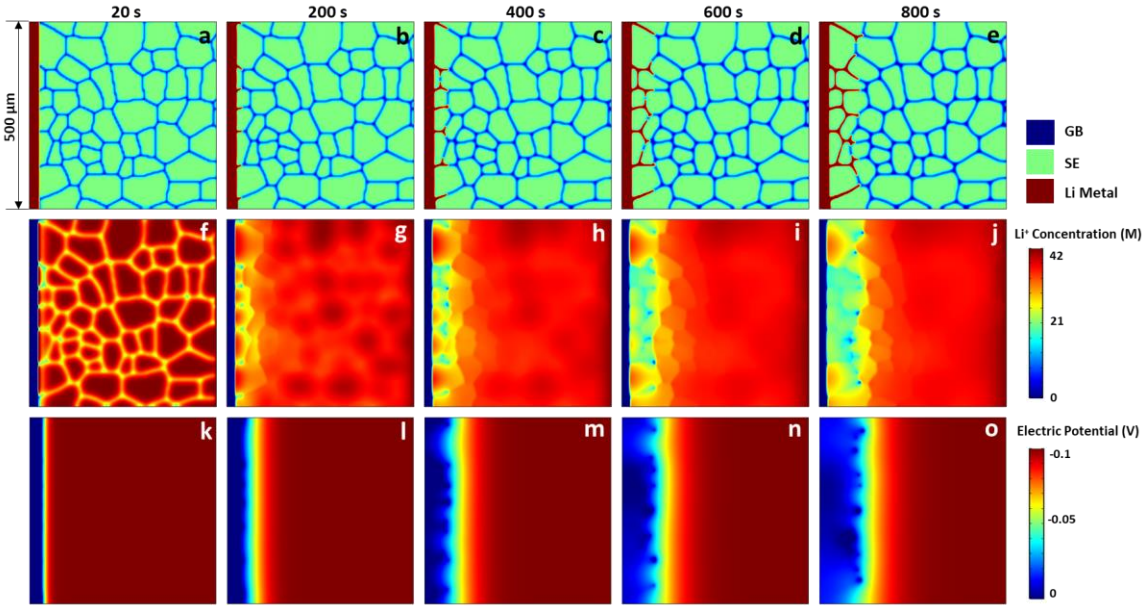

Figure 5-7. Morphology, Li ion concentration and electric potential evolution during electrodeposition in ideal LLZO SSEs of 75 μm grain size with no surface electrons.

The final morphologies of 800s electrodeposition show larger amount of metallic Li and deeper dendrite penetration depth in real LLZO (Figure 5-6 (a1-d1)) than the ideal LLZO (Figure 5-6 (e1-h1)) for all SE grain sizes. This difference is due to the additional electrochemical driving force from excess surface electrons in real LLZO. The contrast between the real and ideal cases becomes more prominent when isolated nucleation of metallic Li took place in the real SEs with the grain sizes of 75 μm and 150 μm (Figure 5-6 (g1) and (h1), respectively.). This is because the additional electrodeposition sites provided by the isolated nucleation inside SE significantly increase the intergranular dendrite penetration depth and growth rate. A more clear comparison is quantitatively demonstrated by the dynamic evolution curves of the total amount of Li (corresponding to capacity loss) and the dendrite penetration depth in SEs, where the two abrupt rising steps in the penetration depth (Figure 5-6 (i)) and the sudden deviations in the Li dendrite amount increasing rates (Figure 5-6 (j)) highlighted by red arrows, indicate the initiation of isolated nucleation (Figure 5-6 (k1)). On the other hand, the formation of metallic Li at the isolated nucleation sites will slow down or even block the intergranular Li ion transport (comparing Figure 5-7 (g-j) and Figure 5-8) and cause an abrupt drop in the local electric potential (Figure 5-6 (k2)), which impedes the normal electrodeposition at the anode substrate.

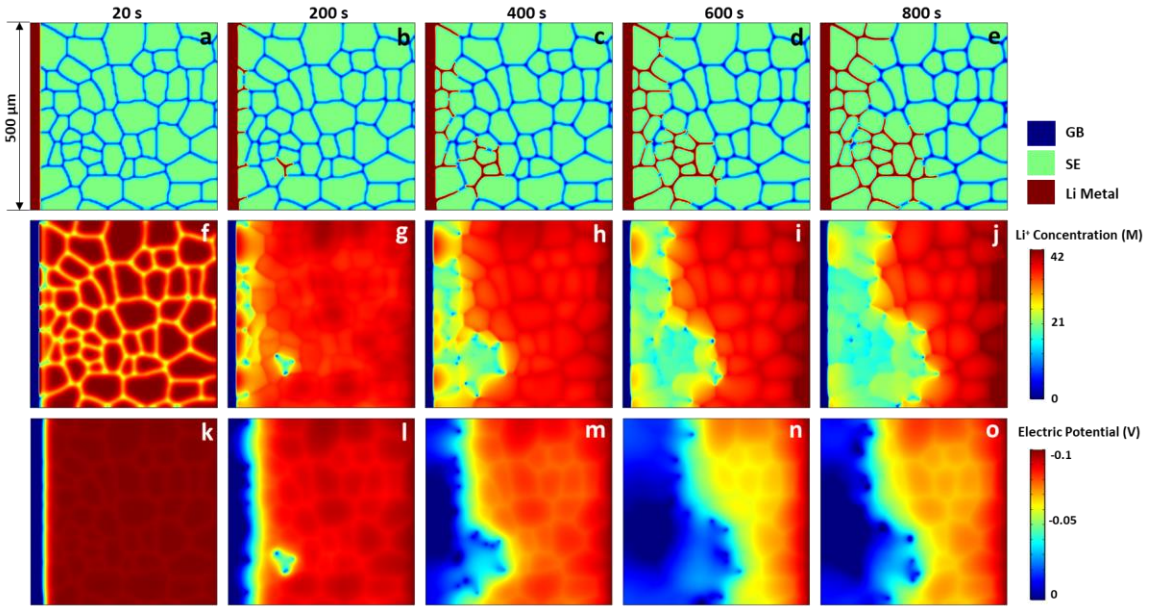

Figure 5-8. Morphology, Li ion concentration and electric potential evolution during electrodeposition in real LLZO SSEs of 75 μm grain size with excess surface electrons.

The impacts of surface trapped electrons are dynamically demonstrated by the comparison of the morphology, Li ion concentration and electric potential evolution snapshots during the Li electrodeposition processes in the 75 μm grain size "ideal" LLZO (Figure 5-7) and real LLZO (Figure 5-8) half cells, respectively. From the morphology evolution figures, the Li intergranular growth is dramatically accelerated in the real LLZO system (Figure 5-8 (a-e)) than the ideal LLZO system (Figure 5-7 (a-e)), which is due to the increased electrochemical driving force contributed from the trapped surface electrons as well as the additional dendrite growth sites at the isolated nucleation spots within the healthy SE region, as mentioned in the main text. Meanwhile, the isolatedly-formed Li metal will hinder or even shut down the intergranular Li ion transport (Figure 5-8 (j-g)) and lead to the sudden decrease of local electric potential (Figure 5-8 (l-o)), which impedes the normal electrodeposition at anode substrate.

5.4 Conclusion

In this chapter, we developed a general phase-field model to study the Li electrodeposition morphology evolution in solid electrolyte systems. This model incorporates mechanical interactions between the evolving Li metal phase and the polycrystalline solid electrolyte phases, and integrates the DFT-predicted electronic properties of solid electrolyte surfaces. Firstly, we validated the model through a series of designed standard test systems including single crystal solid electrolyte, bi-crystal solid electrolyte with a straight grain boundary. Interface stability analyses at Li metal/single crystal solid electrolyte interface were carried out and compared with Newman model. Li electrodeposition behavior at bi-crystal grain boundary was also checked via morphology evolution with different solid electrolyte modulus. Then, the impacts and efficiencies of major solid electrolyte properties on dendrite intergranular growth and penetration were systematically investigated via designed tri-crystal solid electrolyte systems with a straight grain boundary and a crack. The studied solid electrolyte properties include grain boundary adhesion energy, solid electrolyte surface electron density, solid electrolyte modulus, and Li ion conductivity at grain boundary. Finally, we moved on to polycrystalline systems in real life and examined the grain size effects on dendrite intergranular growth and penetration. Based on quantitative analyses of these results, a design map was generated to optimize the performance of solid electrolyte systems.

Chapter 6

Conclusions and future work

6.1 Summary and conclusions

In this dissertation, we thoroughly studied the Li electrodeposition behavior and dendrite formation mechanism from combined computational modeling and experimental methods. A multiscale modeling framework was developed for both liquid and solid electrolyte Li metal batteries, coupling atomic physics with mesoscale transport and morphology evolution. This model reveals the intrinsic origin of dendrite growth and promotes dendrite-free Li metal anode design for next-generation batteries. The main contributions of the dissertation include:

I. In Chapter 2, the Li metal/SEI interface mechanical and electrochemical properties were studied by DFT calculations. Li_2CO_3 and LiF, the two most important SEI inorganic components, were selected to build interface supercells with Li metal. The calculated interfacial energy and work of adhesion show that Li (001) is the most energetically-favored orientation interfaced with both Li_2CO_3 and LiF, and that Li_2CO_3 shows higher interfacial mechanical stability than LiF. Further calculations on DOS and electrostatic potential profile of each interface demonstrate larger electron tunneling barrier for LiF/Li interface, denoting LiF is better in blocking electron leakage than Li_2CO_3. Particularly, in charge cycles with limited Li ion transport from electrolyte to anode surface, undesirable Li dendrites are more likely to nucleate and grow within SEI at Li_2CO_3/Li than LiF/Li interfaces. Based on this DFT interfacial study, we are able to link each SEI component with its mechanical and electrochemical properties, which can be used as descriptors to screen SEI and design artificial electrode coating layers for LIBs.

II. In Chapter 3, the SEI formation mechanism and growth dynamics were investigated by an isotope-assisted time-of-flight secondary ion mass spectrometry (TOF SIMS) method. It is found that the initial SEI formation takes place at the SEI/electrode interface, and new SEI forms beneath the existing SEI layer through a "bottom-up" process. Compositionally, the dense inorganic phase forms beneath and after the porous organic phase layer. This growth mechanism leads to the observed two-layered structure of SEI, where the organic layer is permeable for the electrolyte. This growth mechanism is closely related to the competition of the two different reduction reactions associated with the unbalanced electrolyte and electron concentrations at different stages of SEI formation process. It should be noted that the "bottom-up" growth mechanism may dominate only in the initial stage of SEI formation during the battery pre-cycling. As an SEI grows thicker and more stable, other coupled growth mechanisms may take place. This work provides insights for the SEI formation mechanism from a dynamical perspective, and the in-depth understanding of SEI formation assists electrolyte additives and artificial electrode coatings design. Meanwhile, using Li isotopes as a time indicator, this proposed isotope-assisted TOF SIMS approach can also be extended to study other dynamics-related topics.

III. In Chapter 4, we developed a multiscale model to understand and predict the metal electrodeposition behavior in liquid electrolytes by integrating atomic calculations of the charge-transfer reaction and phase-field model of electrodepositing morphology evolution. The dendritic growth of Li plating and the polyhedral morphology of Mg plating processes were reproduced and compared from cation diffusion and electrostatic potential distribution evolution. It was found that the cation desolvation induced low intrinsic exchange current is mainly responsible for the smooth Mg plating morphology although the surface energy and its anisotropy can also modulate the plating morphology.

More importantly, this study suggests the most efficient way to mitigate dendrite growth at Li metal anodes can be achieved via electrolyte engineering by increasing either the desolvation barrier or the cation-solvation surface coverage. The scale bridging between the mesoscale methods and atomistic calculations can be generalized and employed on other chemical and electrochemical processes, and achieve a parameter-free predictive modeling approach.

IV. In Chapter 5, we extended the phase-field model of metal electrodeposition to solid electrolyte systems, by integrating multiphase solid mechanics and explicit dendrite nucleation. The DFT-calculated electronic properties of solid electrolyte surfaces were incorporated as phase-field input parameters. The model was validated through a series of standard test including interface stability in single crystal solid electrolyte system, morphology evolution at a straight grain boundary in bi-crystal solid electrolyte system. The testing results are in agreement with Newman model, and further goes beyond the fixed geometry limit of the existing models to generate more important information. Then, the impacts and efficiencies of major solid electrolyte properties (grain boundary adhesion energy, surface electron density, modulus, and Li ion conductivity) on dendrite intergranular growth and penetration were systematically investigated via designed tri-crystal solid electrolyte systems. Finally, we examined the grain size effects on dendrite intergranular growth and penetration with realistic polycrystalline solid electrolyte structures from phase-field grain growth codes. Based on quantitative analyses of these results, a design map was generated to optimize the solid electrolyte system design in terms of each studied property, and promote the overall performance of all-solid-state batteries.

6.2 Directions for future work

All-solid-state battery is one of the most important direction for the practical application of Li metal anode and future high energy-density storage. We have developed a general phase-field model for Li dendrite growth in a polycrystalline solid electrolyte half-cell, incorporating Butler-Volmer kinetics, multiphase solid mechanics and explicit dendrite nucleation. The model captured several major reported trends of Li dendrite growth in all-solid-state batteries, namely, Li dendrite intergranular growth, isolated Li-metal formation within pores and grain boundaries, and the sudden increase of Li dendrite penetration depth. These electrodeposition behaviors can eventually lead to an abrupt rise in charging current (at constant voltage) and effective electronic conductivity of SEs, and eventually cause accelerated capacity loss during cycling and a higher risk of short-circuiting. With systematic investigation on major solid electrolyte properties, such as elastic modulus, grain size and grain boundary strength, surface Li ion and electronic conductivities, defects density, etc., the model can predict the Li plating trends and provide quantitative guidance to solid electrolyte design.

However, the current model is still preliminary with several assumptions, approximations and simplified treatments, particularly the descriptions for different kinds of defects that extensively present in various solid electrolyte systems. As we proposed, the Li dendrite growth and penetration mechanisms are either mechanically-driven surface defects filling or electronically-driven dendrite nucleation and growth, both of which involve defects. It is known that engineering materials in general and inorganic materials in particular usually contain internal flaws and defects (i.e. pores, cracks, grain boundaries and triple junctions). Therefore, it is extremely important to model these defects and understand their role in affecting Li plating and dendrite growth. While it is very difficult or impossible to develop a solid electrolyte without defects, it is possible to minimize or eliminate defects which are more prone to Li dendrite

nucleation and growth. For example, according to some DFT calculations, while cracks or pores always exist in a solid electrolyte, not all the crack/pore surfaces will attract electrons and facilitate metallic Li formation, such as LiPON and Li_2S [211]. This discovery suggests that there are at least three ways that a DFT-informed phase-field dendrite growth model can help the design of solid electrolyte materials: (1) design a primary solid electrolyte material whose defects are more Li dendrite resistant; (2) design a Li dendrite resistant secondary phase to modify the pore and grain boundary properties of a primary solid electrolyte to improve its resistance to Li-dendrite growth; (3) design a Li/solid electrolyte interlayer coating to prevent the initial growth of dendrites into the solid electrolyte.

For the solid mechanics part, the phase-field model currently only integrates multiphase elasticity. In realistic all-solid-state batteries, however, Li dendrite can grow via more complicated mechanisms other than the intergranular penetration incorporated in this model. These mechanisms include: (1) growth along with intragranular crack formation and propagation; (2) growth via mechanical extrusion due to external compressive pressure upon initial cell assembly. Therefore, a more comprehensive formulation of the mechanical part is needed for the phase-field model.

Overall, in order to accelerate the design of Li dendrite resistant solid electrolyte materials, we will further extend the existing phase-field model to incorporate new functionalities. The selected advancement in the model are detailed in, but not limited to, the following sections.

6.2.1 Incorporate the plasticity of Li metal into the phase-field model

As mentioned, the mechanical extrusion an important mechanism of Li dendrite growth in al-solid-state batteries. Therefore, the plasticity of Li metal will be incorporated into the existing phase-field model to study the Li metal creep/plastic flow and its impact on plating morphologies and dendrite penetration. The total energy of the inhomogeneous system can be rewritten as

$$F = \int \left[f_{local}(\xi, \phi, \tilde{c}_i) + f_{grad}(\nabla\xi, \nabla\phi) + f_{elec}(c_i, \varphi) + f_{elas}(\xi, \phi) + f_{plas}(\xi, \phi) \right] dV \quad (6\text{-}1)$$

where ξ and ϕ are the phase fields for Li metal and solid electrolyte, respectively. $\tilde{c}_i = c_i/c_0$ is a set of dimensionless concentrations of species, (i.e. $i = Li^+$, e^-) where c_0 is the bulk concentration of the solid phase. φ is the electrostatic potential. There are several contributions to the total energy: local energy (f_{local}) comprised by the chemical potentials of each species and chemical free energy of the phases, interfacial energy introduced through the gradient energy (f_{grad}) of the phase-fields, electrostatic energy (f_{elec}) obtained by solving the current conservation equation, and elastic (f_{elas}) and plastic strain energy (f_{plas}) obtained by solving the elasto-plasticity equations. This approach will also capture the plastic deformation of Li, as suggested by recent experiments [215, 216] [166]. Based on our previous work, many parameters used in the phase-field model, such as surface energy, interface energy, diffusion coefficient, exchange current density, elastic constants, fracture energy can be directly computed from DFT, in addition to experimentally measured values.

Preliminary tests of Li plating at standard single crystalline and bi-grain solid electrolyte systems of different electrolyte moduli and loading conditions will be performed and validated versus analytical solutions and available experimentally measured creep data. Then coupled effects with transport kinetics, solid electrolyte electronic properties, interfacial wetting

conditions, will be systematically studied by phase-field simulations in both standard test and real polycrystalline systems.

6.2.2 Enable crack initiation and propagation in solid electrolyte

While the existing phase-field model captures the dominant failure modes in polycrystalline solid electrolytes, the Li plating behaviors in single crystal and amorphous phase solid electrolytes can be quite different. For example, cracks can initiate and propagate upon the Li plating induced stress concentration in brittle sulfur-based solid electrolyte. Crack nucleation and propagation in solid electrolyte will provide additional path for potential Li dendrite penetration, as shown in Figure 6-1. We will hereby include the phase-field description of crack formation and propagation into existing model based on Griffith's energy criterion and Heaviside function treatment [217]. The extended model will firstly be preliminarily examined by crack evolution standard tests in single crystalline solid electrolyte system under different applied loading. Then electrodeposition and Li ion transport will be coupled and the impacts of crack formation and propagation in solid electrolyte on Li dendrite penetration depth will be systematically investigated under different loading conditions, mechanical properties of solid electrolyte and current densities.

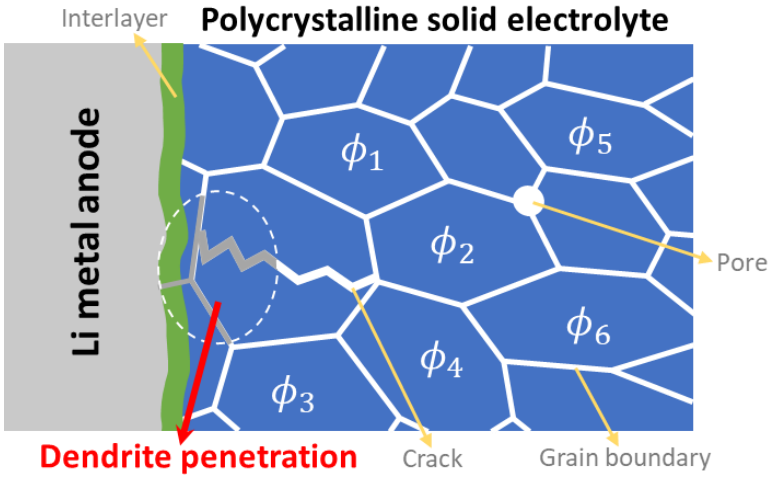

Figure 6-1. Schematic of the proposed mesoscale model incorporating interlayer and intragranular crack propagation in a polycrystal solid electrolyte half-cell system.

6.2.3 Introducing interlayer and/or second phase into the model

We will incorporate and study the impacts of the interlayer and/or the second phase via either the "explicit" or "implicit" approach. In the current model, to describe the microstructure of an N-grain solid electrolyte cell, N+1 independent non-conserved phase-field variables were employed to define each grain or phase with: $\{\xi, (\phi_1, \phi_2, \dots, \phi_g \dots \phi_N)\} = \{1, (0,0, \dots, 0, \dots 0)\}$ for Li metal, $\{\xi, (\phi_1, \phi_2, \dots, \phi_g \dots \phi_N)\} = \{0, (0,0, \dots, 1, \dots 0)\}$ for the i th grain of the solid electrolyte, and $\{\xi, (\phi_1, \phi_2, \dots, \phi_g \dots \phi_N)\} = \{0, (0,0, \dots, 0, \dots 0)\}$ for unspecified internal extended defects. In the implicit model, we will incorporate the properties of this interlayer into the phase-field mode since the interlayer is usually around tens of nanometers in thickness. In the explicit model, an additional phase order parameter will be introduced to the current model and resolve the morphology evolution of the interlayer as an individual phase. We have employed the implicit approach to model the effect of solid electrolyte interphase [1] on Li dendrite growth in liquid electrolytes.[32] All phase-field input parameters related to the layer

properties can be studied and determined from DFT-based calculations. And the impacts of critical interlayer properties on Li plating will be systematically studied from simulations.

6.2.4 More physical and accurate description of defects in solid electrolyte

Surfaces and interfaces in the polycrystal solid electrolyte system play a significant role in the dendrite morphology evolution. The current phase-field model describes a multiphase multigrain solid electrolyte system with isotropic properties, and differentiate the GBs from cracks and pores by using an interfacial adhesion energy term in the gradient energy density formulation. In the proposed work, a more physical and accurate description of polycrystalline solid electrolyte phase will be included into the phase-field model, with stronger coupling with atomic DFT calculations on the energetics, electronic properties and Li ion transport kinetics at GBs as well as surfaces. Specifically, an additional order parameter of grain orientation will be introduced into the existing multigrain phase-field model, if necessary, to connect with the DFT results on different GB structures (e.g. low-angle GBs and high-angle GBs). The differences in the GB electronic states and Li ion diffusion coefficients from bulk, and the impacts of doping and secondary phase at GB will also be incorporated into the model. Temperature impacts on these properties and thus the Li electrodeposition behaviors will also be investigated.

6.2.5 Other innovations and improvements for the phase-field model

Constant current condition of Li plating in phase-field simulation: We will extend the phase field model to perform Li electrodeposition simulation with constant current boundary condition, since it is most commonly used and easily controlled condition in experiments and commercial products. The major challenge in applying constant current condition lies in the

evolving Li metal morphology and varying surface area. We will attempt to realize constant current electrodeposition by controlling the applied voltage based on the feedback of the temporal reaction current. The electric overpotential distribution and the plating morphology (Li-dendrite penetration depth) under constant current condition will be tracked over plating time and compared with those using constant voltage condition. The critical current density for Li to penetrate the solid-electrolyte will be predicted at a given experimental solid electrolyte thickness and microstructure.

Model "Temperature dependent" in phase-field simulation: We will formulate the explicit temperature dependences of each related property (e.g. Li ion diffusion coefficient, equilibrium concentration of solid electrolyte surface trapped electrons, reaction rate constant, etc.). Evaluate their impacts on Li-dendrite penetration depth and critical current density. This will be directly compared with experimental results.

Solid electrolyte microstructure evolution during extended number of cycles and its impact on electrodeposition morphology and battery life: We have been focusing on the electrochemical behaviors within a single charging cycle of the anode side. In the proposed work, we will extend our mesoscale simulations to a number of cycles. The microstructure changes together with the plating/stripping morphology evolutions over cycles will be tracked and investigated for solid electrolytes of different properties. The collected data will be connected with commonly used experimental standards (e.g. Coulombic efficiency, effective conductivity of the solid electrolyte structure, etc.), and input to a battery life model to guide the all-solid-state battery design.

Bibliography

1. Liu, X.-M., et al., *Carbon nanotube (CNT)-based composites as electrode material for rechargeable Li-ion batteries: a review.* Composites Science and Technology, 2012. **72**(2): p. 121-144.
2. Nitta, N., et al., *Li-ion battery materials: present and future.* Materials today, 2015. **18**(5): p. 252-264.
3. Etacheri, V., et al., *Challenges in the development of advanced Li-ion batteries: a review.* Energy & Environmental Science, 2011. **4**(9): p. 3243-3262.
4. Yoshio, M., R.J. Brodd, and A. Kozawa, *Lithium-ion batteries*. Vol. 1. 2009: Springer.
5. Yoshino, A., *The birth of the lithium‐ion battery.* Angewandte Chemie International Edition, 2012. **51**(24): p. 5798-5800.
6. Bernardes, A., D.C.R. Espinosa, and J.S. Tenório, *Recycling of batteries: a review of current processes and technologies.* Journal of Power Sources, 2004. **130**(1-2): p. 291-298.
7. Ritchie, A. and W. Howard, *Recent developments and likely advances in lithium-ion batteries.* Journal of Power Sources, 2006. **162**(2): p. 809-812.
8. Goodenough, J.B., *Electrochemical energy storage in a sustainable modern society.* Energy & Environmental Science, 2014. **7**(1): p. 14-18.
9. Lu, L., et al., *A review on the key issues for lithium-ion battery management in electric vehicles.* Journal of power sources, 2013. **226**: p. 272-288.
10. Jaguemont, J., L. Boulon, and Y. Dubé, *A comprehensive review of lithium-ion batteries used in hybrid and electric vehicles at cold temperatures.* Applied Energy, 2016. **164**: p. 99-114.
11. Li, Y., J. Song, and J. Yang, *A review on structure model and energy system design of lithium-ion battery in renewable energy vehicle.* Renewable and Sustainable Energy Reviews, 2014. **37**: p. 627-633.
12. Lee, S.S., et al. *Joining technologies for automotive lithium-ion battery manufacturing: a review*. in *ASME 2010 international manufacturing science and engineering conference*. 2011. American Society of Mechanical Engineers Digital Collection.
13. Hannan, M.A., et al., *A review of lithium-ion battery state of charge estimation and management system in electric vehicle applications: Challenges and recommendations.* Renewable and Sustainable Energy Reviews, 2017. **78**: p. 834-854.
14. Nykvist, B. and M. Nilsson, *Rapidly falling costs of battery packs for electric vehicles.* Nature climate change, 2015. **5**(4): p. 329.
15. Yang, H., et al., *A review of Li-ion cell chemistries and their potential use in hybrid electric vehicles.* Journal of industrial and engineering chemistry, 2006. **12**(1): p. 12-38.
16. Waag, W., C. Fleischer, and D.U. Sauer, *Critical review of the methods for monitoring of lithium-ion batteries in electric and hybrid vehicles.* Journal of Power Sources, 2014. **258**: p. 321-339.
17. Zhang, S.S., *A review on the separators of liquid electrolyte Li-ion batteries.* Journal of power sources, 2007. **164**(1): p. 351-364.
18. Yuan, X., H. Liu, and J. Zhang, *Lithium-ion batteries: advanced materials and technologies*. 2011: CRC press.

19. Weber, C.J., et al. *Material review of Li ion battery separators*. in *AIP Conference Proceedings*. 2014. AIP.
20. Xiang, Y., et al., *Advanced separators for lithium‐ion and lithium–sulfur batteries: a review of recent progress.* ChemSusChem, 2016. **9**(21): p. 3023-3039.
21. Aifantis, K.E., S.A. Hackney, and R.V. Kumar, *High energy density lithium batteries*. 2010: Wiley Online Library.
22. Nazri, G.-A. and G. Pistoia, *Lithium batteries: science and technology*. 2008: Springer Science & Business Media.
23. Yang, Y., et al., *Transparent lithium-ion batteries.* Proceedings of the National Academy of Sciences, 2011. **108**(32): p. 13013-13018.
24. Tarascon, J.-M., et al., *Performance of Bellcore's plastic rechargeable Li-ion batteries.* Solid State Ionics, 1996. **86**: p. 49-54.
25. Daniel, C., *Materials and processing for lithium-ion batteries.* Jom, 2008. **60**(9): p. 43-48.
26. Cho, S.J., et al., *Hetero‐nanonet rechargeable paper batteries: toward ultrahigh energy density and origami foldability.* Advanced Functional Materials, 2015. **25**(38): p. 6029-6040.
27. Liu, W., et al., *Stretchable Lithium‐Ion Batteries Enabled by Device‐Scaled Wavy Structure and Elastic‐Sticky Separator.* Advanced Energy Materials, 2017. **7**(21): p. 1701076.
28. Prosini, P.P., P. Villano, and M. Carewska, *A novel intrinsically porous separator for self-standing lithium-ion batteries.* Electrochimica acta, 2002. **48**(3): p. 227-233.
29. Eroglu, D., K.R. Zavadil, and K.G. Gallagher, *Critical link between materials chemistry and cell-level design for high energy density and low cost lithium-sulfur transportation battery.* Journal of The Electrochemical Society, 2015. **162**(6): p. A982-A990.
30. Berecibar, M., et al., *Critical review of state of health estimation methods of Li-ion batteries for real applications.* Renewable and Sustainable Energy Reviews, 2016. **56**: p. 572-587.
31. Abada, S., et al., *Safety focused modeling of lithium-ion batteries: A review.* Journal of Power Sources, 2016. **306**: p. 178-192.
32. An, Z., et al., *A review on lithium-ion power battery thermal management technologies and thermal safety.* Journal of Thermal Science, 2017. **26**(5): p. 391-412.
33. Feng, X., et al., *Thermal runaway mechanism of lithium ion battery for electric vehicles: A review.* Energy Storage Materials, 2018. **10**: p. 246-267.
34. Rezvanizaniani, S.M., et al., *Review and recent advances in battery health monitoring and prognostics technologies for electric vehicle (EV) safety and mobility.* Journal of Power Sources, 2014. **256**: p. 110-124.
35. Moshtev, R. and B. Johnson, *State of the art of commercial Li ion batteries.* Journal of power sources, 2000. **91**(2): p. 86-91.
36. Van Schalkwijk, W. and B. Scrosati, *Advances in lithium ion batteries introduction*, in *Advances in Lithium-Ion Batteries*. 2002, Springer. p. 1-5.
37. Malini, R., et al., *Conversion reactions: a new pathway to realise energy in lithium-ion battery.* Ionics, 2009. **15**(3): p. 301-307.
38. Aurbach, D., et al., *Review on electrode–electrolyte solution interactions, related to cathode materials for Li-ion batteries.* Journal of Power Sources, 2007. **165**(2): p. 491-499.
39. Harks, P., F. Mulder, and P. Notten, *In situ methods for Li-ion battery research: A review of recent developments.* Journal of power sources, 2015. **288**: p. 92-105.

40. Jabbour, L., et al., *Cellulose-based Li-ion batteries: a review.* Cellulose, 2013. **20**(4): p. 1523-1545.
41. Martha, S., et al., *A short review on surface chemical aspects of Li batteries: A key for a good performance.* Journal of Power Sources, 2009. **189**(1): p. 288-296.
42. Sun, K., et al., *3D printing of interdigitated Li‐Ion microbattery architectures.* Advanced materials, 2013. **25**(33): p. 4539-4543.
43. Stephan, A.M., *Review on gel polymer electrolytes for lithium batteries.* European polymer journal, 2006. **42**(1): p. 21-42.
44. Marom, R., et al., *A review of advanced and practical lithium battery materials.* Journal of Materials Chemistry, 2011. **21**(27): p. 9938-9954.
45. Wang, C.-Y., et al., *Lithium-ion battery structure that self-heats at low temperatures.* Nature, 2016. **529**(7587): p. 515.
46. Goriparti, S., et al., *Review on recent progress of nanostructured anode materials for Li-ion batteries.* Journal of power sources, 2014. **257**: p. 421-443.
47. Ma, D., Z. Cao, and A. Hu, *Si-based anode materials for Li-ion batteries: a mini review.* Nano-Micro Letters, 2014. **6**(4): p. 347-358.
48. De las Casas, C. and W. Li, *A review of application of carbon nanotubes for lithium ion battery anode material.* Journal of Power Sources, 2012. **208**: p. 74-85.
49. Liu, N., et al., *A yolk-shell design for stabilized and scalable Li-ion battery alloy anodes.* Nano letters, 2012. **12**(6): p. 3315-3321.
50. Zhao, Y., et al., *Significant impact of 2D graphene nanosheets on large volume change tin-based anodes in lithium-ion batteries: a review.* Journal of Power Sources, 2015. **274**: p. 869-884.
51. Thackeray, M., et al., *Spinel electrodes for lithium batteries—a review.* Journal of power sources, 1987. **21**(1): p. 1-8.
52. Lin, D., Y. Liu, and Y. Cui, *Reviving the lithium metal anode for high-energy batteries.* Nature nanotechnology, 2017. **12**(3): p. 194.
53. Zhang, K., et al., *Recent developments of the lithium metal anode for rechargeable non‐aqueous batteries.* Advanced Energy Materials, 2016. **6**(20): p. 1600811.
54. Cheng, X.-B., et al., *Toward safe lithium metal anode in rechargeable batteries: a review.* Chemical reviews, 2017. **117**(15): p. 10403-10473.
55. Zhang, J.-G., W. Xu, and W.A. Henderson, *Lithium metal anodes and rechargeable lithium metal batteries.* 2017.
56. Waldmann, T., B.-I. Hogg, and M. Wohlfahrt-Mehrens, *Li plating as unwanted side reaction in commercial Li-ion cells–A review.* Journal of Power Sources, 2018. **384**: p. 107-124.
57. Cheng, X.B., et al., *A review of solid electrolyte interphases on lithium metal anode.* Advanced Science, 2016. **3**(3).
58. Aurbach, D., et al., *A short review of failure mechanisms of lithium metal and lithiated graphite anodes in liquid electrolyte solutions.* Solid state ionics, 2002. **148**(3-4): p. 405-416.
59. Lu, D., et al., *Failure mechanism for fast‐charged lithium metal batteries with liquid electrolytes.* Advanced Energy Materials, 2015. **5**(3): p. 1400993.
60. Nishikawa, K., et al., *In situ observation of dendrite growth of electrodeposited Li metal.* Journal of The Electrochemical Society, 2010. **157**(11): p. A1212-A1217.
61. Ren, Y., et al., *Direct observation of lithium dendrites inside garnet-type lithium-ion solid electrolyte.* Electrochemistry Communications, 2015. **57**: p. 27-30.

62. Cheng, E.J., A. Sharafi, and J. Sakamoto, *Intergranular Li metal propagation through polycrystalline Li6. 25Al0. 25La3Zr2O12 ceramic electrolyte.* Electrochimica Acta, 2017. **223**: p. 85-91.
63. Peled, E., *The electrochemical behavior of alkali and alkaline earth metals in nonaqueous battery systems—the solid electrolyte interphase model.* Journal of The Electrochemical Society, 1979. **126**(12): p. 2047-2051.
64. Pinson, M.B. and M.Z. Bazant, *Theory of SEI formation in rechargeable batteries: capacity fade, accelerated aging and lifetime prediction.* Journal of the Electrochemical Society, 2013. **160**(2): p. A243-A250.
65. Agubra, V. and J. Fergus, *Lithium ion battery anode aging mechanisms.* Materials, 2013. **6**(4): p. 1310-1325.
66. Dubarry, M., et al., *Identifying battery aging mechanisms in large format Li ion cells.* Journal of Power Sources, 2011. **196**(7): p. 3420-3425.
67. Su, X., et al., *Silicon‐based nanomaterials for lithium‐ion batteries: a review.* Advanced Energy Materials, 2014. **4**(1): p. 1300882.
68. Ge, M., et al., *Review of porous silicon preparation and its application for lithium-ion battery anodes.* Nanotechnology, 2013. **24**(42): p. 422001.
69. Wu, Y.-P., E. Rahm, and R. Holze, *Carbon anode materials for lithium ion batteries.* Journal of Power Sources, 2003. **114**(2): p. 228-236.
70. Leenheer, A.J., et al., *Lithium electrodeposition dynamics in aprotic electrolyte observed in situ via transmission electron microscopy.* ACS nano, 2015. **9**(4): p. 4379-4389.
71. Wen, J., Y. Yu, and C. Chen, *A review on lithium-ion batteries safety issues: existing problems and possible solutions.* Materials express, 2012. **2**(3): p. 197-212.
72. Xu, X., et al., *Recent progresses in the suppression method based on the growth mechanism of lithium dendrite.* Journal of energy chemistry, 2018. **27**(2): p. 513-527.
73. Kushima, A., et al., *Liquid cell transmission electron microscopy observation of lithium metal growth and dissolution: Root growth, dead lithium and lithium flotsams.* Nano Energy, 2017. **32**: p. 271-279.
74. Bhattacharyya, R., et al., *In situ NMR observation of the formation of metallic lithium microstructures in lithium batteries.* Nature materials, 2010. **9**(6): p. 504.
75. Chen, K.-H., et al., *Dead lithium: mass transport effects on voltage, capacity, and failure of lithium metal anodes.* Journal of Materials Chemistry A, 2017. **5**(23): p. 11671-11681.
76. Doughty, D.H. and E.P. Roth, *A general discussion of Li ion battery safety.* The Electrochemical Society Interface, 2012. **21**(2): p. 37-44.
77. Wang, Q., et al., *Thermal runaway caused fire and explosion of lithium ion battery.* Journal of power sources, 2012. **208**: p. 210-224.
78. Hao, F., A. Verma, and P.P. Mukherjee, *Mechanistic insight into dendrite–SEI interactions for lithium metal electrodes.* Journal of Materials Chemistry A, 2018. **6**(40): p. 19664-19671.
79. Steiger, J., D. Kramer, and R. Mönig, *Mechanisms of dendritic growth investigated by in situ light microscopy during electrodeposition and dissolution of lithium.* Journal of Power Sources, 2014. **261**: p. 112-119.
80. Leung, K., *Two-electron reduction of ethylene carbonate: A quantum chemistry re-examination of mechanisms.* Chemical Physics Letters, 2013. **568**: p. 1-8.
81. Aryanfar, A., et al., *Dynamics of lithium dendrite growth and inhibition: Pulse charging experiments and Monte Carlo calculations.* The journal of physical chemistry letters, 2014. **5**(10): p. 1721-1726.

82. Liu, Z., et al., *Interfacial study on solid electrolyte interphase at Li metal anode: implication for Li dendrite growth.* Journal of The Electrochemical Society, 2016. **163**(3): p. A592-A598.
83. Li, W., et al., *The synergetic effect of lithium polysulfide and lithium nitrate to prevent lithium dendrite growth.* Nature communications, 2015. **6**: p. 7436.
84. Kim, J.-S., et al., *Controlled lithium dendrite growth by a synergistic effect of multilayered graphene coating and an electrolyte additive.* Chemistry of Materials, 2015. **27**(8): p. 2780-2787.
85. Schweikert, N., et al., *Suppressed lithium dendrite growth in lithium batteries using ionic liquid electrolytes: Investigation by electrochemical impedance spectroscopy, scanning electron microscopy, and in situ7Li nuclear magnetic resonance spectroscopy.* Journal of Power Sources, 2013. **228**: p. 237-243.
86. Banik, S.J. and R. Akolkar, *Suppressing dendrite growth during zinc electrodeposition by PEG-200 additive.* Journal of The Electrochemical Society, 2013. **160**(11): p. D519-D523.
87. Qian, J., et al., *Dendrite-free Li deposition using trace-amounts of water as an electrolyte additive.* Nano Energy, 2015. **15**: p. 135-144.
88. Zheng, J., et al., *Electrolyte additive enabled fast charging and stable cycling lithium metal batteries.* Nature Energy, 2017. **2**(3): p. 17012.
89. Li, N.W., et al., *An artificial solid electrolyte interphase layer for stable lithium metal anodes.* Advanced materials, 2016. **28**(9): p. 1853-1858.
90. Luo, J., C.C. Fang, and N.L. Wu, *High Polarity Poly (vinylidene difluoride) Thin Coating for Dendrite‐Free and High‐Performance Lithium Metal Anodes.* Advanced Energy Materials, 2018. **8**(2): p. 1701482.
91. Liu, Y., et al., *An artificial solid electrolyte interphase with high Li‐ion conductivity, mechanical strength, and flexibility for stable lithium metal anodes.* Advanced Materials, 2017. **29**(10): p. 1605531.
92. Fan, L., et al., *Regulating Li deposition at artificial solid electrolyte interphases.* Journal of Materials Chemistry A, 2017. **5**(7): p. 3483-3492.
93. Li, G., et al., *Electrokinetic Phenomena Enhanced Lithium‐Ion Transport in Leaky Film for Stable Lithium Metal Anodes.* Advanced Energy Materials, 2019. **9**(22): p. 1900704.
94. Li, G., et al., *Stable metal battery anodes enabled by polyethylenimine sponge hosts by way of electrokinetic effects.* Nature Energy, 2018. **3**(12): p. 1076.
95. Zheng, G., et al., *Interconnected hollow carbon nanospheres for stable lithium metal anodes.* Nature nanotechnology, 2014. **9**(8): p. 618.
96. Liang, Z., et al., *Polymer nanofiber-guided uniform lithium deposition for battery electrodes.* Nano letters, 2015. **15**(5): p. 2910-2916.
97. Yun, Q., et al., *Chemical dealloying derived 3D porous current collector for Li metal anodes.* Advanced Materials, 2016. **28**(32): p. 6932-6939.
98. Zhang, R., et al., *Conductive nanostructured scaffolds render low local current density to inhibit lithium dendrite growth.* Advanced Materials, 2016. **28**(11): p. 2155-2162.
99. Wang, C., et al., *Suppression of lithium dendrite formation by using LAGP-PEO (LiTFSI) composite solid electrolyte and lithium metal anode modified by PEO (LiTFSI) in all-solid-state lithium batteries.* ACS applied materials & interfaces, 2017. **9**(15): p. 13694-13702.
100. Wan, J., et al., *Ultrathin, flexible, solid polymer composite electrolyte enabled with aligned nanoporous host for lithium batteries.* Nature nanotechnology, 2019: p. 1.
101. Han, F., et al., *Suppressing Li dendrite formation in Li2S‐P2S5 solid electrolyte by LiI incorporation.* Advanced Energy Materials, 2018. **8**(18): p. 1703644.

102. Duan, H., et al., *Dendrite-free Li-metal battery enabled by a thin asymmetric solid electrolyte with engineered layers.* Journal of the American Chemical Society, 2017. **140**(1): p. 82-85.
103. Zhou, D., et al., *SiO2 Hollow Nanosphere - Based Composite Solid Electrolyte for Lithium Metal Batteries to Suppress Lithium Dendrite Growth and Enhance Cycle Life.* Advanced Energy Materials, 2016. **6**(7): p. 1502214.
104. Aurbach, D., et al., *Design of electrolyte solutions for Li and Li-ion batteries: a review.* Electrochimica Acta, 2004. **50**(2-3): p. 247-254.
105. Porz, L., et al., *Mechanism of lithium metal penetration through inorganic solid electrolytes.* Advanced Energy Materials, 2017. **7**(20): p. 1701003.
106. Luntz, A.C., J. Voss, and K. Reuter, *Interfacial challenges in solid-state Li ion batteries*. 2015, ACS Publications.
107. Ding, F., et al., *Dendrite-free lithium deposition via self-healing electrostatic shield mechanism.* Journal of the American Chemical Society, 2013. **135**(11): p. 4450-4456.
108. Chen, Y., et al., *Electrical and lithium ion dynamics in three main components of solid electrolyte interphase from density functional theory study.* The Journal of Physical Chemistry C, 2011. **115**(14): p. 7044-7049.
109. Pan, J., Y.-T. Cheng, and Y. Qi, *General method to predict voltage-dependent ionic conduction in a solid electrolyte coating on electrodes.* Physical Review B, 2015. **91**(13): p. 134116.
110. Leung, K., et al., *Using atomic layer deposition to hinder solvent decomposition in lithium ion batteries: first-principles modeling and experimental studies.* Journal of the American Chemical Society, 2011. **133**(37): p. 14741-14754.
111. Jand, S.P. and P. Kaghazchi, *The role of electrostatic effects in determining the structure of LiF-graphene interfaces.* Journal of Physics: Condensed Matter, 2014. **26**(26): p. 262001.
112. Santosh, K., et al., *Electrode-Electrolyte Interface for Solid State Li-Ion Batteries: Point Defects and Mechanical Strain.* Journal of The Electrochemical Society, 2014. **161**(11): p. F3104-F3110.
113. Lepley, N., N. Holzwarth, and Y.A. Du, *Structures, Li+ mobilities, and interfacial properties of solid electrolytes Li 3 PS 4 and Li 3 PO 4 from first principles.* Physical Review B, 2013. **88**(10): p. 104103.
114. Monroe, C. and J. Newman, *Dendrite growth in lithium/polymer systems a propagation model for liquid electrolytes under galvanostatic conditions.* Journal of The Electrochemical Society, 2003. **150**(10): p. A1377-A1384.
115. Monroe, C. and J. Newman, *The effect of interfacial deformation on electrodeposition kinetics.* Journal of The Electrochemical Society, 2004. **151**(6): p. A880-A886.
116. Akolkar, R., *Modeling dendrite growth during lithium electrodeposition at sub-ambient temperature.* Journal of Power Sources, 2014. **246**: p. 84-89.
117. Akolkar, R., *Mathematical model of the dendritic growth during lithium electrodeposition.* Journal of Power Sources, 2013. **232**: p. 23-28.
118. Chen, L.-Q., *Phase-field models for microstructure evolution.* Annual review of materials research, 2002. **32**(1): p. 113-140.
119. Liang, L., et al., *Nonlinear phase-field model for electrode-electrolyte interface evolution.* Physical Review E, 2012. **86**(5): p. 051609.
120. Chen, L., et al., *Modulation of dendritic patterns during electrodeposition: A nonlinear phase-field model.* Journal of Power Sources, 2015. **300**: p. 376-385.
121. Bazant, M.Z., *Theory of chemical kinetics and charge transfer based on nonequilibrium thermodynamics.* Accounts of chemical research, 2013. **46**(5): p. 1144-1160.

122. Jana, A., D.R. Ely, and R.E. García, *Dendrite-separator interactions in lithium-based batteries.* Journal of Power Sources, 2015. **275**: p. 912-921.
123. Ely, D.R., A. Jana, and R.E. García, *Phase field kinetics of lithium electrodeposits.* Journal of Power Sources, 2014. **272**: p. 581-594.
124. Wang, K., et al., *Dendrite growth in the recharging process of zinc–air batteries.* Journal of Materials Chemistry A, 2015. **3**(45): p. 22648-22655.
125. Cogswell, D.A., *Quantitative phase-field modeling of dendritic electrodeposition.* Physical Review E, 2015. **92**(1): p. 011301.
126. Yurkiv, V., et al., *Phase-field modeling of solid electrolyte interface (SEI) influence on Li dendritic behavior.* Electrochimica Acta, 2018. **265**: p. 609-619.
127. Winter, M., *The solid electrolyte interphase–the most important and the least understood solid electrolyte in rechargeable Li batteries.* Zeitschrift für Physikalische Chemie International journal of research in physical chemistry and chemical physics, 2009. **223**(10-11): p. 1395-1406.
128. Armand, M. and J.-M. Tarascon, *Building better batteries.* nature, 2008. **451**(7179): p. 652.
129. Zhang, S.S., *A review on electrolyte additives for lithium-ion batteries.* Journal of Power Sources, 2006. **162**(2): p. 1379-1394.
130. Aurbach, D., Y. Gofer, and J. Langzam, *The correlation between surface chemistry, surface morphology, and cycling efficiency of lithium electrodes in a few polar aprotic systems.* Journal of the Electrochemical Society, 1989. **136**(11): p. 3198-3205.
131. Lu, Y., Z. Tu, and L.A. Archer, *Stable lithium electrodeposition in liquid and nanoporous solid electrolytes.* Nature materials, 2014. **13**(10): p. 961.
132. Verma, P., P. Maire, and P. Novák, *A review of the features and analyses of the solid electrolyte interphase in Li-ion batteries.* Electrochimica Acta, 2010. **55**(22): p. 6332-6341.
133. Peled, E., *Film forming reaction at the lithium/electrolyte interface.* Journal of Power Sources, 1983. **9**(3): p. 253-266.
134. Kanamura, K., et al., *XPS analysis of lithium surfaces following immersion in various solvents containing LiBF4.* Journal of the Electrochemical Society, 1995. **142**(2): p. 340-347.
135. Peled, E., et al., *The sei model—application to lithium-polymer electrolyte batteries.* Electrochimica acta, 1995. **40**(13): p. 2197-2204.
136. Peled, E., D. Golodnitsky, and G. Ardel, *Advanced model for solid electrolyte interphase electrodes in liquid and polymer electrolytes.* Journal of the Electrochemical Society, 1997. **144**(8): p. L208-L210.
137. Aurbach, D., *Review of selected electrode–solution interactions which determine the performance of Li and Li ion batteries.* Journal of Power Sources, 2000. **89**(2): p. 206-218.
138. Lu, P., et al., *Chemistry, impedance, and morphology evolution in solid electrolyte interphase films during formation in lithium ion batteries.* The Journal of Physical Chemistry C, 2014. **118**(2): p. 896-903.
139. Lu, P. and S.J. Harris, *Lithium transport within the solid electrolyte interphase.* Electrochemistry Communications, 2011. **13**(10): p. 1035-1037.
140. Shi, S., et al., *Defect thermodynamics and diffusion mechanisms in Li2CO3 and implications for the solid electrolyte interphase in li-ion batteries.* The Journal of Physical Chemistry C, 2013. **117**(17): p. 8579-8593.

141. Idemoto, Y., et al., *Crystal structure of (Li x K 1− x) 2 CO 3 (x= 0, 0.43, 0.5, 0.62, 1) by neutron powder diffraction analysis.* Journal of Physics and Chemistry of Solids, 1998. **59**(3): p. 363-376.
142. Fiorentini, V. and M. Methfessel, *Extracting convergent surface energies from slab calculations.* Journal of Physics: Condensed Matter, 1996. **8**(36): p. 6525.
143. Wang, Y., et al., *First-principles calculations of β″-Mg 5 Si 6/α-Al interfaces.* Acta Materialia, 2007. **55**(17): p. 5934-5947.
144. Kresse, G., *Comput. Matter Sci. 6, 15 (1996);(d) Kresse, G., and Furthmuller.* Phys. Rev. B, 1996. **54**: p. 11,169.
145. Kresse, G. and J. Furthmüller, *Efficient iterative schemes for ab initio total-energy calculations using a plane-wave basis set.* Physical Review B, 1996. **54**(16): p. 11169.
146. Kresse, G. and D. Joubert, *From ultrasoft pseudopotentials to the projector augmented-wave method.* Physical Review B, 1999. **59**(3): p. 1758.
147. Perdew, J.P., K. Burke, and M. Ernzerhof, *Generalized gradient approximation made simple.* Physical review letters, 1996. **77**(18): p. 3865.
148. Perdew, J.P., et al., *Restoring the density-gradient expansion for exchange in solids and surfaces.* Physical Review Letters, 2008. **100**(13): p. 136406.
149. Recker, K., F. Wallrafen, and K. Dupre, *Directional solidification of the LiF-LiBaF 3 eutectic.* Naturwissenschaften, 1988. **75**(3): p. 156-157.
150. Anderson, M. and C. Swenson, *Experimental equations of state for cesium and lithium metals to 20 kbar and the high-pressure behavior of the alkali metals.* Physical Review B, 1985. **31**(2): p. 668.
151. Bruno, M. and M. Prencipe, *Ab initio quantum-mechanical modeling of the (001), and (110) surfaces of zabuyelite (Li 2 CO 3).* Surface science, 2007. **601**(14): p. 3012-3019.
152. Kokko, K., et al., *First-principles calculations for work function and surface energy of thin lithium films.* Surface science, 1996. **348**(1): p. 168-174.
153. Tyson, W. and W. Miller, *Surface free energies of solid metals: Estimation from liquid surface tension measurements.* Surface Science, 1977. **62**(1): p. 267-276.
154. Gilman, J.J., *Direct measurements of the surface energies of crystals.* Journal of Applied Physics, 1960. **31**(12): p. 2208-2218.
155. Lin, Y., et al., *Connecting the irreversible capacity loss in Li ion batteries with the electronic insulating properties of SEI components --- from first principle calculations.* Journal of The Electrochemical Society, 2015: p. To be submitted.
156. Zeng, Z., et al., *Visualization of electrode–electrolyte interfaces in LiPF6/EC/DEC electrolyte for lithium ion batteries via in situ TEM.* Nano letters, 2014. **14**(4): p. 1745-1750.
157. Gu, M., et al., *Demonstration of an electrochemical liquid cell for operando transmission electron microscopy observation of the lithiation/delithiation behavior of Si nanowire battery anodes.* Nano letters, 2013. **13**(12): p. 6106-6112.
158. Mehdi, B.L., et al., *In-situ electrochemical transmission electron microscopy for battery research.* Microscopy and Microanalysis, 2014. **20**(2): p. 484-492.
159. Suo, L., et al., *How Solid-Electrolyte Interphase Forms in Aqueous Electrolytes.* Journal of the American Chemical Society, 2017. **139**(51): p. 18670-18680.
160. Nandasiri, M.I., et al., *In Situ Chemical Imaging of Solid-Electrolyte Interphase Layer Evolution in Li–S Batteries.* Chemistry of Materials, 2017. **29**(11): p. 4728-4737.
161. Cheong, J.Y., et al., *Growth dynamics of solid electrolyte interphase layer on SnO2 nanotubes realized by graphene liquid cell electron microscopy.* Nano Energy, 2016. **25**: p. 154-160.

162. Shi, Y., et al., *Direct Visualization of Nucleation and Growth Processes of Solid Electrolyte Interphase Film Using in Situ Atomic Force Microscopy.* ACS applied materials & interfaces, 2017. **9**(26): p. 22063-22067.
163. Steinhauer, M., et al., *Investigation of the solid electrolyte interphase formation at graphite anodes in lithium-ion batteries with electrochemical impedance spectroscopy.* Electrochimica Acta, 2017. **228**: p. 652-658.
164. Lin, Y.-X., et al., *Connecting the irreversible capacity loss in Li-ion batteries with the electronic insulating properties of solid electrolyte interphase (SEI) components.* Journal of Power Sources, 2016. **309**: p. 221-230.
165. Li, Y., K. Leung, and Y. Qi, *Computational Exploration of the Li-Electrode| Electrolyte Interface in the Presence of a Nanometer Thick Solid-Electrolyte Interphase Layer.* Accounts of chemical research, 2016. **49**(10): p. 2363-2370.
166. LePage, W.S., et al., *Lithium Mechanics: Roles of Strain Rate and Temperature and Implications for Lithium Metal Batteries.* Journal of The Electrochemical Society, 2019. **166**(2): p. A89-A97.
167. Kim, S.-P., A.C. Van Duin, and V.B. Shenoy, *Effect of electrolytes on the structure and evolution of the solid electrolyte interphase (SEI) in Li-ion batteries: A molecular dynamics study.* Journal of Power Sources, 2011. **196**(20): p. 8590-8597.
168. Shkrob, I.A., et al., *Reduction of carbonate electrolytes and the formation of solid-electrolyte interface (SEI) in Lithium-ion batteries. 1. spectroscopic observations of radical intermediates generated in one-electron reduction of carbonates.* The Journal of Physical Chemistry C, 2013. **117**(38): p. 19255-19269.
169. Hao, F., et al., *Mesoscale Elucidation of Solid Electrolyte Interphase Layer Formation in Li-Ion Battery Anode.* The Journal of Physical Chemistry C, 2017. **121**(47): p. 26233-26240.
170. Ushirogata, K., et al., *Near-shore aggregation mechanism of electrolyte decomposition products to explain solid electrolyte interphase formation.* Journal of The Electrochemical Society, 2015. **162**(14): p. A2670-A2678.
171. Takenaka, N., et al., *On electrolyte-dependent formation of solid electrolyte interphase film in lithium-ion batteries: strong sensitivity to small structural difference of electrolyte molecules.* The Journal of Physical Chemistry C, 2014. **118**(20): p. 10874-10882.
172. Yang, C., Y. Wang, and C. Wan, *Composition analysis of the passive film on the carbon electrode of a lithium-ion battery with an EC-based electrolyte.* Journal of power sources, 1998. **72**(1): p. 66-70.
173. Shi, S., et al., *Direct calculation of Li-ion transport in the solid electrolyte interphase.* Journal of the American Chemical Society, 2012. **134**(37): p. 15476-15487.
174. Wang, A., et al., *Review on modeling of the anode solid electrolyte interphase (SEI) for lithium-ion batteries.* npj Computational Materials, 2018. **4**(1): p. 15.
175. Yoo, H.D., et al., *Mg rechargeable batteries: an on-going challenge.* Energy & Environmental Science, 2013. **6**(8): p. 2265-2279.
176. Cheng, Y., et al., *Rechargeable Mg–Li hybrid batteries: status and challenges.* Journal of Materials Research, 2016. **31**(20): p. 3125-3141.
177. Song, J., et al., *Mapping the challenges of magnesium battery.* The journal of physical chemistry letters, 2016. **7**(9): p. 1736-1749.
178. Muldoon, J., et al., *Electrolyte roadblocks to a magnesium rechargeable battery.* Energy & Environmental Science, 2012. **5**(3): p. 5941-5950.
179. Tutusaus, O. and R. Mohtadi, *Paving the way towards highly stable and practical electrolytes for rechargeable magnesium batteries.* ChemElectroChem, 2015. **2**(1): p. 51-57.

180. Levi, E., Y. Gofer, and D. Aurbach, *On the way to rechargeable Mg batteries: the challenge of new cathode materials.* Chemistry of Materials, 2009. **22**(3): p. 860-868.
181. Ling, C., D. Banerjee, and M. Matsui, *Study of the electrochemical deposition of Mg in the atomic level: Why it prefers the non-dendritic morphology.* Electrochimica Acta, 2012. **76**: p. 270-274.
182. Jäckle, M. and A. Groß, *Microscopic properties of lithium, sodium, and magnesium battery anode materials related to possible dendrite growth.* The Journal of Chemical Physics, 2014. **141**(17): p. 174710.
183. Jäckle, M., et al., *Self-diffusion barriers: possible descriptors for dendrite growth in batteries?* Energy & Environmental Science, 2018.
184. Yoo, H.D., et al., *High areal capacity hybrid magnesium–lithium-ion battery with 99.9% coulombic efficiency for large-scale energy storage.* ACS applied materials & interfaces, 2015. **7**(12): p. 7001-7007.
185. Asadi, E. and M.A. Zaeem, *The anisotropy of hexagonal close-packed and liquid interface free energy using molecular dynamics simulations based on modified embedded-atom method.* Acta Materialia, 2016. **107**: p. 337-344.
186. Cheng, Q., et al., *Operando and three-dimensional visualization of anion depletion and lithium growth by stimulated Raman scattering microscopy.* Nature communications, 2018. **9**(1): p. 2942.
187. Brissot, C., et al., *In situ study of dendritic growth inlithium/PEO-salt/lithium cells.* Electrochimica acta, 1998. **43**(10-11): p. 1569-1574.
188. Brissot, C., et al., *In Situ Concentration Cartography in the Neighborhood of Dendrites Growing in Lithium/Polymer‐Electrolyte/Lithium Cells.* Journal of the Electrochemical Society, 1999. **146**(12): p. 4393-4400.
189. Jäckle, M., et al., *Self-diffusion barriers: possible descriptors for dendrite growth in batteries?* Energy & Environmental Science, 2018. **11**(12): p. 3400-3407.
190. Tran, R., et al., *Surface energies of elemental crystals.* Scientific data, 2016. **3**: p. 160080.
191. Gamburg, Y.D. and G. Zangari, *Theory and practice of metal electrodeposition*. 2011: Springer Science & Business Media.
192. Ding, M.S., et al., *Dendrite growth in Mg metal cells containing Mg (TFSI) 2/glyme electrolytes.* Journal of The Electrochemical Society, 2018. **165**(10): p. A1983-A1990.
193. Monroe, C. and J. Newman, *The impact of elastic deformation on deposition kinetics at lithium/polymer interfaces.* Journal of the Electrochemical Society, 2005. **152**(2): p. A396-A404.
194. Suzuki, Y., et al., *Transparent cubic garnet-type solid electrolyte of Al 2 O 3-doped Li 7 La 3 Zr 2 O 12.* Solid State Ionics, 2015. **278**: p. 172-176.
195. Basappa, R.H., et al., *Grain boundary modification to suppress lithium penetration through garnet-type solid electrolyte.* Journal of Power Sources, 2017. **363**: p. 145-152.
196. Cheng, L., et al., *Effect of surface microstructure on electrochemical performance of garnet solid electrolytes.* ACS applied materials & interfaces, 2015. **7**(3): p. 2073-2081.
197. Taylor, N.J., et al., *Demonstration of high current densities and extended cycling in the garnet Li 7 La 3 Zr 2 O 12 solid electrolyte.* Journal of Power Sources, 2018. **396**: p. 314-318.
198. Xu, B.Y., et al., *Li3PO4-added garnet-type Li6.5La3Zr1.5Ta0.5O12 for Li-dendrite suppression.* Journal of Power Sources, 2017. **354**: p. 68-73.
199. Tsai, C.L., et al., *Li7La3Zr2O12 Interface Modification for Li Dendrite Prevention.* Acs Applied Materials & Interfaces, 2016. **8**(16): p. 10617-10626.

200. Ferrese, A. and J. Newman, *Mechanical deformation of a lithium-metal anode due to a very stiff separator.* Journal of The Electrochemical Society, 2014. **161**(9): p. A1350-A1359.
201. Harry, K.J., et al., *Electrochemical deposition and stripping behavior of lithium metal across a rigid block copolymer electrolyte membrane.* Journal of The Electrochemical Society, 2015. **162**(14): p. A2699-A2706.
202. Schauser, N.S., et al., *Lithium dendrite growth in glassy and rubbery nanostructured block copolymer electrolytes.* Journal of The Electrochemical Society, 2015. **162**(3): p. A398-A405.
203. Hallinan, D.T., et al., *Lithium metal stability in batteries with block copolymer electrolytes.* Journal of The Electrochemical Society, 2013. **160**(3): p. A464-A470.
204. Stone, G., et al., *Resolution of the modulus versus adhesion dilemma in solid polymer electrolytes for rechargeable lithium metal batteries.* Journal of The Electrochemical Society, 2012. **159**(3): p. A222-A227.
205. Nagao, M., et al., *In situ SEM study of a lithium deposition and dissolution mechanism in a bulk-type solid-state cell with a Li 2 S–P 2 S 5 solid electrolyte.* Physical Chemistry Chemical Physics, 2013. **15**(42): p. 18600-18606.
206. Sharafi, A., et al., *Characterizing the Li–Li7La3Zr2O12 interface stability and kinetics as a function of temperature and current density.* Journal of Power Sources, 2016. **302**: p. 135-139.
207. Yu, S., et al., *Elastic properties of the solid electrolyte Li7La3Zr2O12 (LLZO).* Chemistry of Materials, 2015. **28**(1): p. 197-206.
208. Simmons, J., et al., *Microstructural development involving nucleation and growth phenomena simulated with the phase field method.* Materials Science and Engineering: A, 2004. **365**(1-2): p. 136-143.
209. Chen, L.-Q. and W. Yang, *Computer simulation of the domain dynamics of a quenched system with a large number of nonconserved order parameters: The grain-growth kinetics.* Physical Review B, 1994. **50**(21): p. 15752.
210. Fan, D. and L.-Q. Chen, *Diffusion-controlled grain growth in two-phase solids.* Acta materialia, 1997. **45**(8): p. 3297-3310.
211. Tian, H.-K., B. Xu, and Y. Qi, *Computational study of lithium nucleation tendency in Li 7 La 3 Zr 2 O 12 (LLZO) and rational design of interlayer materials to prevent lithium dendrites.* Journal of Power Sources, 2018. **392**: p. 79-86.
212. Fudong Han, A.S.W., Jie Yue, Xiulin Fan, Fei Wang, Miaofang Chi, Donovan N. Leonard, Nancy J. Dudney, Howard Wang, Chunsheng Wang *High electronic conductivity as the origin of lithium dendrite formation within solid electrolytes.* Nature energy, 2019.
213. Murugan, R., V. Thangadurai, and W. Weppner, *Fast lithium ion conduction in garnet-type Li7La3Zr2O12.* Angewandte Chemie-International Edition, 2007. **46**(41): p. 7778-7781.
214. Tian, H.-K., et al., *Interfacial Electronic Properties Dictate Li Dendrite Growth in Solid Electrolytes.* Chemistry of Materials, 2019.
215. Masias, A., et al., *Elastic, plastic, and creep mechanical properties of lithium metal.* Journal of materials science, 2019. **54**(3): p. 2585-2600.
216. Wang, Y. and Y.-T. Cheng, *A nanoindentation study of the viscoplastic behavior of pure lithium.* Scripta Materialia, 2017. **130**: p. 191-195.
217. Biner, S. and S.Y. Hu, *Simulation of damage evolution in composites: A phase-field model.* Acta Materialia, 2009. **57**(7): p. 2088-2097.

VITA

Zhe Liu

Zhe Liu was born in Jinan, Shandong Province, China on March 19, 1989. He got his B.E. in Materials Science and Engineering at Huazhong University of Science and Technology, China, in 2011, and M.S. in Materials Science and Engineering at University of Pennsylvania in 2013. He was enrolled in the Ph.D. program in the Department of Materials Science and Engineering at Penn State in 2013. He is the winner of the 7th and 9th Materials Visualization Competition (MVC7 and MVC9), and received the Jean Shollenberger Beaver Award from Materials Science and Engineering department at Penn State University in 2019. He authored and co-authored 10 papers at Penn State. Following is a selected publication list.

1. H-K. Tian*, **Z. Liu***, Y. Ji, L-Q. Chen, Y. Qi, "Interfacial Electronic Properties Dictate Li Dendrite Growth in Solid Electrolytes", *Chem. Mater*., doi.org/10.1021/acs.chemmater.9b01967, (2019).
2. J. Wan, J. Xie, X. Kong, **Z. Liu**, K. Liu, F. Shi, A. Pei, H. Chen, W. Chen, J. Chen, X. Zhang, L. Zong, J. Wang, L-Q. Chen, J. Qin, Y. Cui, "Ultrathin, flexible, solid polymer composite electrolyte enabled with aligned nanoporous host for lithium batteries", *Nature Nanotechnol.*, **14** 705–711 (2019).
3. G. Li*, **Z. Liu***, D. Wang, X. He, S. Liu, Y. Gao, A. AlZahrani, S. H. Kim, L-Q. Chen, D. Wang, "Electrokinetic Phenomena Enhanced Lithium-Ion Transport in Leaky Film for Stable Lithium Metal Anodes", *Adv. Energy. Mater*., 1900704 (2019).
4. G. Li, **Z. Liu**, Q. Huang, Y. Gao, M. Regula, D. Wang, L-Q Chen, D. Wang, "Stable metal anodes enabled by electrokinetic effects in high-zeta-potential porous structures", *Nature Energy*, **3** 1076 (2018).
5. **Z. Liu**, P. Lu, Q. Zhang, X. Xiao, Y. Qi, L-Q. Chen, "A Bottom-up Formation Mechanism of Solid Electrolyte Interphase Revealed by Isotope-Assisted Time-of-Flight Secondary Ion Mass Spectrometry", *J. Phys. Chem. Lett.*, **9** 5508-5514 (2018).
6. Q. Cheng, L. Wei, **Z. Liu**, N. Ni, Z. Sang, B. Zhu, W. Xu, M. Chen, Y. Miao, L-Q. Chen, W. Min, Y. Yang, "Operando and three-dimensional visualization of anion depletion and lithium growth by stimulated Raman scattering microscopy", *Nature Commun*. **9** 2942 (2018).
7. **Z. Liu**, Y. Qi, Y. Lin, L. Chen, P. Lu, L-Q. Chen, "An Interfacial Study of Solid Electrolyte Interphase at Li metal Anode from Density Functional Theory and its Implication for Li Dendrite Growth", *J. Electrochem. Soc.*, **163** (3) A592-A598 (2016).